CHARACTERIZATION OF THE BEAM DYNAMICS IN THE CORNELL ENERGY RECOVERY LINAC INJECTOR PROTOTYPE

A Dissertation

Presented to the Faculty of the Graduate School

of Cornell University

in Partial Fulfillment of the Requirements for the Degree of

Doctor of Philosophy

by

Colwyn Gulliford

August 2013

CHARACTERIZATION OF THE BEAM DYNAMICS IN THE CORNELL ENERGY RECOVERY LINAC INJECTOR PROTOTYPE

Colwyn Gulliford, Ph.D.

Cornell University 2013

Synchrotron radiation, the radiation emitted from charge particles as their trajectory bends in the presence of magnetic fields, provides one of the main driving forces behind the development and construction of particle accelerators today. As the electron sources in these accelerators are pushed to deliver increasingly brighter beams, significant physics and technological challenges must be overcome. To do so requires both a theoretical and computational understanding of the physics governing the dynamics in these sources, and experimental demonstration of the feasibility of the conclusions drawn from this understanding. To this end, we present a theoretical treatment of the linear dynamics in the combined RF and solenoid fields used in the generation of electron bunches at their source. Additionally, a method for computing and characterizing the asymmetric beam focusing caused by the input power couplers of RF cavities is given. Incorporating these methods, we present the results of a detailed study of the six dimensional phase space of the electron beam in the Cornell ERL injector prototype, a high-brightness, high repetition rate DC gun based photoinjector. The emittance results obtained in this work set a new record low for DC based photoinjectors producing comparable bunch charges, and demonstrate that DC gun based photoinjectors are capable of producing high-brightness beams which surpass the beam quality found in storage rings by a factor 20 when the energy spread in each type of machine is considered.

Biographical Sketch

I was born near Houston, Texas on January 6th, 1985. After living in Texas and upstate New York (where my younger sister was born), my family moved to Lynchburg, Virginia where the first half of my elementary education took place. Living in the woods near Thomas Jefferson's property, not far from the beautiful Blue Ridge mountains, I spent a large amount of my time walking through creeks and gaining a child's appreciation of nature. The rest of my education was completed in central Florida. After completing High School, I moved to Sarasota to attend New College of Florida, on the west coast of the state. My time at New College was in many ways idyllic, attending classes with no grades, just a stone's throw away from the Gulf of Mexico, surrounded by an enthusiastic student body, and living communally with friends. At the time, my acquaintances ranged from (often self-proclaimed) anarchists, freegans, trustafarians, hippies, hipsters, feminists, radical feminists, philosophy majors, sociologists, and the occasional space cadet, the majority of which were very passionate and hard working students. Somewhere in this mix, I decided on pursuing physics, and at the end of my third year in college managed to be accepted for a REU, a summer research program run by the NSF, at Cornell University, working for Ivan Bazarov. This eventually opened up the door to pursuing physics in graduate school, where I quickly joined the same research group I had worked for during my REU, and began my graduate research on the dynamics in the Cornell ERL injector with Ivan. During my time at Cornell, I fell in love with the Ithaca area; enjoying the beautiful natural areas, the cycling scene, the seasons, and the lovely community of refreshingly different people.

To my grandparents: Marge and David Ferm, and Esme and Michael Gulliford.

Acknowledgments

First, I would like to deeply thank my research advisor Prof. Ivan Bazarov, for his guidance and support in my research at Cornell. I am also thankful to the rest of my senior colleagues who made this research possible: John Dobbins, Bruce Dunham, Georg Hoffstaetter, Yulin Li, Xianghong Liu, Karl Smolenski, Tobbey, and Zhi Zhao, to name a few.

I also am very thankful to my fellow graduate students, in particular Joe "Calvatross" Calvey, Yanjiun "Fly-J" Chen, Walter "I'm so high" Hopkins, "Crazy" James (and Elizabeth) Inman, Siddharth "Rock-steady" Karkare, Hyeri "Damn Dude!" Lee, Jared "Max-voltage" Maxson, Stephen "Mr. Tea" Poprocki, Turan "Bustacap" Birol, Ravi-"Vampire Rider"-shankar, Heng "Many Things" Li, Michael "Just Once" Ehrlichman, and Jim "Malarky" Shanks for their friendship and support during my time at Cornell. I am also grateful to the undergraduates who worked with me on this research: Francisco Gonzalez, Allen Kim, and Christian Nguyen, who despite my eccentricity, were able to produce useful work under my guidance. Also, these results would not have been possible without my chief partner in crime, beam operator extraordinaire Adam Bartnik, who proved that any physical system could be optimized by hand as long as the pizza arrives on time.

I also owe special thanks to all those outside of Cornell who made this work possible. Here I would first like to thank my parents and my sister Caitlin, my Aunt Theresa, as well as my partner Carly Summers, for their love and support. In addition, I thank my wonderful college friends Raul Briceno, Jax Lysinger, and Tim and Michelle Sanchez, as well as my die hard high school friends Travis Briggs, Shayna Grajo, Michael Kane, and Juventino Leos. Also, I would like to thank my teacher, David Radin, and the meditation group at the Ithaca Zen Center. Special thanks to my high school teachers: Mrs. Miller,

Mrs. Goldiez, Rita Jackson, and Mr. Desanto, as well as my college professors: Don Colladay, Mariana Sendova, and David Mullins.

Finally, general thanks go out to James Brown, Toots and the Maytals, Medeski Martin and Wood, Nirvana, Jimi Hendrix, Herbie Hancock, Muddy Waters, Howlin' Wolf, Leadbelly, Dr. Funkenstein's Supergroovalistic-Prosifunkstication (a.k.a. Parliament Funkadelic), guitars, drums, The Beatles, Pato Banton, Galactic, Alan Watts, Papa Johns (Adam's fuel), Tim and Sean Rooney (and company), Thich Nhat Hanh, Priscilla and Louis at the Friday Night Macrodinner, Richard Freeman, yoga, Masanobu Fukuoka, Hank Hill, Homer Simpson, Raul Duke, Dr. Gonzo, The Muppets, Larry David, Ito Colon, the Juggernaut, Star Wars, Ghostbusters, and The Big Lebowski.

Research in this thesis was supported by the National Science Foundation (NSF) award No. DMR-0807731.

Table of Contents

List of Figures

List of Tables

CHAPTER 1

Introduction

1.1 A Brief History of Synchrotron Radiation and Accelerator Based Light Sources

In the mid to late forties, several pivotal experiments concerning the emission of radiation from electrons in circular accelerators took place at the General Electric Research Lab in Schenectady, New York. In 1944, work by Iwanenko and Pomeranchuk [1] showed that the maximum energy achievable in circular electron accelerators known as betatrons was limited by the electromagnetic power radiated away by the electrons as they are bent in a circular trajectory by applied magnetic fields. In 1945, the effect of this radiation, now known as synchrotron radiation (SR), was indirectly measured by Blewet using the General Electric 100 MeV betatron shown Fig. 1.1(a). Direct measurement of the radiation occurred later in 1947, and was carried out by Elder, Gurewitsch, Langmuir, and Pollock [2] using the General Electric 70 MeV synchrotron shown in Fig. 1.1(b), the second machine of its kind [3]. At roughly the same time, Schwinger produced a classical description of this radiation, based on previous work by Schott [4], which included predictions for the angular and frequency distribution of the emitted light. Between these initial experiments at General Electric, and later work at Cornell University using a 300 MeV synchrotron [5], the classical theory of synchrotron radiation was experimentally tested and verified.

(a) The General Electric 100 MeV betatron.

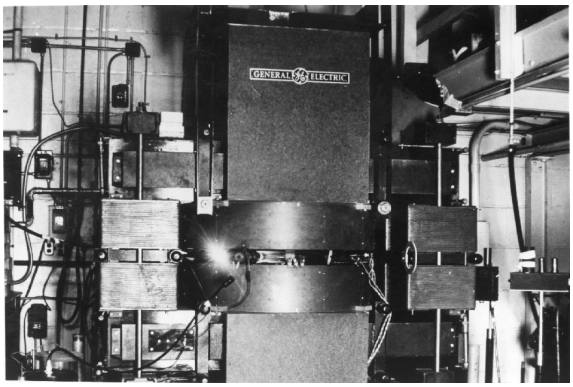

(b) The General Electric 70 MeV synchrotron.

Figure 1.1: Early synchrotron light sources: (a) the General Electric 100 MeV betatron, and (b) the General Electric 70 MeV synchrotron showing the emitted synchrotron light beam (light spot in the left corner of the machine).

Many of the extraordinary properties of SR follow largely from the concentration of the radiation into a forward cone [6, 7]. The opening angle of this cone is determined by the normalized relativistic electron energy: $\theta_{\mathrm{SR}} = 1/\gamma$ [6–9]. The total power radiated by a (classical) relativistic electron undergoing circular motion can be written approximately as [9]:

$$P_s \approx \frac{2}{3} r_e m c^3 \left(\frac{\gamma^4}{R^2} \right). \tag{1.1}$$

In this expression, R is the bending radius of the electron orbit and $r_e = e^2/4\pi\epsilon_0/mc^2$ is the classical electron radius. Another important characteristic of SR comes from the fact that the majority of the power radiated occurs up to a critical frequency, also determined by the electron orbit radius and energy [9]:

$$\omega_c = \frac{3c}{2R}\gamma^3. \tag{1.2}$$

Despite early interest in SR, the production and use of this radiation was initially limited to parasitic operation at synchrotron facilities designed for high energy physics

experiments. With the advent of the electron storage ring in the late 1960's, the stability and quality of SR increased significantly. Indeed, roughly 10^5 times more continuous radiation was provided by these first generation storage ring sources than by conventional (x-ray) light sources of the time [10]. Subsequently, interest in this high intensity, directional radiation source grew rapidly. The desire for higher SR brightness and quality lead to the construction of storage rings around the world, many of which were (are) dedicated light sources [10]. In these so-called "second generation" light sources, SR is produced primarily in the bending magnets used to keep the particles moving through the torus shaped vacuum pipe. A familiar example of combined storage ring and synchrotron facility is the Cornell Electron Storage Ring (CESR) and Cornell High Energy Sychrotron Source (CHESS), shown in Fig. 1.2(a) and 1.2(b).

(a) Overview of the CESR/CHESS facility.

(b) Inner view of the tunnel.

Figure 1.2: The Cornell Electron Storage Ring and High Energy Synchrotron Source: a roughly 5 GeV electron (positron) storage ring and x-ray source.

A significant breakthrough in SR science came with the advent of insertion devices known as undulators and wigglers [11]. These devices use alternating magnetic dipole fields perpendicular to the beam direction to periodically bend the beam trajectory in small

circular arcs. Fig. 1.3 shows the conceptual schematic of an undulator [12]. Undulators

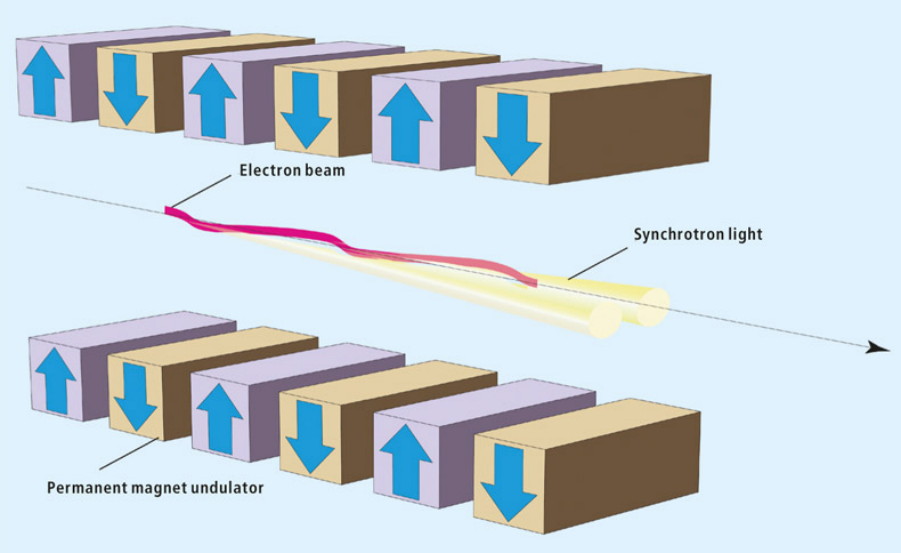

Figure 1.3: Conceptual schematic of an undulator.

typically bend the beam by an angle $\theta_{\mathrm{U}} \leq \theta_{\mathrm{SR}}$. This results in the enhancement of the SR intensity for certain wavelengths, producing a quasi-monochromatic source. Wigglers bend the beam by an angle $\theta_{\mathrm{W}} \geq \theta_{\mathrm{SR}}$, resulting in a broader frequency distribution due to the dependence on the bend radius in Eq. 1.2. In both cases, by adjusting either the magnetic field strength, dipole gap, or beam energy, undulators and wigglers offer a tunable method for producing SR. With the advent of this technology, a third generation of light sources were constructed and came online in the early 90's. A key feature of these machines was the incorporation of more straight sections for insertion devices. The use of undulators in third generation rings produced a factor of roughly 10^4 times the brightness of the SR generated from the bending magnets in earlier rings [10]. The significant gains in beam quality and brightness achieved by storage ring light sources demonstrates that this technology has substantially matured in the roughly forty years since its first implementation.

1.2 Linac Based Light Sources

A key feature of the design of third generation storage ring light sources was the emphasis placed on the SR brightness, defined as the flux per unit area of the radiation source per unit solid angle of the radiation cone per unit spectral bandwidth [13]. This quantity is integrally related to the electron beam brightness, defined roughly as

$$\mathcal{B}_{e^-} = \frac{I}{\epsilon_x \epsilon_y}. \tag{1.3}$$

In this expression I is the electron beam current, and the terms ϵ_x and ϵ_y are the horizontal and vertical *geometric emittances* of the electron beam. These quantities provide a measure of the area occupied by the electron beam in the the two dimensional phase spaces defined by the coordinates (x, θ_x) and (y, θ_y). Here θ_x and θ_y are the transverse angles made by each electron with respect to the beam line axis in the accelerator, and are approximately given by $\theta_{x,y} \simeq p_{x,y}/p_z$ in the straight sections of a machine. The resulting photon beam brightness $\mathcal{B}_\gamma$ is related to the electron beam brightness through a convolution of the photon beam emittance ϵ_γ and electron beam $\epsilon_{x,y}$ emittances. For a Gaussian mode photon beam near the diffraction limit ($\epsilon_\gamma \sim \lambda/4\pi$), this means $\mathcal{B}_\gamma \propto (\epsilon_{x,y} + \lambda/4\pi)^{-2}$, assuming cylindrically symmetric beams [9, 14]. Thus, to generate diffraction limited hard x-rays ($\lambda < 1$ Å) requires electron emittances on the order of 10 pm or less.

As it turns out, SR sets a lower limit on the electron emittance in a storage ring. In these machines, particles perform small oscillations around a closed reference orbit with design energy E_0. In the horizontal and vertical planes transverse to this orbit, these small oscillations are known as betatron motion. Similarly, particles also perform energy oscillations around the design energy known as synchrotron oscillations. To ensure particles make closed orbits around the ring, betatron oscillations are controlled with transverse

magnetic focusing fields, and synchrotron oscillations are controlled with time-dependent energy focusing in the RF fields used to maintain the beam energy.

In general, the loss of energy to SR comes at the expense of both the transverse and longitudinal momentum of the circulating particles, however, because the energy associated with the transverse motion is in typically many orders of magnitude smaller than the longitudinal energy, as well as the fact that RF fields replace energy only in the longitudinal direction, SR tends to have a dampening effect on the betatron oscillations. In addition, in light of the scaling of the emitted SR power with γ^4 in Eq. (1.1), particles with higher energy radiate more power than those with lower energy, providing a dampening mechanism to synchrotron oscillations [14].

It turns out that these dampening effects are countered by the quantum nature of the SR emission process. During the emission of a photon, an electron suddenly loses energy, which in turn excites synchrotron oscillations. The loss of energy can also lead to a different closed orbit for the electron if the photon is emitted in dispersive regions, as in the bending magnets. The combination of the quantum and damping effects of SR lead to the formation of a Gaussian equilibrium electron phase space distribution with the horizontal and vertical emittances determined by the properties of the optical elements in the accelerator. In a typical storage ring, the emittance in the horizontal plane may be 10 to 100 times larger than in the vertical plane [10, 15]. For example, emittances in PETRA III, a representative state-of-the-art third generation ring, are roughly 1 nm and 10 pm in the horizontal and vertical direction respectively [15]. Because of the increased horizontal emittance resulting from the formation of an equilibrium distribution with larger horizontal phase space area, such a machine will not be able to produce diffraction limited hard x-rays.

While there are still many ways in which storage rings can be further optimized for

x-ray production, the equilibrium process will always set a fundamental upper limit to the brightness of a given ring design. An alternative approach to the use of storage rings is provided by linear accelerators (linacs). Because beams in these devices are only accelerated and recirculated at most a relatively small number of times, the quality of the beam distribution is largely dominated by the beam quality of the initial source. In general, there are currently two light source technologies being developed which are based on linac sources.

1.2.1 The Free Electron Laser

The push for extremely high peak brightness has lead to the development of the Free Electron Laser (FEL). There are currently several x-ray FELs in operation around the world. These include, but are not limited to, the Linac Coherent Light Source at the Stanford Linear Accelerator Center (SLAC), SPring-8 Angstrom Compact Free Electron Laser (SACLA) at the RIKEN institute in Japan, the Free-electron LASer in Hamburg (FLASH), and the SwissFEL at the Paul Scherrer Institute in Switzerland [16–18]. These machines are based on the self-amplified stimulated emission (SASE) principle in which the initial electron beam is bunched longitudinally due by the undulator fields and emitted SR fields. The resulting micro-bunches are longitudinally separated by roughly the wavelength of the emitted light, yielding a coherent addition of the radiated fields. The resulting x-ray beam brightness is staggering, with a demonstrated factor of roughly 10^{10} more peak brightness compared to third-generation light sources [16]. SASE operation at LCLS has been used to generate tens of GW of tunable x-rays ($25 - 1.2$ Å) with pulse lengths as short as $5 - 10$ fs at a repetition rate of 120 Hz. Recently, the LCLS has also demonstrated the possibility of self-seeding the micro-bunching process with x-ray light initially generated by SASE in the first section of the FEL, significantly increasing the temporal coherence of the emitted x-rays [16].

While these devices have set the bar for peak brightness, there is a growing desire for machines with comparable average beam brightness, but operating at a much higher bunch repetition rate [19]. In machines such as the LCLS, the power lost to the beam(s) is small due to the low repetition rate. Using typical values for the LCLS machine gives a beam loading of:

$$P = I_{\text{beam}} \cdot V \approx 200\ \text{pC/bunch} \times 120\ \text{Hz} \times 12\ \text{GeV} = 288\ \text{W}. \tag{1.4}$$

The limitation of the repetition rate is in part fundamentally set by the power losses in the normal conducting RF (NCRF) cavity walls. While the use of superconducting RF (SRF) cavities would help limit cavity wall losses, the beam loading becomes unmanageable if very high (GHz) repetition rates are sought. For example, to continuously accelerate 77 pC bunches to 5 GeV at 1.3 GHz requires an enormous power supply:

$$P = I_{\text{beam}} \cdot V = 77\ \text{pC/bunch} \times 1.3\ \text{GHz} \times 5\ \text{GeV} = 0.5\ \text{GW}. \tag{1.5}$$

Clearly this is impractical. Thus a significantly different approach to the linac design used to drive a high repetition rate hard x-ray source is required.

1.2.2 The Energy Recovery Linac

To solve the beam loading problem inherent in producing high-brightness, high repetition rate beams, a machine known as an Energy Recovery Linac (ERL) was proposed by Tigner [20] in 1965. A general schematic of this type machine is shown in Fig. 1.4. First, high quality electron bunches are created and initially accelerated to moderate energy (shown in red) in a short linac, known as the *injector*. The beam is then injected into a large linac, and accelerated to high energy (shown in green) by RF fields where it can be used to produce x-ray beams in both undulators and bend sections. After completing one loop

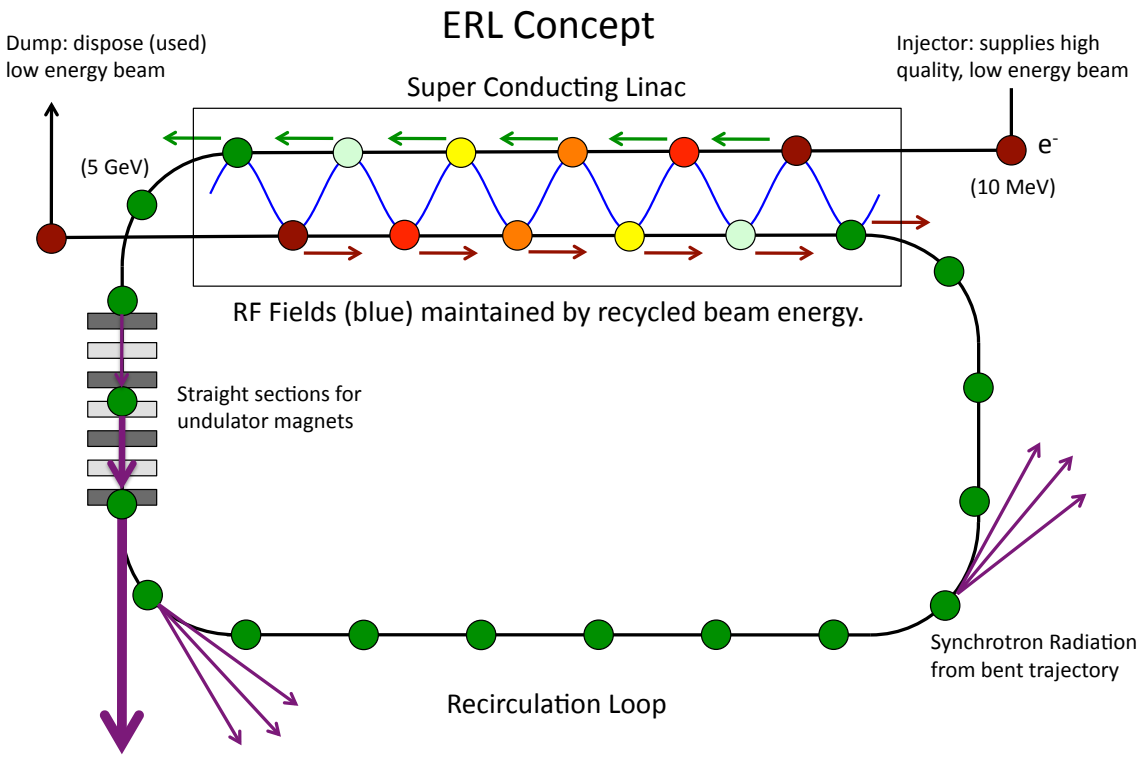

Figure 1.4: The conceptual layout of an Energy Recovery Linac.

around the accelerator, the high energy beam is then sent back into the same RF linac used for acceleration (fields shown in blue). However, the arrival of the recirculated beam is timed so that it is exactly 180 degrees out of phase with the fields in the cavity fields (shown in blue). The beam is then decelerated, and the energy is recovered from the particles and deposited back in the accelerating fields. In order to efficiently recovery the particle's energy, the accelerating cavities must be continuously filled, and the ohmic cavity wall losses must be kept to a minimum. This is accomplished with the use of high quality superconducting RF (SRF) cavities.

Energy recovery has already been experimentally verified at several labs. Examples of operating ERLs include the 135 MeV ERL at Thomas Jefferson Accelerator Facility (Jefferson Lab), a 40 MeV ERL at the Budker Institute of Nuclear Physics (BINP), and the

30 MeV ALICE facility at Daresbury Laboratory [21]. A common feature of these facilities is the use of the ERL to drive an FEL, producing radiation in the Thz to IR/UV spectrum, depending on the available beam energy. Building on the success of these machines, scientists at Cornell University have been designing and developing the technology required to realize a high-energy (GeV), high repetition rate (GHz), hard x-ray ERL [19]. This work includes the design of a high-energy accelerator lattice making use of the existing CESR facility, SRF cavity design and fabrication, the design and testing of a high-brightness DC injector source, as well as laser and cathode research and development. A schematic of the current Cornell ERL design is shown in Fig. 1.5. Table 1.1 shows the relevant simulated

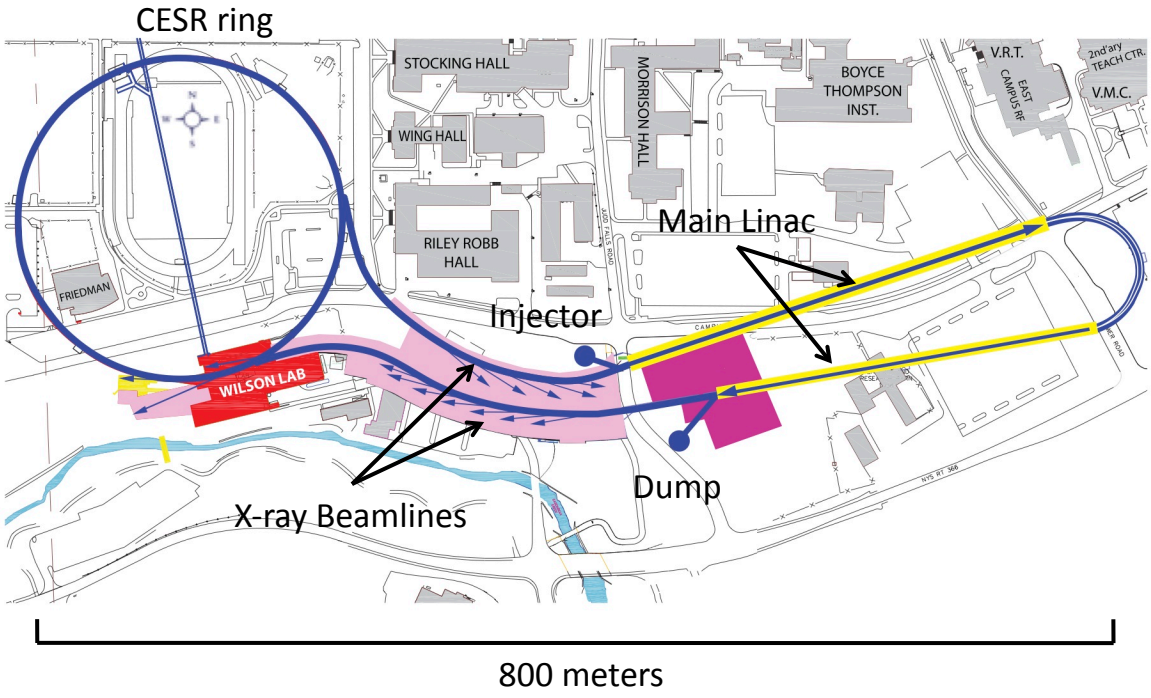

Figure 1.5: The proposed layout for a high energy hard x-ray ERL at Cornell University.

beam parameters determined from complete front-to-end simulations of the accelerator lattice [19].

Table 1.1: Cornell ERL design specifications and parameters.

Parameter	Values
Energy (KE)	5 GeV
Repetition Rate	1.3 GHz
Current (I)	(25) 100 mA
Bunch Charge (q)	(19) 77 pC
Horizontal Emittance (ϵ_x)	13 - 66 pm
Vertical Emittance (ϵ_y)	10 - 25 pm
RMS Bunch Length (σ_t)	0.1 - 2.1 ps
RMS Energy Spread (σ_δ)	0.009 - 0.09 %

The parameters shown in Table 1.1, are based on simulations starting with an exceptional electron source capable of producing high-brightness beams at high repetition rate. The development of such a source, for this application as well as other types of next generation light sources, presents many fundamental physics and technological challenges. As the majority of this work centers on the physics in these state-of-the-art injectors, an overview of modern electron sources is given in the next section.

1.3 High-Brightness Electron Sources

The basic electron source, known as an electron gun or in the case of an accelerator, the injector, can be characterized by three critical properties: the cathode material, the emission process used to generate electrons, and the type of electromagnetic field used to accelerate the extracted electrons. The combination of these properties ultimately sets the physical limits on the quality and quantity of the electron bunches produced.

In general, there are three important types of electron emission processes: thermionic, where electrons are heated off a metal filament; field emission, where electrons are stripped

off a filament via applied large electric fields; and photoelectric, where electrons are emitted from a cathode via the photoelectric. Thermionic sources are widely used, and generally feature a heated (often tungsten) filament. Uses of this type of source include cathode ray tubes, electron microscopes, klystrons, as well as injectors for large scale accelerator facilities [22–25]. Field emission sources have also been used electron microscopes [22]. Photo-emission based guns, the third class of electron guns, represent a relatively new technology, which only recently has become the go to choice for high quality beam production [26].

1.3.1 Photoinjectors and the Physics of Producing High Quality Beams

Initially developed as specialized devices producing polarized electrons for high energy physics, atomic physics, and materials science, photoemission-based guns offer significant flexibility in critical design parameters such as bunch charge, repetition rate, bunch length, and beam energy [26]. There are three main types of photo-emission sources: NCRF guns, SRF guns, and DC guns (followed by SRF acceleration). While each type of source offers particular benefits and potential draw backs, each type of gun ultimately attempts to solve the fundamental problem of producing very bright initial bunches and accelerating them to relativistic energies as quickly as possible. To see why this is necessary, the relevant physics in these machines is discussed below.

One of the dominating effects in high-brightness photoinjectors are the self fields of the beam [27–32]. In general, the interactions between beam particles is comprised of two parts [28]. The first is due to Coulomb forces between neighboring particles, and the second is the effect of the entire beam's charge distribution as a whole. The relative importance of

both these contributions is determined by three fundamental length scales: the Debeye length λ_D, the inter-particle distance l_p, and the beam dimension a [28]. The first of these quantities, the Debye length λ_D, measures the distance over which screening of the fields from a test charge placed in the beam occurs. Collective forces become important when $\lambda_D \ll a$ [28]. In this regime, smooth functions for the self-field effects can be used if $\lambda_D \gg l_p$. For the remainder of this work, it is assumed that this regime holds.

As previously mentioned, one of most important figures of merit for a high-brightness photoinjector is the transverse emittance. Generally in linacs (where the energy may change substantially), the *normalized emittnace* ϵ_n is used. The normalized emittance is related to the geometric emittance defined Eq. (1.3) by $\epsilon_n = \epsilon/(\gamma\beta)$, and gives a measure of the area occupied in either the horizontal or vertical transverse phase spaces (x, p_x) or (y, p_y). While there is no unique definition of emittance used in the literature [28], by far the most common definition used is the *rms* emittance. To motivate the definition of this quantity, the application of Liouville's Theorem to charged particle beams is reviewed.

In general, the motion of electrons in the injector is (classical) Hamiltonian [28]. Subsequently, Liouville's Theorem states that the probability distribution $\rho_{6\mathrm{N}}$ describing an ensemble of particle beams each occupying a point in the 6N-dimensional phase space $(\mathbf{x}, \mathbf{p}) \times N_{\mathrm{beams}}$ is a constant of motion: $d\rho_{6\mathrm{N}}/dt = 0$. Assuming the interactions among particles in each beam of the ensemble can be approximated by average self-fields generated by a continuous distribution of charge, the form of the Hamiltonian describing each beam of the ensemble can be written as a sum over identical single particle Hamiltonians: $\mathcal{H}_{\mathrm{beam}} = \sum_i \mathcal{H}_i$. Consequently, the phase space required to describe the system reduces to the 6D phase space of a single beam: $(\mathbf{x}, \mathbf{p}) \times N_{\mathrm{particles}}$ [33]. The single beam density function in 6D phase space is then denoted $\rho = \rho(\mathbf{x}, \mathbf{p})$, and can be used to represent the number of particles in a small 6D volume [28]: $\mathrm{d}N = N\rho(\mathbf{x}, \mathbf{p})\mathrm{d}^3x\mathrm{d}^3p$. As before,

Liouville's theorem implies $\mathrm{d}\rho/\mathrm{d}t = 0$. Equivalently, the theorem states that the volume in phase space occupied by the beam is a constant of motion.

If there is no coupling between the particle motion in each of the spacial dimensions, then Liouville's Theorem can be applied to the 2D phase spaces in the x, y, and z directions. In this case, the area occupied by the beam in each coordinate phase space is an exact constant of motion. Initially, these areas would seem like prime candidates for the definition of emittance, and in fact many authors use a similar definition [28]. However, this definition does not distinguish between "high quality" beams with "regularly" shaped phase space areas, and ones where the occupied phase space area has become highly distorted in shape due to nonlinear forces (such as space charge). Alternatively, a quantity which does provide this distinction is the *rms* emittance:

$$\epsilon_{n,x} = \frac{1}{mc}\sqrt{\langle x^2\rangle\langle p_x^2\rangle - \langle x p_x\rangle^2}. \tag{1.6}$$

The various moments used here are defined by $\langle ...\rangle = \int (...)\rho_x(x, p_x)\mathrm{d}x\mathrm{d}p_x$, where ρ_x is the normalized particle distribution function in the x-p_x phase space. For a more detailed description of the emittance please see Appendix A.

It is possible to show that the rms emittance is also an invariant of motion, provided the forces acting on the beam are linear. Under this assumption, the map relating the initial phase space coordinates of a particle in the beam to those at some later time t is given by $\mathbf{u}(t) = M \cdot \mathbf{u}(0)$, where $u = (x,\ p_x)^T$, and the *transfer matrix* M is defined by $M_{ij} = \partial u_i(t)/\partial u_j(0)$. The fact that the beam's phase space area is conserved implies

$$A(t) = \int_{\text{final}} \mathrm{d}x\mathrm{d}p_x = \int_{\text{initial}} |\det[M]|\mathrm{d}x\mathrm{d}p_x = \int_{\text{initial}} \mathrm{d}x\mathrm{d}p_x = A(0), \tag{1.7}$$

which implies $\det[M] = 1$. It should be noted that the fact that the the determinant of the transfer matrix is equal to unity is a general consequence of Liouville's theorem, and does

not depend on the forces being linear. The emittance can be expressed as the square root of the determinant of the matrix of second moments. This matrix is defined as

$$\Sigma = \frac{1}{(mc)^2}\langle \mathbf{u}\mathbf{u}^{\mathrm{T}} \rangle = \frac{1}{(mc)^2} \begin{pmatrix} \langle x^2 \rangle & \langle x p_x \rangle \\ \langle x p_x \rangle & \langle p_x^2 \rangle \end{pmatrix}. \tag{1.8}$$

Using the definition of the transfer matrix, it is easy to show $\Sigma(t) = M\Sigma(0)M^{\mathrm{T}}$. Thus the rms emittance at a given time t, and position along the accelerator z, is given by

$$\epsilon_{n,x}^2(t,z) = \det[\Sigma(t)] = \det[M\Sigma(0)M^{\mathrm{T}}] = \det[M]\det[\Sigma(0)]\det[M^{\mathrm{T}}] = \epsilon_{n,x}^2(0). \tag{1.9}$$

The fundamental limit on the emittnace produced in a photoinjector is set by the emittance at the cathode:

$$\epsilon_{n,x,y} = \sigma_{x,y}\sqrt{\frac{\mathrm{MTE}}{mc^2}}. \tag{1.10}$$

In this expression, MTE is the mean transverse energy of the electrons as they are emitted from the cathode and is an intrinsic property of the cathode material. The term $\sigma_{x,y}$ stands for the rms spot size of the laser beam on the cathode. Ideally this emittance would be a constant of motion, however in practice there are many factors which can cause the transverse emittances in a photoinector to grow. The most obvious cause of emittance degradation comes from the violation of the assumption that the fields experienced by the bunch are linear. Sources of non-linear fields include aberration fields from focusing magnets, as well as space charge fields. To reduce aberration effects from magnetic optical elements requires the design of high quality magnets as well as proper alignment of the beam orbit through the resulting fields [34]. To reduce non-linear space charge effects, great care is taken to shape the laser pulse so that the subsequent electron charge distribution extracted from the cathode has predominantly linear self-fields [34, 35].

Assuming both aberration effects and nonlinear space charge fields are controlled, a third source of emittance growth in injectors may be present if the transverse fields acting

on the bunch have a longitudinal dependence along the bunch length. In order to picture this effect, the bunch is sliced transversely at several positions along the direction of motion, as shown in Fig. 1.6. When strong longitudinally dependent transverse forces act on each slice of the bunch, a correlation in the orientation of the phase space area occupied by the particles in each slice may develop. In this case, when these emittances are projected on top of each other, the resulting projected emittance will be significantly larger than the individual slice emittances which are generally on the order of the emittance value set at the cathode. Fig. 1.6 shows how the emittance of different beam slices effect the total *projected* emittance. Unfortunately, it is this *projected emittance* which is the quantity of

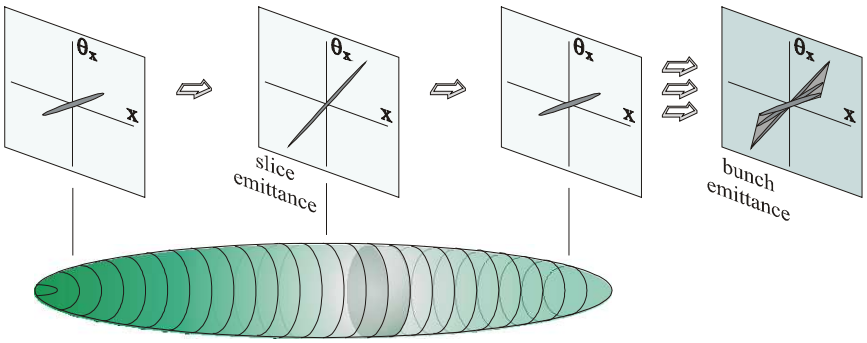

Figure 1.6: Profile of a sliced beam bunch and corresponding slice emittances. θ_x is the divergence of the beam from the beam axis (left to the right): $\theta_x \approx p_x/p_z$.

interest in insertion devices used to generate SR. Space charge forces (particular near the cathode), and time-dependent RF forces both display longitudinal dependence along the bunch length which produce larger projected emittance, and thus have to be compensated if high quality beams are to be produced.

The mitigation of these effects, known as *emittance compensation* [29, 30], is of prime importance in the design of photoinjectors. The effects of the space charge fields are highly energy dependent. In fact, a straight forward calculcation shows that the (linear) transverse force from a uniformly filled cylinder of charge scales with γ^{-3}. Consequently, the effects of

space charge are greatest when the beam has low energy. To counter this effect great effort is taken to accelerate particles emitted from the cathode as rapidly as possible. It follows directly that the accelerating field at the cathode, as well as the mean transverse energy of the electrons emitted, fundamentally set the limit on the emittances produced in photoinjectors, and thus determines the overall electron and photon beam quality in linac based light sources.

1.3.1.1 NCRF Guns

Historically, it was the invention of NCRF guns [36] which solidified the position of photoinjectors as one of the mainstays in the development of new accelerator projects [26]. As previously discussed, it is crucial to minimize the effect of self forces acting on a bunch, particularly at low energies like those occurring right after the bunch is emitted from a cathode. To do this requires supplying as large of an accelerating field as possible at the time of emission. In general, the use of time-dependent fields allows the for a larger voltage to be applied to the initial beam, as compared to DC fields [34]. In this regard, NCRF guns provide the best performance, with accelerating fields of up to 115 MV/m at the cathode having been demonstrated [37].

In terms of average beam power and high duty factor operation, the 433 MHz, 5 MeV NCRF gun built by Boeing and Las Alamos National Laboratory shown in Fig. 1.8(a), remains state-of-the-art to this day [38]. The accelerating gradient delivered at the cathode for this machine was 26 MV/m. Bunches were produced at a 16^{th} of the RF frequency (27 MHz) with a reduced duty factor of 25%. The demonstrated average current of 32 mA from this machine held the world record for highest average current from a photoinjector from 1986 till until 2012 when the Cornell ERL DC photoinjector recently surpassed it [26, 39].

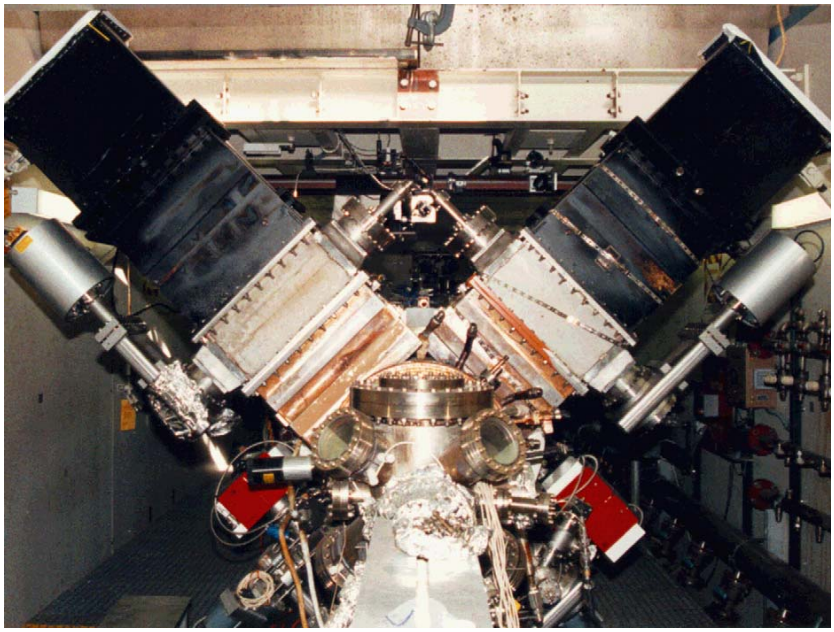

Figure 1.7: Photo of the Boeing/LANL NCRF gun.

One of the factors which limited the use of this gun was the poor vacuum created during operation [38, 39].

For pulsed mode operation, NCRF guns represent the best option for producing high-brightness beams [38]. The injector for the LCLS, as well as FLASH, makes use of a pulsed mode NCRF gun. In this case, very large peak accelerating fields at the cathode have been demonstrated: 115 MV/m for the LCLS and ~ 60 MV/m for FLASH. It should be noted though that these values are not the fields seen by the bunch at emission because these guns must be run with an RF field phase offset. This results in a reduction of the cathode field during emission by a factor of roughly $1/2 - 2/3$. These guns typically operate at significantly lower duty rates (for example 120 Hz at the LCLS), which make them unsuitable for use in an ERL.

Because of this limitation, as well as the effects of ohmic losses in the cavity walls, the demonstration of a high average current NCRF injector operating at 100% duty factor has

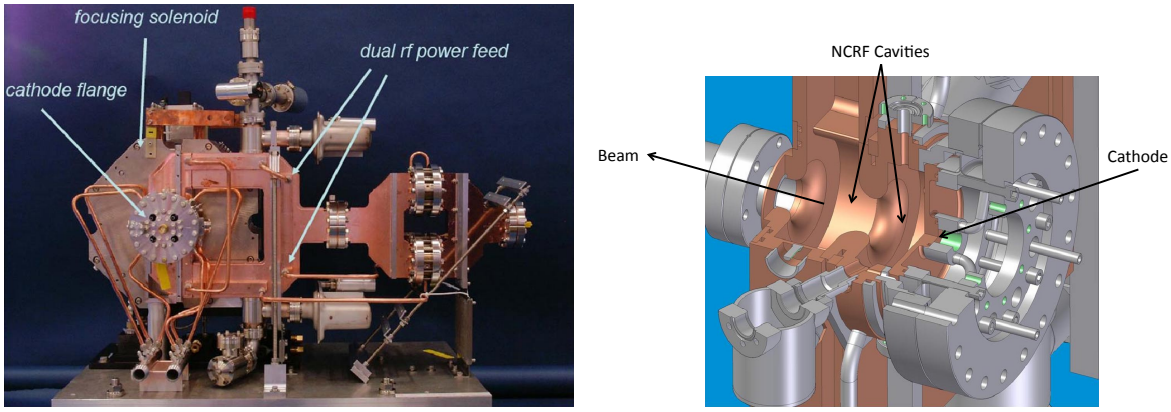

(a) Photo of the LCLS NCRF gun.

(b) Schematic of the LCLS NCRF gun.

Figure 1.8: Examples of a pulsed mode NCRF gun: the LCLS gun.

yet to be realized. A joint effort between Advanced Energy Systems (AES), and LANL has led to the design of 700 MHz NCRF gun to test the feasibility of creating a NCRF source capable of driving a high repetition rate ERL [38]. Unfortunately, the design of such a machine requires the lowering of the field at the cathode to around 7 MV/m, which is within the range of current DC guns [34, 38]. Additionally, scientists at Lawrence Berkeley National Laboratory (LBNL) are currently working on the commissioning of a roughly 186 MHz NCRF gun with cathode fields on the order of 20 MV/m, though full current operation of this machine has not been demonstrated [40].

1.3.1.2 DC Guns

Recent work started at Jefferson Lab and expanded at Cornell University has shown that it is possible to achieve single bunch quality rivaling most NCRF guns, but at much higher (GHz) repetition rates, using a high-voltage DC gun followed by immediately by acceleration in by using a DC electron gun followed by acceleration with SRF cavities [34].

In general, DC guns offer significantly better vacuum then those found in NCRF guns

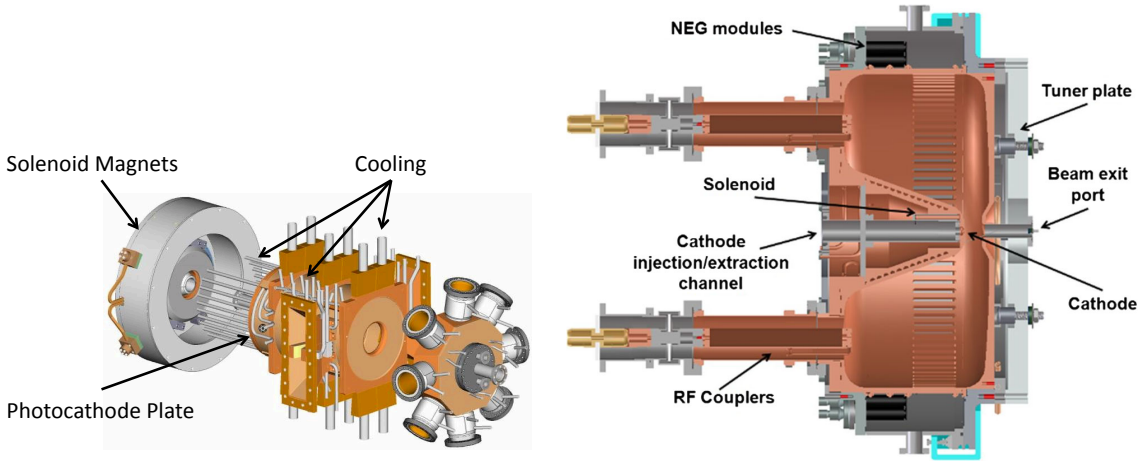

(a) Schematic of the LANL NCRF gun. (b) Schematic of the LBNL NCRF gun.

Figure 1.9: Examples of a cw mode NCRF guns.

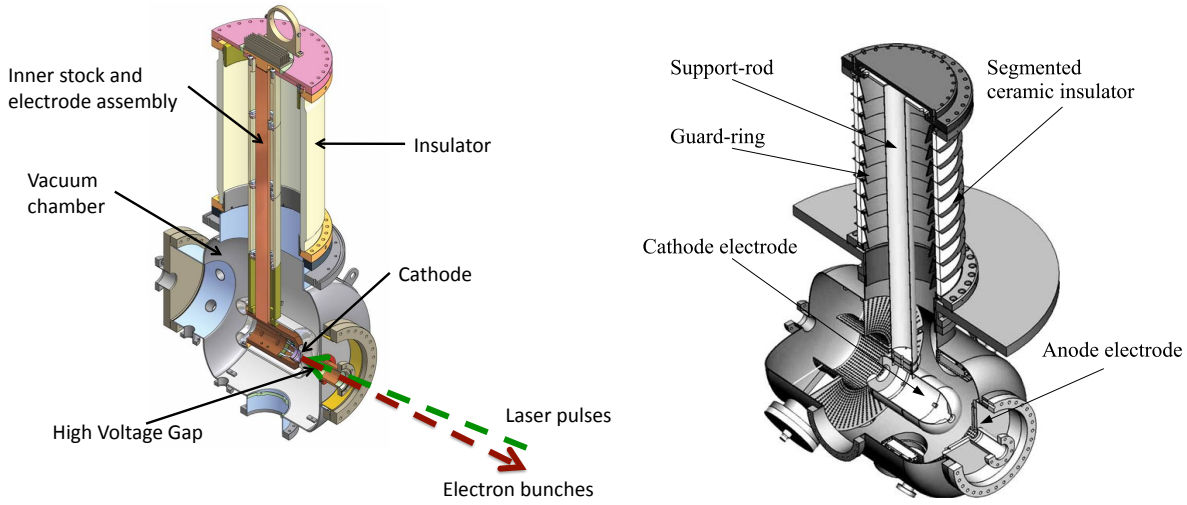

(a) Cornell University DC gun. (b) JAEA/KEK DC gun.

Figure 1.10: Example high-voltage DC guns.

[26], allowing for a wider variety of photocathode materials to be explored. Several labs are currently developing this gun techonology. Examples include, but are not limited to a the 375 kV gun at Jefferson lab, the 350 kV gun at Cornell, and recently a 500 kV gun at

JAEA/KEK laboratory. Fig. 1.10 shows the schematics for the Cornell University and KEK high-voltage DC guns.

Crucial to the performance of these types of machines is the quality and operational integrity of the main ceramic insulator. In both the Jefferson Lab and Cornell guns, the voltage and thus the field at the cathode are limited by the puncture of this ceramic, likely due to field emission events. To overcome this problem, the gun designed and constructed at KEK features a segmented ceramic insulator with metal guard rings to project each insulator segment. Despite the limited voltage achieved, the Cornell gun has recently been used to demonstrate the world record for the highest average beam current from a photoinjector [26], as well as demonstrating record low emittances for DC based photoinjectors with comparable bunch charge (described in Chapter §4) [41]. In addition Cornell scientists are in the process of the fabrication and testing of a new gun featuring a similar segmented insulator design as used in the KEK gun.

1.3.1.3 SRF Guns

In effort to combine the large fields at the cathode provided by NCRF guns, with the excellent vacuum and high repetition rates possible in DC guns, several laboratories are designing SRF guns. SRF gun technology is the most recent of all photoinjector types, with the first electron beam created from an SRF gun being produced by the Forschungszentrum Dresden-Rossendorf (FZD) 1.3 GHz SRF gun in 2002 [42]. Another notable example of an SRF gun under development is the 703 MHz gun being designed and built as a joint venture between AES and Brookhaven National Laboratory (BNL) shown in Fig. 1.11(b). This machine is designed to produce very high currents (500 mA). In order to do so, an excellent vacuum must be maintained, and extremely efficient photocathodes must be

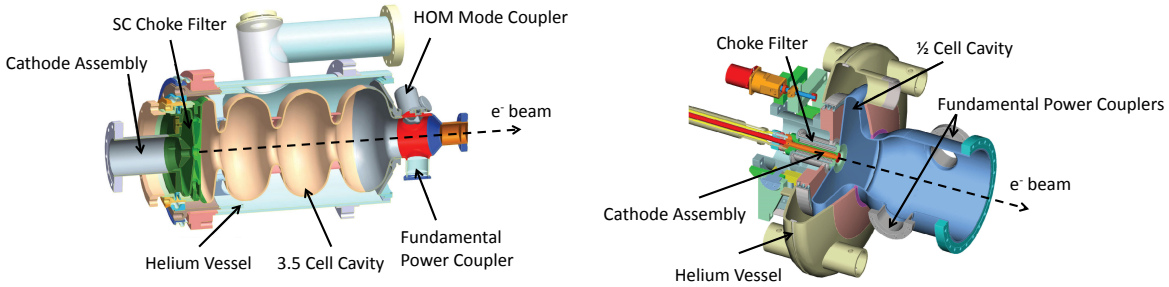

(a) Schematic of the 1.3 GHz FZD SRF gun. (b) Schematic of the 703 MHz AES-BNL SRF gun.

Figure 1.11: Example SRF guns.

developed. Additionally, two input power couplers capable of delivering 500 kW of power to the gun must be demonstrated. This program has made great strides toward demonstrating the principles of this design, though no beam running has been demonstrated yet [42].

While the use of superconducting technology significantly lowers the ohmic losses in the cavity walls, several design challenges remain in demonstrating the viability of these sources. One of the fundamental challenges facing these machines is the introduction of the photocathode into the SRF cyro-environment. This leads to multipacting and vacuum concerns. Other issues include, but are not limited too, the design of high power input couplers, and in particular, minimizing the kicks to the beams generated by asymetric fields in the coupler lines, and controlling the production of higher-order modes (HOMs) which are produced in high quality cavities.

1.4 Overview

Having described the motivation behind the development and construction of fourth generation linac based light sources such as FELs and ERLs, as well as the basic physics

in the electron injectors used to drive these machines, we now turn to the three main contributions to the field of photoinjectors presented in this work. These contributions take the form of the remaining three chapters. The first two chapters deal with theoretical and computational considerations dealing with the transport of low energy beams through RF fields. Chapter §2 gives a semi-analytic approach to computing the linear transfer matrix through combined cylindrically symmetric RF and solenoid fields. The resulting analytic matrix for a small integration step clearly demonstrates the physics of single particle motion in these fields and correctly maintains the symplecticity arising from the Hamiltonian nature of this motion. These results are relevant to any combined RF and solenoid field set-up, and can be used to simulate linear dynamics in DC guns, NCRF guns, and SRF guns.

Chapter §3 gives a complete method for creating realistic 3D RF cavity field maps which include the time-dependent focusing of coaxial input power couplers. The method detailed in this chapter extends previous results so that coupler focusing can be quantified and simulated for non-relativistic beam energies, thus making it of particular relevance to RF gun and injector design and simulation.

Finally, Chapter §4 gives the results of a detailed investigation of the six dimensional electron beam phase space in the Cornell ERL injector prototype. Incorporating the results of Chapters §2 and§3, a complete simulation model of the injector was constructed, verified by measurement, and optimized. The results of the direct measurements of the tranverse vertical and horizontal phase spaces, the time-resolved phase space, and the energy spread of the beam are given and compared to simulation. Overall, excellent agreement was found between measurement and simulation. These results set a new record for low emittances in a DC photoinjector for comparable bunch charges, and represent a milestone in the advancement of DC based high-brightness photoinjectors.

CHAPTER 2

A New Method for Generating Linear Transfer Matrices through Combined RF and Solenoid Fields

Originally published as: C. Gulliford and I. Bazarov, Phys. Rev. ST Accel. Beams **15**, 024002 (2012) [43].

2.1 Abstract

We present a new method for computing the transverse transfer matrix for superimposed axisymmetric RF and solenoid field maps. The algorithm constructs the transfer matrix directly from one-dimensional RF and solenoid field maps without computing numerical derivatives or eigenfunction expansions of the field map data. In addition, this method accurately describes the dynamics of low energy particles starting from a solenoid-immersed cathode, allowing the method to simulate transport through both RF and electrostatic guns. Comparison of particle tracking with the transfer matrix, and direct integration of the equations of motion through several field set-ups, shows excellent agreement between the two methods.

2.2 Introduction

Linear transfer matrices continue to serve as important simulation tools in the design, commissioning, and operation of modern accelerators. Common examples of their use include the computation of linear centroid motion, beam-based alignment of optical elements, and orbit feedback. In addition, they feature prominently in the theory of round-to-flat beam transforms in RF and DC guns [44, 45], and are used for emittance measurements for beams without space charge [46]. Because of this utility, analytic expressions for the transfer matrix through many beam line elements, such as magnets with constant fields, are well known and are widely used. In contrast to these simple elements, the fields of many beam line elements in modern accelerators have no analytic form and may overlap each other. For example, in high brightness electron sources, solenoid fields used for emittance compensation may overlap the accelerating fields at or near the cathode. To properly describe the dynamics in these machines, the transfer matrix through superimposed RF and solenoid fields must be constructed. In general, to model these elements, one must use numerically computed electromagnetic field maps. Unfortunately, no closed form solutions for the transfer matrix through such elements exist.

Nonetheless, a significant amount of work has gone into developing both semi-analytic and numerical techniques to compute these matrices. In general, these techniques require some form of manipulation of the field map data and often have a limited range of validity. For example, the widely used RF transfer matrix given by Rozensweig and Serafini [47] requires a Floquet expansion of the on-axis RF field map, and is only valid for ultra-relativistic particles. Other methods expand the field map data in terms of the the general solution to the homogeneous Maxwell equations in cylindrical coordinates [48, 49]. From this expansion, the vector potential can be computed, allowing the Hamiltonian for

the overlapping solenoid and RF fields to be constructed. When combined with differential and Lie algebra techniques, this method is quite powerful and can be used to generate arbitrary order maps. Despite this, it requires significant overhead in setting up, and it may not be suitable for online modeling purposes. A simpler solution has been put forth in [50]. In this approach, the particle energy and RF fields are assumed constant over a small time step. The second order linear transverse equations of motion can then be solved 'exactly,' and the transfer matrix for the time step constructed. While this method works well for relativistic particles, it does have several draw backs. First, the assumption that the energy is constant requires extremely small time steps for very low energy particles like those emitted from a photocathode. Second, the determinant of the resulting transfer matrix is only correct to first order in the step size. Another simple approach is given in [51, 52], and makes use of the "Equivalent Field" concept. While this method guarantees the correct determinant of the transfer matrix, it assumes a constant velocity over each integration step and is therefore not valid for very low particle energies. Alternatively, one can also compute the transfer matrix elements from the equations of motion directly using numerical integration [53]. In general, this requires computing numerical derivatives of the field maps (or differentiating orbits). Additionally, in order to properly capture the dynamics of the problem, some care must be taken to ensure the integrator used truly maintains symplecticity [54].

To our knowledge, there is currently no simple, inherently symplectic method of computing the transfer matrix directly from superimposed RF and solenoid field maps for low particle energies. Because no analytic solution for the transfer matrix through the field of an entire RF cavity or solenoid exists, any attempt at constructing a simple algorithm for low energy dynamics will require multiple steps. Given the availability of numerical integrators, any new algorithm must satisfy the following three requirements in order to be

useful: (i) using reasonable step sizes, the method should be able to describe the low energy dynamics found in RF or DC guns; (ii) the method should generate matrices with the correct determinant, regardless of the step size; and (iii) the method for constructing the transfer matrix should be easy to implement. Based on a new analytic solution to the equations of motion, we derive a transfer matrix algorithm with all three of these qualities.

The layout of this work is as follows. First, the longitudinal equations of motion are solved for a single small step in the independent variable. Then, the transfer matrix over the same step is derived for electrostatic and solenoid fields. Building on this result, the matrix for combined RF and solenoid fields is computed. This matrix is then tested with tracking through a DC gun, a superconducting RF cavity and a RF gun with a solenoid immersed cathode. Excellent agreement between the transfer matrix and direct integration of the equations of motion is demonstrated in all three cases.

2.3 Notation and the Equations of Motion

In this section the variables, notation, and the equations of motion used throughout this work are defined. In general, both standing and traveling wave RF fields can be written in the complex form $\mathbf{E} = \tilde{\mathcal{E}}(x, y, z)e^{i\omega t}$ and $\mathbf{B} = \tilde{\mathcal{B}}(x, y, z)e^{i\omega t}$. In these and all subsequent expression, tildes are used to denote phasor quantities. The coordinate system for the fields is set up so that the z-axis points along the length of the beamline. The functions $\tilde{\mathcal{E}}$ and $\tilde{\mathcal{B}}$ represent the field maps generated by RF cavity field solvers and include the initial phase offset of the cavity. For notational simplicity, the phase factor $e^{i\omega t}$ and the real symbol Re[...] are suppressed in all but the final results for the transfer matrix. To derive the linear equations of motion, the fields are expanded to first order in the transverse offsets x and y.

The linearized RF fields take the form

$$\tilde{\mathcal{E}}(x,y,z) = -\frac{x}{2}\left(\frac{d\tilde{\mathcal{E}}_z}{dz}\right)\hat{\mathbf{x}} - \frac{y}{2}\left(\frac{d\tilde{\mathcal{E}}_z}{dz}\right)\hat{\mathbf{y}} + \tilde{\mathcal{E}}_z(r=0)\hat{\mathbf{z}},$$
$$\tilde{\mathcal{B}}(x,y,z) = -\frac{y}{2}\left(\frac{i\omega}{c^2}\right)\tilde{\mathcal{E}}_z\hat{\mathbf{x}} + \frac{x}{2}\left(\frac{i\omega}{c^2}\right)\tilde{\mathcal{E}}_z\hat{\mathbf{y}}. \tag{2.1}$$

Similarly, the expansion of the solenoid field gives

$$\mathbf{B}_{\text{sol}} = -\frac{x}{2}\left(\frac{dB_z}{dz}\right)\hat{\mathbf{x}} - \frac{y}{2}\left(\frac{dB_z}{dz}\right)\hat{\mathbf{y}} + B_z(r=0)\hat{\mathbf{z}}. \tag{2.2}$$

Note that the solenoid field is distinguished from the RF magnetic field by the lack of a tilde. The total physical fields are given by $\mathbf{E}_{\text{tot}} = \text{Re}[\tilde{\mathcal{E}}e^{i\omega t}]$ and $\mathbf{B}_{\text{tot}} = \text{Re}[\tilde{\mathcal{B}}e^{i\omega t}] + \mathbf{B}_{\text{sol}}$.

For the single particle equations of motion, the longitudinal coordinate z is used as the independent variable. Derivatives with respect to z are denoted with a prime: $f' \equiv df/dz$. The equations of motion for the longitudinal phase space variables t and γ are

$$t' = \frac{1}{\beta(z)c}, \qquad \tilde{\gamma}'(z) = \frac{e\tilde{\mathcal{E}}_z}{mc^2} = \tilde{\mathcal{E}}_z/\mathcal{E}_e, \qquad \gamma' = \text{Re}[\tilde{\gamma}'e^{i\omega t}]. \tag{2.3}$$

Here the constant $\mathcal{E}_e = mc^2/e$ gives the (signed) rest energy of the electron in [eV]. The normalized energy is given by $\gamma = \text{Re}[\tilde{\gamma}e^{i\omega t}]$. The transverse equations of motion can be written as [28, 55]:

$$x'' + \frac{p'}{p}x' + \left(\frac{\gamma\tilde{\mathcal{E}}_z'}{2\mathcal{E}_e p^2} + \frac{i\omega\tilde{\gamma}'}{2cp}\right)x + 2\Delta\theta_L' y' - \left(\frac{cB_z'}{2\mathcal{E}_e p}\right)y = 0, \tag{2.4}$$
$$y'' + \frac{p'}{p}y' + \left(\frac{\gamma\tilde{\mathcal{E}}_z'}{2\mathcal{E}_e p^2} + \frac{i\omega\tilde{\gamma}'}{2cp}\right)y - 2\Delta\theta_L' x' + \left(\frac{cB_z'}{2\mathcal{E}_e p}\right)x = 0. \tag{2.5}$$

In this expression, $p = \beta\gamma$ is the normalized reference particle momentum, and $\Delta\theta_L$ is the Larmor angle, defined by

$$\Delta\theta_L(z) = -\int_{z_i}^{z} \frac{cB_z}{2\mathcal{E}_e p}dz, \qquad \Delta\theta_L' = -\frac{cB_z}{2\mathcal{E}_e p}. \tag{2.6}$$

Note the use of a negative sign in front of the integral. With this definition, a positive solenoid field creates a positive change in the Larmor angle for electrons. Decoupling these equations requires rotating to the Larmor frame. By defining the variable $\eta = x + iy$, the transformation to Larmor coordinates takes the form [55]:

$$\eta_L(z) = x_L + iy_L = \eta e^{-i\Delta\theta_L(z)}. \tag{2.7}$$

The equivalent transformation for the transverse phase space vector $\mathbf{u} = (x \;\; x' \;\; y \;\; y')^T$ is defined by

$$\begin{pmatrix} x_L \\ x'_L \\ y_L \\ y'_L \end{pmatrix} = \begin{pmatrix} C & 0 & S & 0 \\ -\Delta\theta'_L S & C & \Delta\theta'_L C & S \\ -S & 0 & C & 0 \\ -\Delta\theta'_L C & -S & -\Delta\theta'_L S & C \end{pmatrix} \begin{pmatrix} x \\ x' \\ y \\ y' \end{pmatrix}. \tag{2.8}$$

In this and following expressions, $C \equiv \cos\Delta\theta_L$, and $S \equiv \sin\Delta\theta_L$. The matrix in this equation is denoted by $L = L(\Delta\theta_L, \Delta\theta'_L)$. It is easy to show that the determinant of this matrix is equal to unity. Another important characteristic of this matrix is found by taking the limit as $z \to z_i$. In this limit, $\Delta\theta_L \to 0$, and the matrix reduces to

$$L(0, \Delta\theta'_L(z_i)) = \begin{pmatrix} 1 & 0 & 0 & 0 \\ 0 & 1 & \Delta\theta'_L(z_i) & 0 \\ 0 & 0 & 1 & 0 \\ -\Delta\theta'_L(z_i) & 0 & 0 & 1 \end{pmatrix}. \tag{2.9}$$

The two remaining focusing terms describe the effect of starting a particle with $B_z(z_i) \neq 0$, the so-called "immersed cathode" condition.

Substituting the transformation in Eq. (2.7) into Eqs. (2.4) and (2.5) gives the transverse equation of motion for the Larmor coordinates:

$$\eta''_L + \frac{p'}{p}\eta'_L + \left(\frac{\gamma\tilde{\mathcal{E}}'_z}{2\mathcal{E}_e p^2} + \frac{i\omega\tilde{\gamma}'}{2cp} + (\Delta\theta'_L)^2 \right) \eta_L = 0. \tag{2.10}$$

In this expression η_L stands for either x_L and y_L. Because the transformation between the laboratory and Larmor coordinates is known, all that remains is solving the above differential equation. With this solution, the transfer matrix for the lab phase space variables follows directly: $M(z_i \to z_f) = L^{-1}(z_f) M_L(z_i \to z_f) L(z_i)$. Consequently, the majority of this work is spent finding an exact solution to Eq. (2.10) within the approximation that the fields are constant over a small step in z. Because all of the following derivations are carried out in the Larmor frame, the subscript 'L' on the transverse variables is suppressed in the remainder of this work.

2.4 Derivation of the Transfer Matrix

As stated before, general solutions to the differential equations in Eqs. (2.3), (2.6), and (2.10), do not exist for arbitrary cavity and solenoid fields. As a result, any method for computing the transfer matrix analytically requires some form of approximation to these equations. The approach taken in this work is to find an exact solution to the equations of motion for a step in z and t that is small enough so that the field profiles $\tilde{\mathcal{E}}_z(z)$ and $\tilde{\mathcal{B}}_z(z)$, as well as the RF phase, don't change appreciably. The solution is exact in the sense that the particle energy changes correctly over the course of the step. The change in the field map profile as well as the RF phase are then included with the use of edge-focusing matrices. Slicing the field maps and consecutively multiplying the matrices for each step gives the total transfer matrix:

$$M(z_i \to z_f) \approx \prod_k \Delta M(z_k \to z_k + \Delta z). \tag{2.11}$$

The first step in constructing the transfer matrix for one step is to solve the longitudinal

equations of motion in Eq. (2.3). To do so the electric and magnetic fields are assumed constant and equal to their average value over the step from z_i to z_f:

$$\mathcal{E}_z(z) \cong \langle \mathcal{E}_z \rangle, \qquad B_z(z) \cong \langle B_z \rangle. \tag{2.12}$$

For a constant electric field, $\gamma' \cong \langle \mathcal{E}_z \rangle / \mathcal{E}_e$ is constant, and the normalized energy, momentum, and velocity are given by

$$\gamma(z) = \gamma_i + \gamma'(z - z_i), \quad p(z) = \sqrt{(\gamma_i + \gamma'(z - z_i))^2 - 1}, \quad \beta(z) = p(z)/\gamma(z). \tag{2.13}$$

Using these expressions, the derivatives of $t(z)$ and $\Delta\theta_L$(z) in Eqs. (2.3) and (2.6) can be directly integrated:

$$t(z) = \frac{1}{c\gamma'}[p(z) - p_i], \tag{2.14}$$

$$\Delta\theta_L(z) = \left(\frac{b}{\gamma'}\right) \ln\left(\frac{p(z) + \gamma(z)}{p_i + \gamma_i}\right). \tag{2.15}$$

In the last line, the constant b is the normalized solenoid field defined as $b = p \cdot \Delta\theta'_L = -e\langle B_z \rangle / 2mc$ [56] . Note that the expression for time given here is essentially the same as Eq. (7) in [31]. For simplicity and speed, we take the average values here to be equal to the fields evaluated at the midpoint of the step. In addition to defining the transformation between the lab and Larmor coordinates, the function $\Delta\theta_L$ plays an important role in the derivation of the transfer matrix for both the electrostatic and RF field cases.

2.4.1 Overlapping Electrostatic and Solenoid Fields

The derivation of the transfer matrix for superimposed RF and solenoid fields is based in part on the method used to derive the transfer matrix for static fields [46]. In this section, a detailed derivation of the static field result is given. The same techniques are then

modified and used to derive the RF matrix in the following section. For static fields, the equation of motion is found by taking $\omega \to 0$ in Eq. (2.10):

$$\eta'' + \frac{p'}{p}\eta' + \left(\frac{\gamma \mathcal{E}_z'}{2\mathcal{E}_e p^2} + (\Delta\theta_L')^2\right)\eta = 0. \tag{2.16}$$

Note that $p' \propto \langle \mathcal{E}_z \rangle$ and $\Delta\theta_L' \propto \langle B_z \rangle$ in this expression, implying η depends on both the accelerating field and its gradient, as well as the solenoid field. The transfer matrix from z_i to $z_f = z_i + \Delta z$ is derived in a three-step process. Over the interval $[z_i, z_f]$, the electric and magnetic fields are approximated as rectangular step functions. Formally the fields are written as:

$$\begin{aligned}
\mathcal{E}_z(z) &\cong \langle \mathcal{E}_z \rangle \left\{\theta(z - z_i) - \theta(z - z_f)\right\}, \quad \mathcal{E}_z' \cong \langle \mathcal{E}_z \rangle \left\{\delta(z - z_i) - \delta(z - z_f)\right\}, \\
B_z(z) &\cong \langle B_z \rangle \left\{\theta(z - z_i) - \theta(z - z_f)\right\}, \quad B_z' \cong \langle B_z \rangle \left\{\delta(z - z_i) - \delta(z - z_f)\right\},
\end{aligned}$$

where $\theta(z)$ is the Heaviside step function, and $\delta(z)$ is the Dirac delta function. The transfer matrix is then found by solving the transverse equation of motion piecewise from z_i to z_f.

First, the equations of motion are integrated across the rising edge of the electric field at z_i. Because the rising edge is approximated as an instantaneous step, the particle's position does not change: $\eta(z_i^+) = \eta(z_i^-) = \eta(z_i)$. Integrating the equation of motion gives the kick delivered to the particle's trajectory [47, 56]:

$$\begin{aligned}
\Delta\eta' &= -\int_{z_i-\epsilon}^{z_i+\epsilon} \left\{\frac{p'}{p}\eta' + \left(\frac{\gamma \mathcal{E}_z'}{2\mathcal{E}_e p^2} + (\Delta\theta_L')^2\right)\eta\right\} \mathrm{d}z \\
&= -\int_{z_i-\epsilon}^{z_i+\epsilon} \frac{\langle \mathcal{E}_z \rangle}{2\gamma\beta^2\mathcal{E}_e}\eta(z)\delta(z - z_i)\mathrm{d}z \\
&= -\frac{\gamma'}{2\gamma_i\beta_i^2}\eta(z_i).
\end{aligned}$$

The corresponding transfer matrix for the rising edge, R_E, takes the form

$$R_E(\gamma, \gamma') = \begin{pmatrix} 1 & 0 \\ -\frac{\gamma'}{2\gamma\beta^2} & 1 \end{pmatrix}.$$

Next, the equation of motion is solved across the interval (z_i, z_f), where both the electric and magnetic field are approximately constant. In this region, the equation of motion reduces to

$$\eta'' + \frac{\gamma'}{\gamma\beta^2}\eta' + (\Delta\theta_L')^2\eta = 0, \tag{2.17}$$

where $\Delta\theta_L'(z) \propto 1/p(z)$. With the electric field held constant, γ, p, β, and $\Delta\theta_L$ are given by Eqs. (2.13) and (2.15). With these functions, the differential equation can be solved by assuming $\eta = \eta(\Delta\theta_L)$. Plugging this into Eq. (2.17) gives

$$(\Delta\theta_L')^2\left[\frac{d^2\eta}{d\theta_L^2} + \eta\right] + \frac{d\eta}{d\theta_L}\left[\Delta\theta_L'' + \frac{\gamma'}{\gamma\beta^2}\Delta\theta_L'\right] = 0. \tag{2.18}$$

Using Eq. (2.15), it is possible to show $\Delta\theta'' = -\gamma'\Delta\theta'/\gamma\beta^2$, canceling the second term in the above equation. Assuming $\Delta\theta' \neq 0$, the first term in this expression must also vanish. It follows that: $\eta = A\cos\Delta\theta_L + B\sin\Delta\theta_L$. Completing the initial value problem for this solution determines the transfer matrix for the step from z_i to z_f:

$$M_{i\to f} = \begin{pmatrix} C & \frac{p_i}{b}S \\ -\frac{b}{p_f}S & \frac{p_i}{p_f}C \end{pmatrix}. \tag{2.19}$$

In this and following expressions, $C \equiv \cos(\Delta\theta_L(z))$, and $S \equiv \sin(\Delta\theta_L(z))$.

The last step in constructing the full matrix for the interval $[z_i, z_f]$ is to evaluate the transfer matrix for the falling edge of the accelerating field. The result is essentially the same as before, except now the derivative of the electric field has the opposite sign. This allows the transfer matrix for the falling edge to be written as

$$R_E^{-1}(\gamma, \gamma') = \begin{pmatrix} 1 & 0 \\ \frac{\gamma'}{2\gamma\beta^2} & 1 \end{pmatrix}. \tag{2.20}$$

Combining the three matrices for each region gives the full transfer matrix for the step Δz:

$$\begin{aligned} \Delta M_{x,x'}^{\mathrm{dc}} &= R_E^{-1}(\gamma_f, \gamma')M_{i\to f}R_E(\gamma_i, \gamma') \\ &= \begin{pmatrix} 1 & 0 \\ \frac{\gamma'}{2\gamma_f\beta_f^2} & 1 \end{pmatrix}\begin{pmatrix} C & \frac{p_i}{b}S \\ -\frac{b}{p_f}S & \frac{p_i}{p_f}C \end{pmatrix}\begin{pmatrix} 1 & 0 \\ -\frac{\gamma'}{2\gamma_i\beta_i^2} & 1 \end{pmatrix}. \end{aligned} \tag{2.21}$$

One important thing to note about the matrix in Eq. (2.21) is that it has the correct determinant for the phase space variables chosen: $\det(\Delta M^{\mathrm{dc}}_{x,x'}) = p_i/p_f$. The transfer matrix for the canonical phase space variables x_L and $p_{x,L}$ can be found by applying the transformation:

$$\Delta M^{\mathrm{dc}}_{x,p_x} = \begin{pmatrix} 1 & 0 \\ 0 & p_f \end{pmatrix} \Delta M^{\mathrm{dc}}_{x,x'} \begin{pmatrix} 1 & 0 \\ 0 & 1/p_i \end{pmatrix}. \tag{2.22}$$

It follows from this expression that the matrix $\Delta M^{\mathrm{dc}}_{x,p_x}$ satisfies the symplectic condition $\det(\Delta M^{\mathrm{dc}}_{x,p_x}) = 1$. In addition to this, the transfer matrix also has the convenient feature that the derivative of the accelerating field never has to be calculated, bypassing the need to compute derivatives numerically. It is important to note that the rising-edge matrix should not be included in Eq. (2.21) when the electric field is nonzero at the initial position of the reference particle. Including the edge matrix in this case is equivalent to a particle seeing the field rise from zero to the actual value at the initial reference position. For particles starting from a cathode, this is not physical. Similarly, the falling edge matrix should not be included when tracking of the reference particle stops in a region of nonzero electric field.

2.4.2 Overlapping RF and Solenoid Fields

With the results for the electrostatic field determined, it is now possible to construct the transfer matrix for RF fields. The approximation used here is similar to that used in the electrostatic case: the field profiles $\tilde{\mathcal{E}}_z$ and B_z, as well as the RF phase, are assumed constant over the step Δz. This implies $\tilde{\gamma}(z,t)$ is also constant, allowing the solutions to the longitudinal equations of motion in Eq. (2.13) to be used. Over the interval (z_i, z_f), the general equation of motion in Eq. (2.10) reduces to

$$\eta'' + \frac{\tilde{\gamma}'}{\gamma\beta^2}\eta' + \left(\frac{i\omega\tilde{\gamma}'}{2cp} + (\Delta\theta_L')^2\right)\eta = 0. \tag{2.23}$$

Because the RF magnetic focusing term proportional to ω scales as p^{-1} and not $p^{-2} \propto (\Delta\theta_L')^2$, the solution to the equation of motion used in the electrostatic case is no longer valid. In the constant field and phase approximation, this term introduces a square root of a quadratic in z into the equation of motion: $p^{-1} = [(\gamma_i + \gamma'\Delta z)^2 - 1]^{-1/2}$. The presence of this factor makes this equation difficult to solve. To our knowledge no analytic solution exists.

In order to proceed, the RF magnetic focusing term must be removed from Eq. (2.23). Changing variables to reduced coordinates, defined by $\hat{\eta} = \sqrt{\beta\gamma}\eta$, provides a clue as to how to remove this term. To see this requires transforming the general equation of motion in Eq. (2.10) first, and then making the constant field and phase approximation. The general equation of motion for the reduced variables is [55, 56]:

$$\hat{\eta}'' + \left[\frac{(\tilde{\gamma}')^2(\gamma^2+2)}{4(\gamma^2-1)^2} - \frac{i\omega\tilde{\gamma}'}{2cp^3} + (\Delta\theta_L')^2\right]\hat{\eta} = 0. \tag{2.24}$$

Unfortunately, the RF magnetic focusing term, now proportional to p^{-3}, still contains a square root in the denominator, and the reduced equation of motion does not have an analytic solution. It is important to note, however, that switching to the reduced variables effectively removes the RF *electric* contribution (the term proportional to $\mathcal{E}_z'$) to the focusing function [56]. This implies that a similar variable transformation can be used to eliminate the RF magnetic focusing term. It turns out that such a transformation is possible, and requires switching the independent variable from longitudinal position to time. Doing so yields the equivalent equation of motion:

$$\ddot{\eta} + \frac{\dot{\tilde{\gamma}}}{\gamma}\dot{\eta} + \left[\frac{c^2\tilde{\mathcal{E}}_z'}{2\gamma\mathcal{E}_e} + c\beta\frac{i\omega\tilde{\gamma}'}{2\gamma} + (\Delta\dot{\theta}_L)^2\right]\eta = 0. \tag{2.25}$$

Next, the coordinates are transformed to the new reduced variables defined by $\bar{\eta} = \sqrt{\gamma}\eta$. In matrix form, this transformation is written as

$$\begin{pmatrix} \bar{\eta} \\ \dot{\bar{\eta}} \end{pmatrix} = \Lambda T \begin{pmatrix} \eta \\ \eta' \end{pmatrix}, \quad T(\beta) = \begin{pmatrix} 1 & 0 \\ 0 & c\beta \end{pmatrix}, \quad \Lambda(\gamma, \dot{\tilde{\gamma}}) = \sqrt{\gamma}\begin{pmatrix} 1 & 0 \\ \frac{\dot{\tilde{\gamma}}}{2\gamma} & 1 \end{pmatrix}. \tag{2.26}$$

As before, the equation of motion for the reduced variables takes the form of Hill's equation:

$$\ddot{\bar{\eta}} + \left[\frac{\dot{p}^2(p^2-2)}{4(p^2+1)^2} + \frac{c^2\tilde{\mathcal{E}}_z'}{2\gamma^3\mathcal{E}_e} + (\Delta\dot{\theta}_L)^2\right]\bar{\eta} = 0. \tag{2.27}$$

Comparing Eqs. (2.24), and (2.27) shows that switching the independent variable and using the new reduced coordinates effectively exchanges the roles of the functions γ and p. Additionally, switching between the two sets of reduced coordinates allows one to choose which of the two RF focusing terms to hide in the variable transformation.

With the new definition of the reduced coordinates, all that remains now is to solve Eq. (2.27) in the region where the solenoid and accelerating fields are constant. This requires knowing the functions $p(t)$ and $\gamma(t)$. The momentum is easily found by rearranging Eq. (2.14): $p(t) = p_i + c\gamma'(t - t_i)$. The normalized energy is then given by $\gamma(t) = \sqrt{p^2(t)+1}$. Inserting these expressions into the equations of motion in the constant field region yields:

$$\ddot{\bar{\eta}} + \left[\frac{(c\tilde{\gamma}')^2(p^2-2)}{4(p^2+1)^2} + \frac{(bc)^2}{p^2+1}\right]\bar{\eta} = 0. \tag{2.28}$$

Note that by approximating the fields as constant after changing variables, the RF electric focusing term proportional to $\tilde{\mathcal{E}}_z'\gamma^{-3}$ in Eq. (2.27) is set to zero in the transformed equation of motion. This eliminates the presence of any square roots in the resulting focusing function, and effectively breaks the normal equivalence between using the two sets of independent variables and reduced coordinates.

Eq. (2.28) can be solved with the function $\bar{\eta} = \sqrt{\gamma}(A\cos\Delta\theta_L + B\sin\Delta\theta_L)$. The transfer matrix is found by completing the initial value problem for this solution. The resulting matrix can be written in the compact form

$$\bar{M}^{\mathrm{rf}}_{i\to f} = \Lambda(\gamma_f, \dot{\tilde{\gamma}}_f)T(\beta_f)M^{\mathrm{dc}}_{i\to f}T^{-1}(\beta_i)\Lambda^{-1}(\gamma_i, \dot{\tilde{\gamma}}). \tag{2.29}$$

In this expression $\dot{\tilde{\gamma}}_f = c\beta_f\tilde{\gamma}'$. The matrix in Eq. (2.29) correctly describes the evolution

of the reduced variables. In order to get the transfer matrix for the usual phase space variables, it must be transformed back:

$$M^{\mathrm{rf}}_{i\to f} = T^{-1}(\beta_f)\Lambda^{-1}(\gamma_f, \dot{\tilde{\gamma}}_f e^{i\omega\Delta t})\Lambda(\gamma_f, \dot{\tilde{\gamma}}_f)T(\beta_f)M^{\mathrm{dc}}_{i\to f}. \tag{2.30}$$

It is clear from this expression that the effects of the RF magnetic focusing must be contained in the matrices left multiplying $M^{\mathrm{dc}}_{i\to f}$. Combining these matrices together gives

$$R_{\mathrm{rf}} = T^{-1}(\beta)\Lambda^{-1}(\gamma, \dot{\tilde{\gamma}}e^{i\omega\Delta t})\Lambda(\gamma, \dot{\tilde{\gamma}})T(\beta) = \begin{pmatrix} 1 & 0 \\ \frac{\tilde{\gamma}'}{2\gamma}(1 - e^{i\omega\Delta t}) & 1 \end{pmatrix}. \tag{2.31}$$

In the limit that $\Delta t = t - t_i$ is small, this matrix reduces to

$$R_{\mathrm{rf}} \approx \begin{pmatrix} 1 & 0 \\ -\frac{i\omega\tilde{\gamma}'}{2cp_i}\Delta z & 1 \end{pmatrix}. \tag{2.32}$$

From equation Eq. (2.10), it is clear that this is nothing but a thin lens approximation to the focusing delivered by the RF magnetic field. The complete matrix for the step Δz is found by including the effects of the field edges. The effect of adding the time dependence to the edge matrices is minimal; the rising edge matrix remains the same. For the falling edge matrix, the change in the RF phase is included in the electric field: $\tilde{\gamma}'_f = \tilde{\gamma}' e^{i\omega\Delta t}$. Adding the edge matrices to Eq. (2.30) gives

$$\begin{aligned} \Delta M^{\mathrm{rf}}_{x,x'} &= R_E^{-1}\left(\gamma_f, \tilde{\gamma}' e^{i\omega\Delta t}\right) R_{\mathrm{rf}}(\gamma_f, \tilde{\gamma}', e^{i\omega\Delta t}) M^{\mathrm{dc}}_{i\to f} R_E(\gamma_i, \tilde{\gamma}') \\ &= \begin{pmatrix} 1 & 0 \\ \frac{\mathrm{Re}[\tilde{\gamma}' e^{i\omega(t_i+\Delta t)}]}{2\gamma_f\beta_f^2} & 1 \end{pmatrix} \begin{pmatrix} 1 & 0 \\ \frac{1}{2\gamma_f}\mathrm{Re}[\tilde{\gamma}'(1 - e^{i\omega\Delta t})e^{i\omega t_i}] & 1 \end{pmatrix} \times \ldots \\ &\qquad \ldots \times \begin{pmatrix} C & \frac{p_i}{b}S \\ -\frac{b}{p_f}S & \frac{p_i}{p_f}C \end{pmatrix} \begin{pmatrix} 1 & 0 \\ -\frac{\mathrm{Re}[\tilde{\gamma}' e^{i\omega t_i}]}{2\gamma_i\beta_i^2} & 1 \end{pmatrix}. \end{aligned} \tag{2.33}$$

This is the main result of this work. As a reminder, $\tilde{\gamma}' = e\tilde{\mathcal{E}}_z(z_i)/mc^2$, where $\tilde{\mathcal{E}}_z$ is the complex electric field map. Additionally, the expressions for γ, p, and Δt can be found in Eqs. (2.13-2.15), respectively. For clarity we leave the result in the above factorized matrix

form. This allows several limiting cases to be easily evaluated. First, in the limit that both the RF and solenoid fields vanish, $b, \tilde{\gamma}' \to 0$, and Eq. (2.33) reduces to a drift matrix. For vanishing RF fields, $\tilde{\gamma}' \to 0$, and Eq. (2.33) reduces to a hard edge solenoid matrix. In the limit that $\omega \to 0$, $R_{\rm rf}$ reduces to $I_{2\times 2}$, and the total RF matrix reduces to the previous electrostatic result in Eq. (2.21). In addition to having the correct limiting behavior, the RF transfer matrix also has the correct determinant: $\det[\Delta M^{\rm rf}_{x,x'}] = \det[\Delta M^{\rm dc}_{x,x'}] = p_i/p_f$. This follows directly from the fact that $\det[R_{\rm rf}] = 1$. The factorized matrix form in Eq. (2.33) also clearly demonstrates the dynamics of a step through overlapped RF and solenoid fields: focusing from the change in the accelerating field, rotation from the solenoid, compression from acceleration, as well as focusing from the RF magnetic field. Additionally, because the analytic form depends only on the reference trajectory defined by $t(z)$, $\gamma(z)$, $\Delta\theta_L(z)$, and the field maps at the same position, these quantities do not have to be computed using Eqs. (2.13-2.15). This allows one to construct a transfer matrix directly from the reference and field data output from any simulation code if desired.

2.5 Testing the Transfer Matrix

To test the validity of our approach, the energy gain and transfer matrix are calculated through three different field set-ups and compared to direct integration of the equations of motion using a fourth order Runge-Kutta algorithm. The three field set-ups used are a DC gun with overlapping solenoid, a SRF cavity, and a RF gun with a solenoid-immersed cathode. To check that the transfer matrix correctly describes the transverse dynamics in each case, all four transfer matrix elements are compared with Runge-Kutta integration. To do so, the two principle trajectories through each field set-up are computed. These

trajectories are defined by the initial phase space coordinates $\mathbf{u} = (1\,\text{mm},\ 0)^T$, and $\mathbf{u} = (0,\ 1\,\text{mrad})^T$.

Table 2.1: Simulation Parameters

Parameter	DC gun & Solenoid	RF Cavity	RF gun & Solenoid
Voltage	500 kV	3 MV	1 MV
Phase	0 deg	0 deg (on-crest)	0 deg (on-crest)
Max B_{sol}	0.04 T	N/A	0.04 T
KE($z = z_i$)	1eV	1 MeV	1 eV
Step Size Type	fixed	fixed	adaptable
Step Size	1 mm	2 mm	0.1 mm (avg.)

For the first simulation, we use the field maps for the the high voltage DC gun and first emittance compensation solenoid of the Cornell ERL injector prototype. Fig. 2.1(a) shows the field maps corresponding to gun voltage and solenoid field strength given in Table 2.1. Fig 2.1(b) shows how the energy gain computed from the constant field solution in Eq. (2.13) compares with the energy gain computed using Runge-Kutta integration. The step size used for the constant field solution is 1 mm. The agreement between the two methods demonstrates that the constant field solution works very well for the longitudinal variables, even for low initial kinetic energies. Fig. 2.2 shows the results of tracking the principle trajectories using both the RF transfer matrix with $\omega = 0$, and Runge-Kutta integration. As with longitudinal variables, the agreement between both methods of tracking is excellent. In addition to these results, the expression for the electrostatic transfer matrix has been experimentally verified in [46]. Next, the two principle trajectories are computed through the field map of the 1.3 GHz Cornell ERL injector SRF cavity. Fig. 2.3(a) shows the on-axis electric field map of the SRF cavity model with a 3 MV cavity voltage. The corresponding energy gain through the cavity, computed using the constant field solution and Runge-Kutta integration, are shown in Fig. 2.3(b). The results of

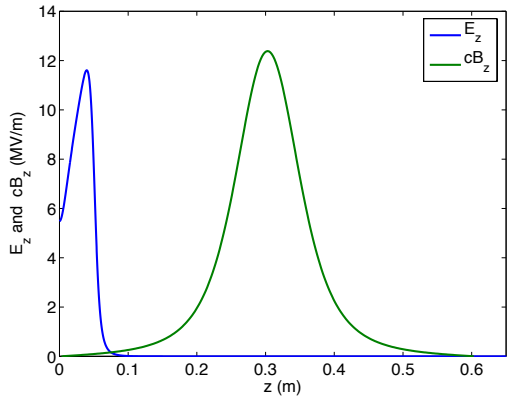

(a) Field maps for the DC gun and solenoid.

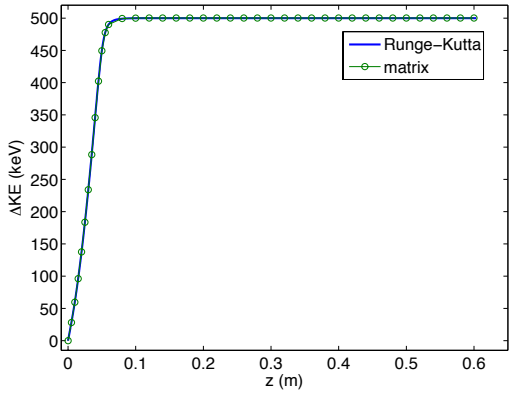

(b) Energy gain through the DC gun.

Figure 2.1: The fields and energy gain for a 500 kV gun voltage, 0.04 T maximum solenoid field setting, and 1 eV initial kinetic energy.

tracking the two principle trajectories through the cavity, with a fixed step size of 2 mm, are shown in Fig 2.4. As in the electrostatic case, the agreement is very good. Finally, the principle trajectories are computed through the RF gun set-up. To simulate an RF gun, the last 1.5 cells of the injector cavity field map are used. The solenoid field is positioned so that the maximum value of the solenoid field occurs at the cathode. In order to make sure that the RF phase is constant over each step, a simple adaptive step size algorithm is included. This algorithm adjusts the step size so that the change in RF phase over the step is less than a user-defined tolerance. Fig. 2.5(a) shows field maps for the RF gun set-up. The corresponding energy gain through the gun is shown in Fig. 2.5(b). The accelerating field is scaled so that the RF cavity voltage is 1 MV and the phase is set for maximum acceleration. The tracking results for the two principle trajectories are shown in Fig. 2.6. From the figure, it is clear that that the transfer matrix works well in the low energy case. The average step size for the simulation was roughly $\Delta z = 0.1$ mm.

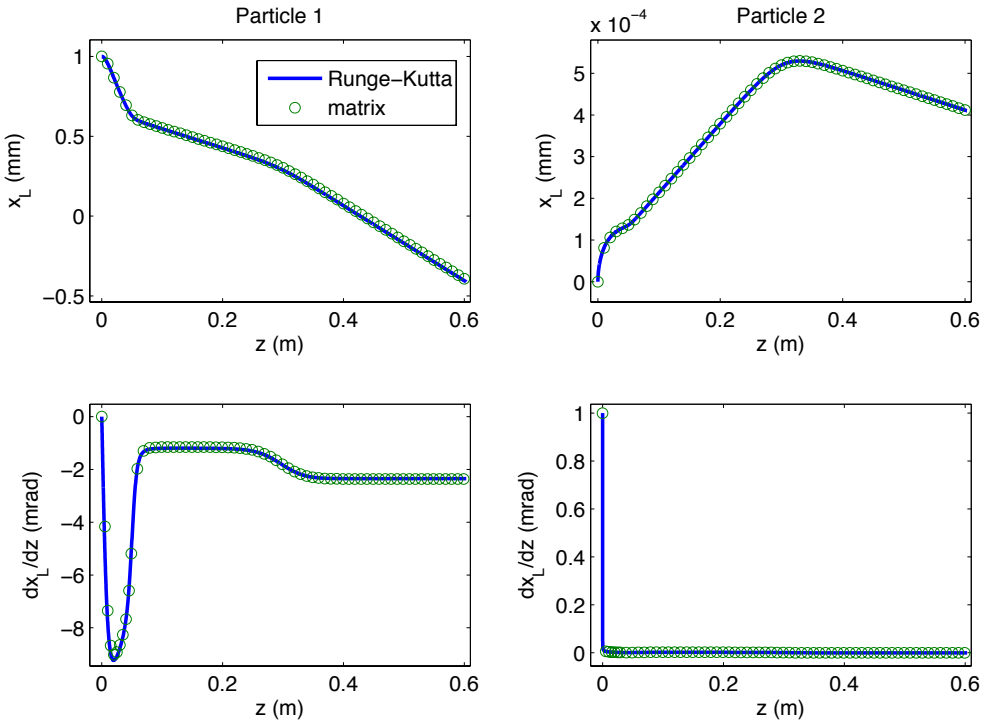

Figure 2.2: Comparison of Runge-Kutta integration (blue) and the tracking using the transfer matrix (green) through the DC gun and solenoid fields.

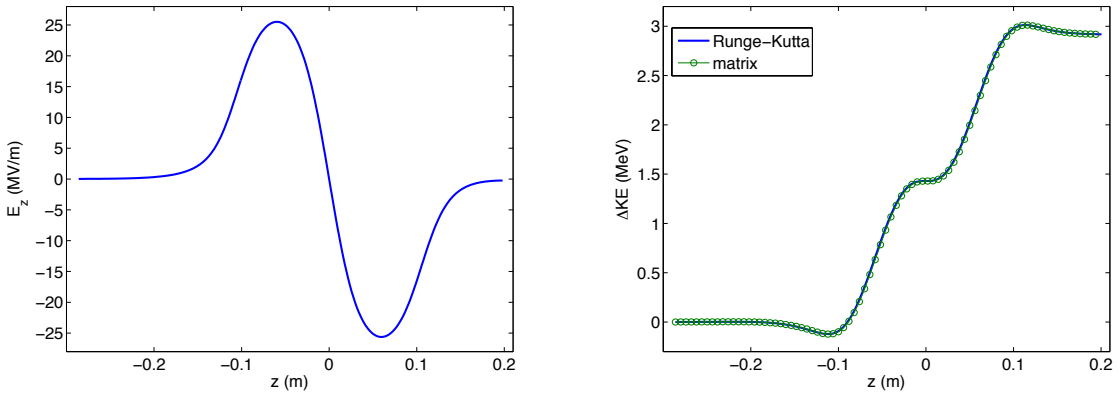

(a) SRF cavity field map.

(b) Energy gain through the SRF cavity.

Figure 2.3: The field map for the SRF injector cavity and the corresponding energy gain. The cavity voltage is 3 MV, the initial kinetic energy is 1 MeV, and the phase is on-crest.

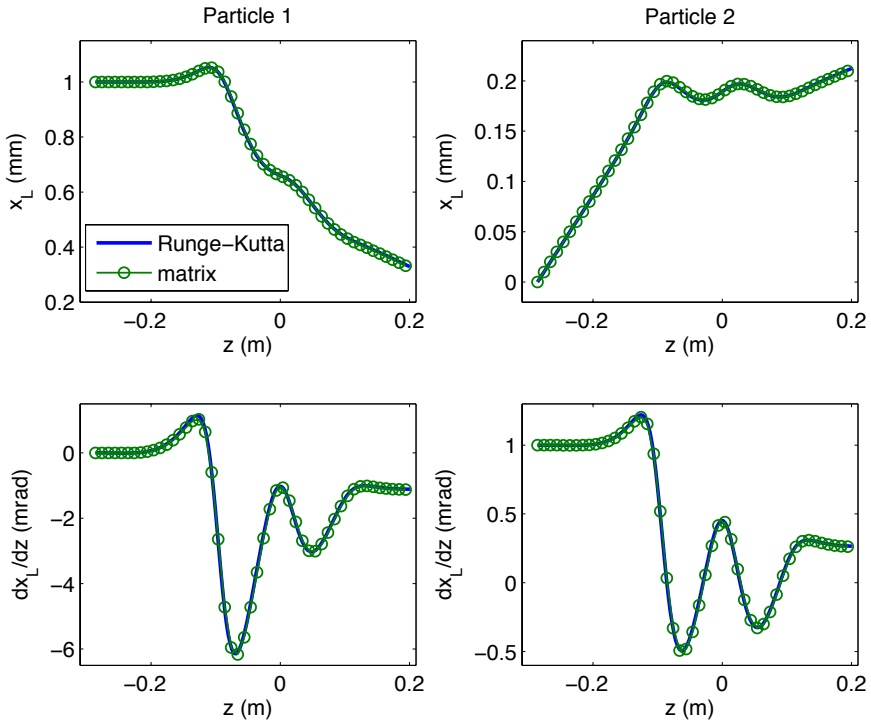

Figure 2.4: Comparison of direct integration (blue) and tracking using the transfer matrix (green) of the two principle trajectories.

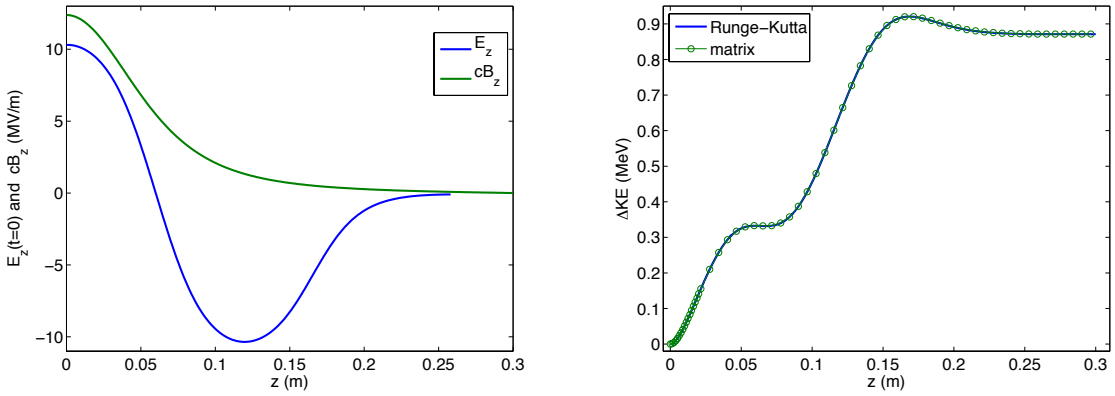

(a) RF gun field maps.

(b) Energy gain through the RF gun.

Figure 2.5: The fields and energy gain. The cavity field is scaled and rotated so that the cavity voltage is 1 MV, and the phase is set to the on-crest value for a 1 MeV electron.

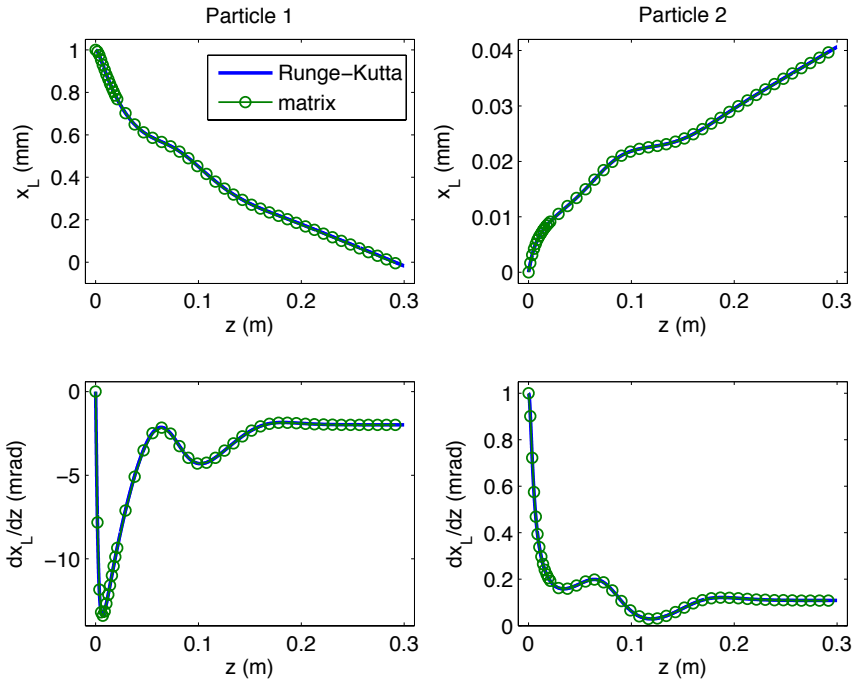

Figure 2.6: Comparison of direct integration (blue) and tracking using the transfer matrix (green) of the two principle trajectories.

2.6 Conclusion

We have derived and tested a new method for calculating the 4×4 transfer matrix through superimposed RF and solenoid fields. The algorithm computes the transfer matrix directly from the field data without computing eigenfunction expansions or numerical derivatives. Comparison with numerical integration demonstrates that this new method works for low energy beams starting from a solenoid immersed cathode. Additionally, because the algorithm relies on analytic solutions to the equations of motion, it is simple to implement and guarantees the correct value for the determinant of the transfer matrix. One limitation to this approach is the assumption (inherent in the derivation) that the fields display cylindrical symmetry. For many applications this is a reasonable assumption; however, previous work shows that asymmetric focusing from input power couplers may be noticeable

when heavy beam loading is present [54]. In addition, when tracking ultra-relativistic particles, the algorithm takes steps typically on the order of a few millimeters, and therefore may not be the best choice for computational speed. In this case, one may still choose to use the Rosenzweig-Serafini matrix. Nonetheless, the matrix algorithm given here strikes an appropriate balance between accuracy, speed, and simplicity not previously achieved.

CHAPTER 3

Study of the Asymmetric Focusing from Twin Input Power Couplers Using Realistic RF Cavity Field Maps

Originally published as: C. Gulliford, I. Bazarov, S. Belomestnykh, and V. Shemelin, Phys. Rev. ST Accel. Beams **14**, 032002 (2011) [54].

3.1 Abstract

Advanced simulation codes now exist that can self-consistently solve Maxwell's equations for the combined system of an RF cavity and a beam bunch. While these simulations are important for a complete understanding of the beam dynamics in RF cavities, they require significant time and computing power. These techniques are therefore not readily included in real time simulations useful to the beam physicist during beam operations. Thus, there exists a need for a simplified algorithm which simulates realistic cavity fields significantly faster than self-consistent codes, while still incorporating enough of the necessary physics to ensure accurate beam dynamics computation. To this end, we establish a procedure for producing realistic field maps using lossless cavity eigenmode field solvers. This algorithm incorporates all relevant cavity design and operating parameters, including beam loading from a non-relativistic beam. The algorithm is then used to investigate the asymmetric

quadrupole-like focusing produced by the input couplers of the Cornell ERL injector cavity for a variety of beam and operating parameters.

3.2 Introduction

The effects on the beam dynamics due to the placement of both the input power couplers and HOM couplers of superconducting radio-frequency cavities in linear accelerators have been studied extensively. The majority of this work focuses on the transverse momentum imparted to the beam due to a single input power coupler or a pair of up- and downstream HOM couplers [57–59]. Many mitigation techniques for eliminating this 'coupler kick' have been proposed and studied for a variety of cavity geometries, including the TESLA-style ILC cavity, the CEBAF cavities [60], as well as the injector and main linac cavities for the proposed Cornel ERL [61–64]. One of these techniques is to design the cavity with twin symmetric power couplers. This approach has been used in the design for the cavities in the current Cornell ERL injector prototype, a high-brightness photoelectron source. While this effectively eliminates the dipole coupler kick, it still produces off-axis quadrupole-like focusing near the couplers. Developing a way to correctly model this effect in heavily beam-loaded super-conducting cavities like those found in high current electron accelerators–particularly high brightness photoinjectors and RF guns (where the beam may not be considered ultra-relativistic)–is the goal of this investigation.

The layout of our work is as follows. First, drawing on previous studies [57–64], a detailed description of how to compute realistic field maps for RF cavities using lossless eigenmode solvers is given. This method incorporates all relevant cavity design and operating parameters. These include the cavity voltage, phase, detuning angle, input coupling, and beam loading. While the basis of this method has been previously developed,

to our knowledge there is no single comprehensive account of this procedure in the literature. Additionally, for non-relativistic beams, this treatment yields implicit expressions for the cavity fields. In order to extend the algorithm to account for low beam energies, approximations for computing the effective cavity voltage and R/Q of the cavity are given and tested. The use of these approximations results in explicit expressions for the cavity fields. Next, the definition of the coupler kick is also extended to the non-relativistic regime by explicitly writing the effect in terms of the transfer matrix elements through the cavity field map. We provide one description of how to compute these matrices using orbit differentiation [53], and also give a simple method for expanding the cavity fields in the paraxial approximation assuming symmetry about the x-z and y-z planes (quadrupole-like symmetry). Having extended the algorithm for computing the cavity fields as well as the effect of the input couplers, we perform several checks on both and discuss the relevant numerical issues involved. Finally, we apply this methodology to the model of the Cornell ERL injector cavities and quantify the quadrupole focusing effect due to the use of twin symmetric input couplers. The effect is documented for scans of both the initial beam energy and the average beam current, and for both orientations of the cavity (the couplers at the cavity entrance vs. exit).

3.3 Field Generation Algorithm

The computation of RF cavity fields can be greatly simplified by making one assumption: the effects of beam loading do not alter the form of the fields in the cavity. In this limit, the beam induces a voltage in the cavity in one of its fundamental modes. This assumption is valid if the amount of energy lost to each bunch, ΔU_b, is very small compared to the energy

stored in the cavity:

$$\frac{\Delta U_b}{U} \ll 1. \tag{3.1}$$

In this limit, it is possible to create realistic fields from lossless eigenmode solvers. The procedure for synthesizing these field maps involves reconstructing the forward and reflected traveling waves in the input power coupler(s). The proper normalization and phase of these waves are related to the cavity design and operating conditions. By correctly including the operating conditions, the combined traveling waves in the input coupler represent the forward power from the RF generator and the reflected power back out of the cavity. Proper construction of these waves ensures the correct form for the fields in the cavity.

3.3.1 The Cornell ERL Injector Cavity Model

Before moving directly to the procedure for constructing realistic cavity fields, it is instructive to give a brief description of the Cornell ERL injector cavity as it is used as a working example in following sections. The Cornell ERL photoinjector cryomodule houses five superconducting two-cell niobium RF cavities. The relevant design and nominal operating parameters for the injector cavities are listed in Table 3.1 [61]. Each cavity is powered by two symmetric coaxial input couplers. The couplers are designed to deliver 50 kW of forward power when operating with 100 mA average current at a cavity voltage of 1 MV. The amount of coupling to the cavity can be adjusted depending on the desired operating conditions (low or high current running). This is accomplished by changing the insertion depth of the coupler antennae. To model the cavities we use the eigenmode field solver in CST Microwave Studio (MWS) [65]. Fig. 3.1 shows the 3D injector cavity model used in MWS. The model assumes the cavity is made of perfectly conducting material surrounded by vacuum. The ends of the beam line are terminated by using an electric short

Cornell ERL Injector Cavity Parameters	
Frequency	1300 MHz
Number of Cells	2 Elliptical
Number of Couplers	2 Coaxial
Cavity Gap Voltage	1-3 MV
Quality Factor Q_0	$\geq 5 \times 10^9$
External Q-Factor Q_{ext}	$4.6 \times 10^4 - 4.1 \times 10^5$
Coupler Radii r_i, r_o	11, 30 mm

Table 3.1: List of Cavity Parameters.

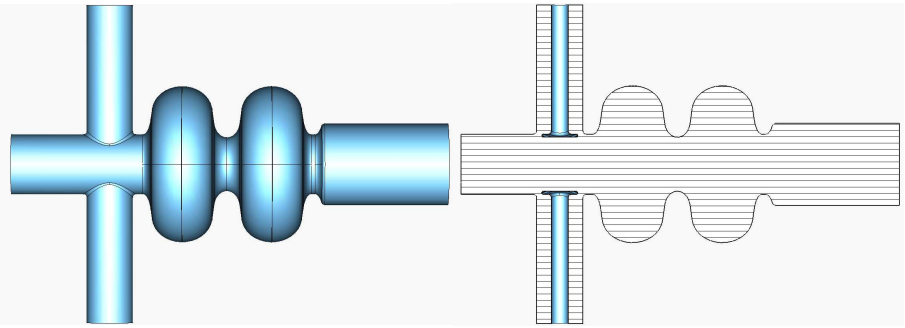

Figure 3.1: Microwave Studio model of ERL Injector Cavity showing the cavity exterior (left), and the cavity cross-section and the inner conductors of the coaxial power couplers (right).

($E_{\|} = 0$). The choice of boundary condition for the end of the coaxial power couplers is discussed later. The coordinate system in the model is defined so that z-axis in the model coincides with the beam axis (the positive direction is to the right in Fig. 3.1) and the y-axis is parallel to the center axis of the twin symmetric input couplers.

3.3.2 Creating Traveling Waves in the Coaxial Coupler Line

3.3.2.1 Analytic Expressions

To create the correct fields in the power coupler, it is necessary to derive analytic formulas for the fields in this region. Far from the end of the coupler and cavity, the fields take the form of two superimposed TEM traveling waves. We assume no other types of modes are excited in the coupler. In this region the fields are given by:

$$\begin{aligned}\tilde{\mathbf{E}}_{\pm} &= \frac{A_{\pm}}{r}\exp\left[i(\pm k(y-y_0)+\phi_{\pm})\right]\hat{\mathbf{r}},\\ \tilde{\mathbf{B}}_{\pm} &= \mp\frac{A_{\pm}}{cr}\exp\left[i(\pm k(y-y_0)+\phi_{\pm})\right]\hat{\theta},\end{aligned}$$

Here the '+' and '−' subscripts label the forward and reflected waves in the top coupler (positive y-axis). The tilde denotes that these quantities are phasors with an associated time dependence of $e^{i\omega t}$. The location of the origin along the y-axis, y_0, is arbitrary. The forward and reflected power determine the amplitudes of each wave:

$$A_{\pm} = \sqrt{\frac{\mu_0 c P_{\pm}}{\pi \ln(r_o/r_i)}}, \qquad A_{-} = \sqrt{\frac{P_{-}}{P_{+}}}A_{+}, \tag{3.2}$$

The terms r_o and r_i are the outer and inner radius of the coaxial coupler. The reflection coefficient Γ is defined by the complex ratio of *amplitudes* of $\tilde{\mathbf{E}}_{-}$ and $\tilde{\mathbf{E}}_{+}$:

$$\Gamma = \left(\frac{\tilde{E}_{-}}{\tilde{E}_{+}}\right)_{y=y_0} = \frac{A_{-}}{A_{+}}e^{i\Delta\phi} = |\Gamma|e^{i\phi_{\Gamma}}. \tag{3.3}$$

From this it follows that $A_{-} = |\Gamma|A_{+}$, and $\Delta\phi = \phi_{-} - \phi_{+} = \phi_{\Gamma}$.

3.3.2.2 Circuit Model and Relation to Operating Parameters

In addition to being related to the operating parameters, the forward and reflected power also satisfy the general formula for the conservation of energy in the cavity-beam system:

$$P_{+} = P_{-} + P_c + P_b. \tag{3.4}$$

In this equation P_c is the power lost in the cavity walls, and P_b is the average power delivered to the beam. Satisfying the balance of powers in this equation provides one useful check for the algorithm described below. From these quantities, the well known quality factors for the cavity are defined [66, 67]:

$$Q_0 = \frac{\omega U}{P_c}, \qquad Q_{\text{ext}} = \frac{\omega U}{P_{\text{ext}}}, \qquad Q_b = \frac{\omega U}{P_b}. \tag{3.5}$$

The term P_{ext} is the power emitted back out of the input couplers when the cavity is operated with both the beam and power generator turned off: $P_b = P_+ = 0$. In this limit, $P_{\text{ext}} = P_-$. The quality factor associated with the power lost to the beam can be written as $Q_b = 2\pi(\Delta U_b/U)^{-1}$. The criterium in Eq. (3.1) is equivalent to having a large value of Q_b. Lastly, the measure of the coupling strength, denoted by β, is defined as $\beta = P_{\text{ext}}/P_c = Q_0/Q_{\text{ext}}$.

The above quantities can now be related to the operating conditions using transmission line theory and the equivalent circuit model for a beam loaded cavity first given by Wilson [66]. The notation used here more closely follows that of Wangler [68] in a similar treatment. Fig. 3.2 shows the equivalent parallel circuit for the cavity and waveguide including beam loading. The waveguide is modeled as a matched external load coupled to the cavity circuit via a transformer. In the figure, the waveguide impedance Z_{WG} has already been transformed into the cavity circuit. The effective voltage drop across the cavity is defined in terms of the energy gain of an electron traveling through the cavity on axis:

$$V_c(\phi_0) = \frac{[\Delta W(\phi_0)/e]}{\cos\phi_0}.$$

The phase ϕ_0 is defined so that $\phi_0 = 0$ is the phase that maximizes the energy gain $\Delta W(\phi_0 = 0) = \max(\Delta W)$. In addition, the sign of ϕ_0 is chosen so that it also represents the difference in phase of the cavity voltage to the beam current. The cavity gap voltage is defined by taking the ultra-relativistic limit of the effective cavity voltage: $V_c \to V_0$ as

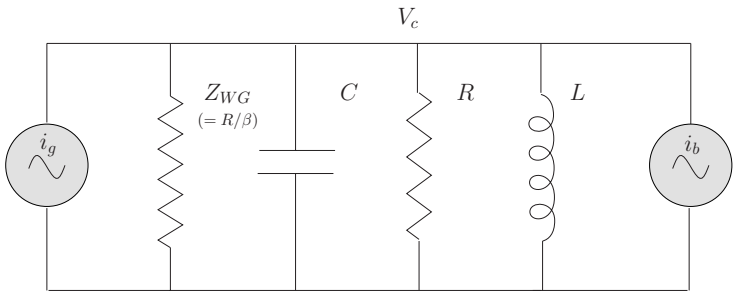

Figure 3.2: Equivalent circuit model for a beam-loaded cavity as seen from the internal cavity circuit. The cavity is excited by the generator current i_g and the beam current i_b.

$v \to c$. The maximum effective voltage is used, along with the power lost in the cavity walls, P_c, to define the effective shunt impedance:

$$R = \frac{V_c^2}{P_c}(\phi_0 = 0).$$

It is often useful to work with the ratio of the effective shunt impedance and the intrinsic quality factor:

$$(R/Q) \equiv \frac{R}{Q_0} = \frac{V_c^2}{\omega U}(\phi_0 = 0). \tag{3.6}$$

Finally, the loaded detuning parameter is defined as

$$\tan\psi' = 2Q_L\left(\frac{\Delta\omega}{\omega}\right). \tag{3.7}$$

Here $\Delta\omega$ is the difference between generator frequency and the resonant frequency of the cavity, and $Q_L = Q_0/(1+\beta)$ is the loaded quality factor. For strongly coupled cavities $Q_L \approx Q_{\text{ext}}$.

In terms of these definitions, the complex impedance of the cavity is given by [66]

$$Z_c = \frac{(R/Q)Q_0}{1 + i\tan\psi'}. \tag{3.8}$$

This impedance is in parallel to the beam impedance $Z_b = (V_c/I_b)e^{i\phi_0}$. This amounts to having a total admittance of

$$Y = \frac{1}{Z_b} + \frac{1}{Z_c} = \frac{I_b}{V_c}e^{-i\phi_0} + \frac{1 + i\tan\psi'}{(R/Q)Q_0}. \tag{3.9}$$

From the circuit, the waveguide impedance is given by $Z_{\mathrm{WG}} = R/\beta$. The general formula for the reflection coefficient can be written as

$$\Gamma = \frac{V_-}{V_+} = \frac{1 - Y \cdot Z_{\mathrm{WG}}}{1 + Y \cdot Z_{\mathrm{WG}}}. \tag{3.10}$$

Substituting in the total admittance and the waveguide impedance yields

$$\Gamma = -\frac{\frac{1-\beta}{1+\beta} + \frac{I_b}{V_c}(R/Q)Q_L e^{-i\phi_0} + i\tan\psi'}{1 + \frac{I_b}{V_c}(R/Q)Q_L e^{-i\phi_0} + i\tan\psi'}.$$

Using the fact that $V_c = V_+ + V_-$ and the above expression for Γ, the forward and reflected powers can be solved for:

$$\begin{aligned} P_+ &= P_c \frac{(\beta+1)^2}{4\beta} \times \\ &\quad ... \quad \times \left[\left(1 + \frac{I_b}{V_c} \left(\frac{R}{Q} \right) Q_L \cos\phi_0 \right)^2 + \left(\tan\psi' - \frac{I_b}{V_c} \left(\frac{R}{Q} \right) Q_L \sin\phi_0 \right)^2 \right], \\ P_- &= P_c \frac{(\beta+1)^2}{4\beta} \times ... \\ &\quad ... \quad \times \left[\left(\frac{1-\beta}{1+\beta} + \frac{I_b}{V_c} \left(\frac{R}{Q} \right) Q_L \cos\phi_0 \right)^2 + \left(\tan\psi' - \frac{I_b}{V_c} \left(\frac{R}{Q} \right) Q_L \sin\phi_0 \right)^2 \right]. \end{aligned} \tag{3.11}$$

The formula for P_+ is equivalent to the formula for the generator power P_g in [66]. With these expressions for the forward and reflected power, it is easy to directly verify the relationships in Eqs. (3.2) and (3.3), as well as the conservation of energy requirement in Eq. (3.4).

It should be noted that any parameters defined in terms of the energy gain of a single particle through the cavity, ΔW, are in fact functions of the fields we are trying to construct. This is due to the fact that the energy gain is not in general given simply by $V_0 \cos\phi_0$ in the non-relativistic limit. This issue will be further addressed after the equations for the realistic field maps have been (implicitly) defined.

3.3.2.3 Connection to Eigenmode Solutions

Having connected the analytic expressions for the fields in the coaxial coupler line to the cavity design and operating parameters, we now connect the analytic expressions to the solutions from the eigenmode solver. To re-create traveling waves in the coaxial coupler line of the forms given in Eq. (3.2), two sets of electric and magnetic fields are generated [57–59, 61–64]. Each set is created by terminating the input coupler line in the computer model with either an electric or magnetic wall boundary condition. The field solutions in the coaxial line near the boundary will then be of the form

$$\text{Electric Wall} \qquad \begin{cases} \mathbf{E}^e = \frac{A^e}{r}\sin(k(y-y_{\text{BC}}))\hat{\mathbf{r}} \\ \mathbf{B}^e = i\cdot\frac{A^e}{cr}\cos(k(y-y_{\text{BC}}))\hat{\theta} \end{cases} \tag{3.12}$$

$$\text{Magnetic Wall} \qquad \begin{cases} \mathbf{E}^m = \frac{A^m}{r}\cos(k(y-y_{\text{BC}}))\hat{\mathbf{r}} \\ \mathbf{B}^m = -i\cdot\frac{A^m}{cr}\sin(k(y-y_{\text{BC}}))\hat{\theta} \end{cases} \tag{3.13}$$

where y_{BC} is the position of the coupler boundary condition. It is now easy to identify these terms with the real and imaginary components of the fields given by the eigenmode solver:

$$\text{Electric Wall} \qquad \begin{cases} \text{Re}[\mathbf{E}^e_{\text{MWS}}] = \frac{A^e}{r}\sin(k(y-y_{\text{BC}}))\hat{\mathbf{r}} \\ \mu_0\text{Im}[\mathbf{H}^e_{\text{MWS}}] = \frac{A^e}{cr}\cos(k(y-y_{\text{BC}}))\hat{\theta} \end{cases} \tag{3.14}$$

$$\text{Magnetic Wall} \qquad \begin{cases} \text{Re}[\mathbf{E}^m_{\text{MWS}}] = \frac{A^m}{r}\cos(k(y-y_{\text{BC}}))\hat{\mathbf{r}} \\ \mu_0\text{Im}[\mathbf{H}^m_{\text{MWS}}] = -\frac{A^m}{cr}\sin(k(y-y_{\text{BC}}))\hat{\theta} \end{cases} \tag{3.15}$$

From here it is evident that adding $\pm\lambda/4$ to the line length of the electric wall solutions transforms the fields into those produced using the magnetic wall condition (up to an overall sign). With these relations, the MWS field maps are added together in the following manner to yield the plane waves given in Eq. (3.2). First, the amplitudes are solved for in terms of the field maps:

$$\begin{aligned} A^e &= a\cdot\mu_0 c\cdot\text{Im}[\mathbf{H}^e_{\text{MWS}}](r=a, y=y_{\text{BC}})\cdot\hat{\theta}, \\ A^m &= a\cdot\text{Re}[\mathbf{E}^m_{\text{MWS}}](r=a, y=y_{\text{BC}})\cdot\hat{\mathbf{r}}, \end{aligned}$$

for some arbitrary radius a such that $r_i \leq a \leq r_o$. It turns out that the field generation algorithm is quite sensitive to the calculation of these amplitudes, as will be discussed later. The fields are normalized and combined to form traveling waves using:

$$\begin{aligned} \tilde{\mathbf{E}}_{\pm} &= A_{\pm}\left[\frac{\mathrm{Re}[\mathbf{E}^m_{\mathrm{MWS}}]}{A^m} \pm i\frac{\mathrm{Re}[\mathbf{E}^e_{\mathrm{MWS}}]}{A^e}\right] e^{i\phi_{\pm}}, \\ \tilde{\mathbf{B}}_{\pm} &= i\mu_0 A_{\pm}\left[\frac{\mathrm{Im}[\mathbf{H}^m_{\mathrm{MWS}}]}{A^m} \pm i\frac{\mathrm{Im}[\mathbf{H}^e_{\mathrm{MWS}}]}{A^e}\right] e^{i\phi_{\pm}}, \\ \phi_{\pm} &= \pm k(y_{\mathrm{BC}} - y_{\mathrm{ref}}) + \phi_{\Gamma}(1 \mp 1)/2. \end{aligned} \tag{3.16}$$

Note the inclusion of the factor $\exp[\pm ik(y_{\mathrm{BC}} - y_{\mathrm{ref}})]$. This is used to shift the origin of the traveling waves. The position y_{ref} is the location of the *reference plane*, the point where the maximum in the amplitude of the electric fields occurs when the reflection coefficient Γ is positive and real. The next section gives the procedure for how to compute the position of reference plane. It is easy to show using the analytic expressions for the field patterns in Eq. (3.15) that this combination of fields yields the correct set of traveling waves in the coaxial line. Plugging in the expressions for the forward and reflected waves, the total fields can be written as

$$\begin{aligned} \tilde{\mathbf{E}} &= A\left[\left(1 + \Gamma e^{-i(2k\Delta y)}\right)\frac{\mathrm{Re}[\mathbf{E}^m_{\mathrm{MWS}}]}{A^m} + i\left(1 - \Gamma e^{-i(2k\Delta y)}\right)\frac{\mathrm{Re}[\mathbf{E}^e_{\mathrm{MWS}}]}{A^e}\right], \\ \tilde{\mathbf{B}} &= i\mu_0 A\left[\left(1 + \Gamma e^{-i(2k\Delta y)}\right)\frac{\mathrm{Im}[\mathbf{H}^m_{\mathrm{MWS}}]}{A^m} + i\left(1 - \Gamma e^{-i(2k\Delta y)}\right)\frac{\mathrm{Im}[\mathbf{H}^e_{\mathrm{MWS}}]}{A^e}\right]. \end{aligned} \tag{3.17}$$

In these equations $\Delta y = y_{\mathrm{BC}} - y_{\mathrm{ref}}$. These equations imply several important facts, all of which depend on the value of the reflection coefficient Γ. First, if the cavity is run under perfectly matched conditions, $\Gamma = 0$, and the resulting fields are independent of the position of the reference plane. Physically this is due to the fact that when Γ vanishes, only an incoming traveling wave exists in the input coupler, for which there is no reference plane. The above equations also show that there are only two critical values of Γ for which the equations for the fields reduce to one of the two eigenmode solutions (either the

electric or magnetic solutions). These occur when the reflection coefficient is given by $\Gamma_{\pm} = \pm \exp[i(2k\Delta y)]$. In general these two critical values are complex and therefore not of interest when simulating cavities under normal operation (where reactive beam loading is compensated using cavity detuning and the reflection coefficient is real). Thus, in general, to correctly model the fields near the couplers, one must use both eigenmode solutions.

3.3.2.4 Finding the Reference Plane

The position of the reference plane is related to the phase of the reflection coefficient Γ. This is seen by computing the amplitude function of the total electric field in the coaxial line:

$$|\tilde{E}_+ + \tilde{E}_-| = \frac{1}{r}\sqrt{A_+^2 + A_-^2 + 2A_+A_- \cos(2k(y - y_{\text{ref}}) - \phi_\Gamma)}.$$

The reference plane is defined as the position of the maximum of this function when the reflection coefficient Γ is real and positive . If Γ has some non-zero phase then the position of the maximum in this function shifts by $\Delta y = (\phi_\Gamma/4\pi)\lambda$.

It is possible to compute y_{ref} using several solutions from lossless eigenmode solvers [67]. When simulating the cavity fields using the eigenmode solver, there is no effect from a beam: $I_b = 0$. In this limit, the reflection coefficient for a real cavity becomes

$$\Gamma = \frac{\frac{\beta-1}{\beta+1} - i\tan\psi'}{1 + i\tan\psi'}.$$

For strongly coupled cavities ($\beta \gg 1$), this quantity is positive and close to unity when the cavity is run on resonance. If the cavity is tuned very far from resonance then $\psi' \to \pm\pi/2$. In this limit $\Gamma \to -1$, and $\phi_\Gamma \to \pm\pi$. This implies that the amplitude maximum will shift by $\Delta y = \pm\lambda/4$. Thus, if one can simulate the lossless cavity model being detuned, then the position of the reference plane can be computed. This is accomplished by terminating the coupler with an electric (or magnetic) wall at several different positions. In general MWS

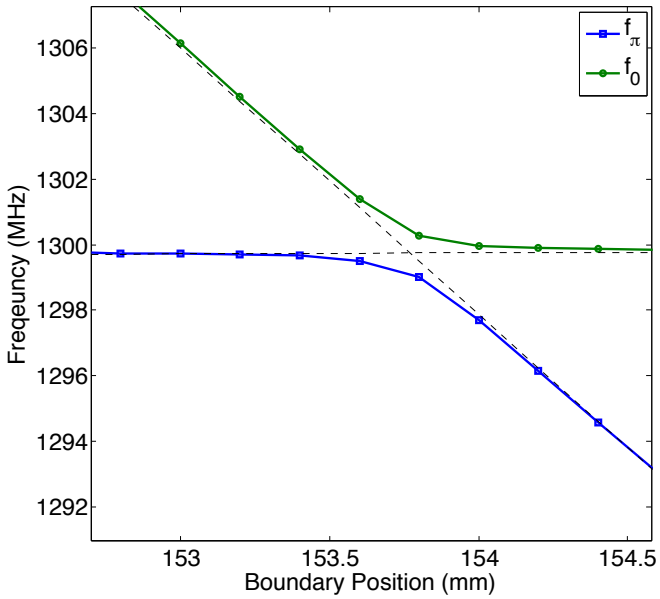

Figure 3.3: Frequency of 0- and π-modes in coupler region vs. coupler length.

will produce two modes of interest with frequencies near the actual operating frequency ω of the real RF system. The coupler and the cavity regions in the model form a pair of coupled oscillators. Consequently there will be two modes of oscillation: one with the fields in both regions oscillating in phase together, and another where the fields in the two regions oscillate out of phase. We call these modes the zero and π modes of the cavity-coupler system. These labels do not correspond to the zero and π resonant modes of the cavity itself, the latter of which is considered the normal mode of operation for the two cell cavities in the Cornell ERL injector. Fig. 3.3 shows the results of varying the position of the electric wall condition and plotting the zero and π modes of the global cavity-coupler system. In the region where the two mode frequencies nearly intersect, the ratio of the magnitudes of the fields in the coupler region to those in the cavity region is a maximum. In terms of a real cavity, this corresponds to tuning the cavity far from resonance. This means that the reference plane is then $\pm\lambda/4$ from this position:

$$y_{\text{ref}} = y_{\text{BC}}^{\text{off}} \pm \frac{\lambda}{4}. \tag{3.18}$$

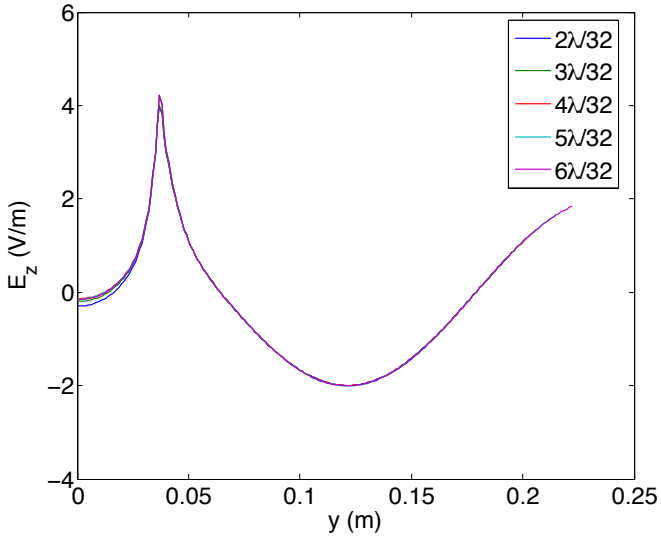

Figure 3.4: Radial electric field generated by combining the forward and reflected waves for $\Gamma = 1$ and $t = 0$ sec. The fields are evaluated so that the radial field in the coupler is given by E_z (V/m) in that region.

Here $y_{\rm BC}^{\rm off}$ is the position of the boundary condition when the cavity is simulated off resonance. Setting the boundary condition to this value makes it difficult to identify the cavity π mode, which has a resonant frequency of 1300 MHz in the case of the Cornell injector cavity. This can be seen in Fig. 3.3. The two modes plotted here have frequencies which deviate from 1300 MHz when $y = y_{\rm BC}^{\rm off}$. If the boundary position is moved by $\pm\lambda/4$ then, according to Eq. (3.15), when one switches from the electric to magnetic wall, this will be equivalent to running the simulation with an electric wall at $y_{\rm BC}^{\rm off}$. One must then place the boundary in between $y_{\rm BC}^{\rm off}$ and $y_{\rm BC}^{\rm off} + \lambda/4$. As long as the boundary condition is not near these points and the coupler length is large enough to accommodate the TEM mode, the position of the boundary condition does not matter. Fig. 3.4 shows this invariance of the radial electric fields in the coaxial input coupler at $t = 0$. The fields shown are the combined forward and reflected traveling waves for the case where $\Gamma = 1$. In this plot, the boundary condition has been varied from $y_{\rm BC}^{\rm off} + (2/32)\lambda$ to $y_{\rm BC}^{\rm off} + (6/32)\lambda$. In the figure, the two fields with the shortest coupler length show the greatest difference from the

rest of the fields created, as is expected. This does not invalidate the assumption that the position of the boundary condition is invariant within $y_{\rm BC}^{\rm off}$ and $y_{\rm BC}^{\rm off} + \lambda/4$, but provides the first indication that it may be necessary to add on length to the coupler in units of $\lambda/2$ to ensure the proper standing wave pattern is achieved near the boundary condition. This fact is addressed later on when we give a systematic check of the field generation algorithm.

3.3.2.5 Computing R/Q, V_c, and $Q_{\rm ext}$

Having now defined all of the relevant cavity design and operation parameters, and given the procedure for constructing the cavity fields assuming all of these parameters are known, it is now time to address the problem discussed in previous sections that many of the operating conditions depend on the computed energy gain through the fields. This means that the fields have actually been implicitly defined in terms of themselves. In this section we resolve this issue. In addition we also briefly describe a convenient method for computing the external quality factor [63].

Because the injector cavities are designed to have large $Q_{\rm ext}$ values, the fields in the cavity cells are standing waves. This fact can be used to compute approximate values for the cavity voltage V_c and R/Q. The quantities are defined as

$$V_c = \frac{[\Delta W(\phi_0)/e]}{\cos\phi_0}, \qquad R/Q = \frac{[\max(\Delta W/e)]^2}{\omega U}.$$

The total energy stored in the fields can be approximated by noting:

$$U = \frac{\epsilon_0}{2}\int\limits_{\rm cavity} |\mathbf{E}|^2 dV \cong \frac{\epsilon_0}{2}\int\limits_{\rm cells} |\mathbf{E}|^2 dV,$$

assuming the cavity is not run far off resonance. This approximation is valid because the

majority of the energy stored in the fields is found in the cavity cells. This means that this quantity can be approximated by

$$U \cong \frac{\epsilon_0}{2} \int\limits_{\text{cells}} |\alpha_m \mathbf{E}^m|^2 dV = \alpha_m^2 \text{ [Joule]},$$

since the standing wave field pattern in the cavity cells should be roughly the same as the standing wave from the MWS eigenmode solver. Here α_m is a scaling factor used to normalize the fields to the correct voltage. This can be easily computed by tracking particles through the on-axis field $E_z^m(r=0)$. The above equation makes use of the fact that MWS normalizes the energy in its solutions to 1 J. The solution $\mathbf{E}^e$ could also be used. Similarly,

$$\Delta W(\phi_i) \cong e \int \text{Re}[\alpha_m E_z^m(r=0) e^{i(\omega t(z)+\phi_i)}] dz,$$

with the initial phase offset $\phi_i \in [0, 2\pi]$. We define ϕ_{off} so that $\Delta W(\phi_{\text{off}}) = \max(\Delta W(\phi_i))$. The effective cavity voltage and R/Q are then explicitly given by

$$\begin{aligned} V_c &\cong \frac{1}{\cos\phi_0} \int \text{Re}[\alpha_m E_z^m(r=0) e^{i(\omega t+\phi_{\text{off}}+\phi_0)}] dz, \\ R/Q &\cong \frac{1}{\omega \alpha_m^2} \left[\int \text{Re}[\alpha_m E_z^m(r=0) e^{i(\omega t+\phi_{\text{off}})}] dz \right]^2. \end{aligned}$$

Fig. 3.5 shows the results of computing the on-axis energy gain as a function of initial phase of the cavity through both the realistic fields, computed with the algorithm described above (light blue line), and the fields generated by Microwave Studio using a magnetic wall boundary condition (dark blue line). For this scan, the initial kinetic energy of the beam $\text{KE}_i = 1$ MeV, the speed-of-light cavity voltage $V_0 = 1$ MV, the average beam current $I_b = 100$ mA, the phase offset of the cavity $\phi_0 = 30$ deg (red line), $Q_0 = 10^{10}$, $Q_{\text{ext}} = 4 \times 10^4$, and the reactive beam loading is compensated. The green line shows the computed value of $\Delta W = eV_c \cos\phi_0$, which intersects the graph at the correct point. It is apparent that the energy gain of both sets of fields is the same, verifying the assumptions made for the computation of ΔW and R/Q.

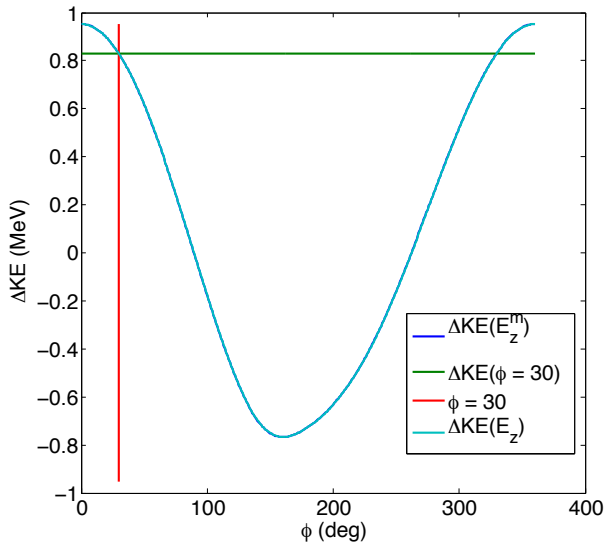

Figure 3.5: Checking the energy gain approximation scheme.

The last quantity to compute before constructing the realistic cavity fields is Q_{ext}. Several methods for computing Q_{ext} from two eigenmode solutions have been previously proposed [67, 69]. We use a method prescribed by Buckley and Hoffstaetter [63]. This method generally assumes one input coupler, but is easily modified for the case of several identical input couplers. Assume the cavity has been excited by a generator to some voltage and the generator then switched off. After some time, only waves traveling out of the cavity will be present, and the fields $\mathbf{E}_-$ and $\mathbf{B}_-$ can be used to compute Q_{ext}. First, the stored energy in the cavity is computed:

$$U = \frac{\epsilon_0}{2}\int |\mathbf{E}_-|^2 dV = \frac{\epsilon_0}{2}\left(\frac{A_-}{A^e}\right)^2 \int \left(\xi^2|E^m|^2 + |E^e|^2\right) dV,$$

where $\xi = A^e/A^m$. The integrals over the electric fields are known. Microwave Studio normalizes the integrals over each set of fields to one joule. Thus the total energy stored in the cavity is $U = (A_-/A^e)^2(\xi^2+1)$. The power flowing out of the coupler(s) is given by $P_- = \frac{\pi}{\mu_0 c}A_-^2 \ln(r_o/r_i)$. Combining these expressions gives

$$Q_{\text{ext}} = \left[\frac{1}{2}\right]\left(\frac{\xi^2+1}{\xi^2}\right)\left(\frac{k}{\pi\epsilon_0}\right)\frac{1 \;\; \text{Joule}}{(A^m)^2 \ln(r_o/r_i)}.$$

In this equation $k = \omega/c$. The factor of 1/2 in brackets is included for the case of the twin symmetric couplers used in the Cornell injector cavity model. If the normalization of the fields is different (or not known), the factor $\xi^2 + 1$ becomes $\xi^2 U^m + U^e$, which can still be computed directly from the eigenmode fields. The realistic fields can now be computed: first V_c, R/Q, and Q_{ext} are computed using the above expressions. With these quantities and the rest of the operating conditions, the forward and reflected power $P_{\pm}$, and the reflection coefficient Γ are computed. Then, using Eqs. (3.16) and (3.17), the cavity fields are constructed. The new fields can be used to recompute V_c and the process iterated until the field profiles converge to a unique result. In the cases studied in this work, at most two iterations were needed.

3.4 RF Coupler Kicks

3.4.1 Generalizing the Definition of the Coupler Kick

To quantify the effect of the input power couplers on the linear beam dynamics of the cavity model, we generalize the formulas for the normalized momentum change in cavity. This is done by first examining the 'coupler kick', as defined in the literature, and its connection to the momentum change in the cavity. This leads to a natural generalization of the momentum change in terms of the transfer matrix elements through the cavity.

The normalized coupler kick, as defined by Dohlus [58], is to linear order

$$\mathbf{k}(x,y) = \frac{\mathbf{V}(x,y)}{\mathbf{e}_z \cdot \mathbf{V}(0,0)} = \begin{pmatrix} v_{x,0} + v_{x,x}x + v_{x,y}y \\ v_{y,0} + v_{y,x}x + v_{y,y}y \\ 1 + v_{z,x}x + v_{z,y}y \end{pmatrix},$$

where the complex voltage gain $\mathbf{V}(x, y)$ is defined as

$$\mathbf{V}(x, y) = \int (\tilde{\mathbf{E}} + c\mathbf{e}_z \times \tilde{\mathbf{B}}) e^{i(\omega z/c)} dz.$$

Note that this definition assumes an ultra-relativistic and therefore rigid beam. The coefficients $v_{x,0}$ and $v_{y,0}$ quantify any voltage change (normalized to the on-axis voltage gain) due to dipole-like fields. In general any structure that breaks the cylindrical symmetry of the cavity may contribute to these terms. The remaining coefficients quantify both the focusing due to the cavity and the focusing due to the input and HOM couplers. The normalized voltage change can be directly used to compute the momentum kick imparted to a particle traversing the cavity:

$$\Delta\mathbf{p} = \left(\frac{e}{c}\right) \mathrm{Re}\left[\mathbf{k}(x, y) e^{i(\omega s/c)}\right] V_{\mathrm{acc}}.$$

Here s denotes the position of a particle with respect to the center of the beam.

The formula for the momentum change can now be generalized by allowing the transverse and longitudinal offset of particles moving through the cavity to vary. In this case, the momentum change can still be related to the initial particle offset from the reference particle, using the transfer matrix elements:

$$\Delta\mathbf{p}(s) = \begin{pmatrix} \Delta p_{x,0} + M_{p_x,x} x_0 + M_{p_x,y} y_0 \\ \Delta p_{y,0} + M_{p_y,x} x_0 + M_{p_y,y} y_0 \\ \Delta p_{z,0} + M_{p_z,x} x_0 + M_{p_z,y} y_0 \end{pmatrix}.$$

Dividing by the change of the reference energy defines the normalized momentum change through the cavity

$$\mathbf{k}(s) = \frac{1}{\Delta p_{z,0}} \begin{pmatrix} \Delta p_{x,0} + M_{p_x,x} x_0 + M_{p_x,y} y_0 \\ \Delta p_{y,0} + M_{p_y,x} x_0 + M_{p_y,y} y_0 \\ \Delta p_{z,0} + M_{p_z,x} x_0 + M_{p_z,y} y_0 \end{pmatrix}. \tag{3.19}$$

3.4.1.1 Transfer Matrix Computation

For non-relativistic beam energies the transfer matrix elements cannot be computed using analytic or semi-analytic methods like those of Rosenzweig and Serafini [47]. A simple method, used by TEAPOT [53], to compute the transfer matrix is to numerically differentiate particle trajectories. We use an eighth-order implicit symplectic integrator [70] to track four separate particles. The transverse phase space variables used are

$$\mathbf{u} = (x, \quad \gamma\beta_x, \quad y, \quad \gamma\beta_y)\,. \tag{3.20}$$

Each of the four particle trajectories is offset slightly in one of the four phase space variables. Labeling the j-th particle trajectory as $\mathbf{u}^{(j)}$ and its initial offset in the j-th phase space variable as $\Delta u^{(j)}$, the transverse transfer matrix elements can then be computed using

$$M_{ij} = \frac{\partial u_i(z_f)}{\partial u_j(z_i)} \cong \frac{u_i^{(j)}(z_f)}{\Delta u^{(j)}}.$$

The initial offsets $\Delta u^{(j)}$ must be made small enough so as to avoid non-linear effects, as well as to ensure the symplecticity of the resulting transfer matrix. Using the symplectic integrator with initial particle position and momentum offsets of 10^{-15} meters, and 10^{-15} $[\gamma\beta]$ respectively, yields transfer matrices which preserve the symplecticity of the system to near machine accuracy: $\det(M) - 1 \sim 10^{-15}$. Scanning the initial offsets between 10^{-4} and 10^{-14} shows little variation in the matrix elements themselves.

3.4.1.2 Off-Axis Expansion of the Fields

Because we are only concerned with linear dynamics, we can use an off-axis expansion of the fields (as opposed to a full 3D interpolation) to speed up the particle tracking. In general the fields can be expanded around the beam axis in the form

$$f(x, y, z) = \sum_{n,m=0}^{\infty} f^{(n,m)}(z) x^n y^m, \qquad f^{(n,m)}(z) = \frac{1}{m! \cdot n!} \left.\frac{\partial^{n+m} f}{\partial x^n \partial y^m}\right|_{r=0}.$$

The use of twin couplers in the cavity model imposes mirror symmetry in the x-z and y-z planes. These symmetries imply

$$\begin{aligned} E_x &= \begin{cases} E_x(-x,y,z) = -E_x(x,y,z) \\ E_x(x,-y,z) = \quad E_x(x,y,z) \end{cases}, \\ E_y &= \begin{cases} E_y(-x,y,z) = \quad E_y(x,y,z) \\ E_y(x,-y,z) = -E_y(x,y,z) \end{cases}, \\ E_z &= \begin{cases} E_z(-x,y,z) = E_z(x,y,z) \\ E_z(x,-y,z) = E_z(x,y,z) \end{cases}. \end{aligned} \tag{3.21}$$

These conditions imply

$$\begin{aligned} \mathbf{E} &= \sum_{n,m=0}^{\infty} x^{2n} y^{2m} \left[\left(E_x^{(2n+1,2m)} x \right) \hat{\mathbf{x}} + \left(E_y^{(2n,2m+1)} y \right) \hat{\mathbf{y}} + E_z^{(2n,2m)} \hat{\mathbf{z}} \right]. \\ \mathbf{B} &= \sum_{n,m=0}^{\infty} x^{2n} y^{2m} \left[\left(B_x^{(2n,2m+1)} y \right) \hat{\mathbf{x}} + \left(B_y^{(2n+1,2m)} x \right) \hat{\mathbf{y}} + xy B_z^{(2n+1,2m+1)} \hat{\mathbf{z}} \right]. \end{aligned} \tag{3.22}$$

The expression for the magnetic fields follows directly from the form of the electric field and Maxwell's equations. For tracking we keep only the terms in the field expansions to first order (the terms in brackets above with $n = m = 0$):

$$\mathbf{E} \cong x E_x^{(1,0)} \hat{\mathbf{x}} + y E_y^{(0,1)} \hat{\mathbf{y}} + E_z^{(0,0)} \hat{\mathbf{z}}, \qquad \mathbf{B} \cong y B_x^{(0,1)} \hat{\mathbf{x}} + x B_y^{(1,0)} \hat{\mathbf{y}}. \tag{3.23}$$

The first order transverse expansion coefficients in these expressions can be expanded around the axisymmetric first order coefficients. For axisymmetric fields the first order coefficients have the form

$$E_x^{(1,0)} = E_y^{(0,1)} = E_r^{(1)}, \qquad B_x^{(0,1)} = -B_y^{(1,0)} = -B_\theta^{(1)}, \tag{3.24}$$

where the radial and azimuthal components are given by [31]:

$$E_r^{(1)} = -\frac{1}{2} \frac{dE_z}{dz}(r=0), \qquad B_\theta^{(1)} = \frac{i\omega}{2c^2} E_z(r=0).$$

The superscripts in this equation denote the number of derivatives taken with respect to the radial coordinate r. For fields displaying the quadrupole symmetry described in

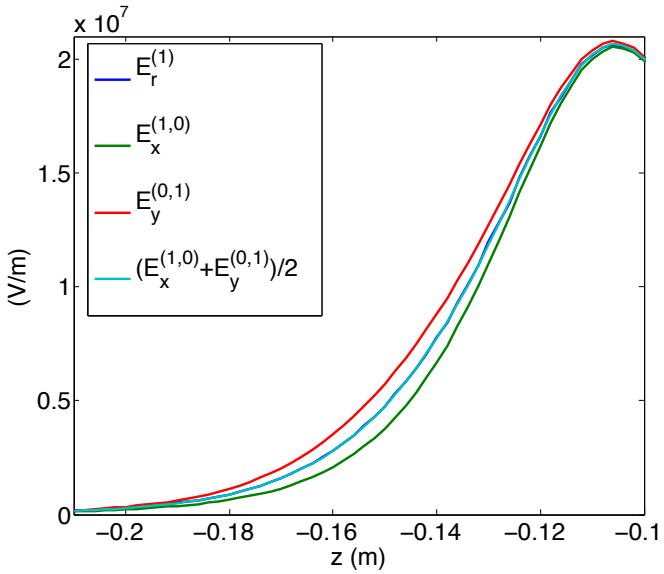

Figure 3.6: The expansion coefficients of E_x and E_y in the coupler region at $t = 0$. Shown here are $E_r^{(1)}$ (dark blue), $E_x^{(1,0)}$ (green), $E_y^{(0,1)}$ (red), and the average the two (light blue).

Eq. (3.21), one can define $\Delta_{\mathcal{E}} = E_x^{(1,0)} - E_r^{(1)}$ and $\Delta_{\mathcal{B}} = B_y^{(1,0)} - B_\theta^{(1)}$. To the appropriate order, Maxwell's equations then impose:

$$\begin{cases} E_x^{(1,0)} = E_r^{(1)} + \Delta_{\mathcal{E}} \\ E_y^{(0,1)} = E_r^{(1)} - \Delta_{\mathcal{E}} \end{cases} \qquad \begin{cases} B_x^{(0,1)} = -B_\theta^{(1)} + \Delta_{\mathcal{B}} \\ B_y^{(1,0)} = \quad B_\theta^{(1)} + \Delta_{\mathcal{B}} \end{cases} \tag{3.25}$$

Fig. 3.6 shows the first order expansion coefficients for the electric field in the coupler region computed from the general 3D field maps. It is clear from the figure that the field expansion coefficients are of the form given in Eq. (3.25). Similar agreement was found for the magnetic field coefficients. The form of the fields in Eq. (3.23) shows directly that the use of symmetric power couplers decouples the x and y phase space variables and eliminates the dipole kick. It is also apparent that the longitudinal momentum gain is independent of the initial particle transverse offset to first order. The equation for the coupler kick in Eq. (3.19) reduces to

$$\mathbf{k}_\perp = \frac{\Delta \mathbf{p}_\perp}{\Delta p_{z,0}} = \frac{1}{\Delta p_{z,0}} \begin{pmatrix} M_{p_x,x}(s) x_0 \\ M_{p_y,y}(s) y_0 \end{pmatrix}. \tag{3.26}$$

We find it useful to look at the gradient of this quantity with respect to the initial transverse offset:

$$\kappa = \frac{1}{\Delta p_{z,0}} \begin{pmatrix} M_{p_x,x}(s) \\ M_{p_y,y}(s) \end{pmatrix}.$$

Plugging the linearized fields into the Lorentz force law gives

$$F_x = (F_r^{(1)} + \Delta_{\mathcal{F}})x, \qquad F_y = (F_r^{(1)} - \Delta_{\mathcal{F}})y,$$

with $F_r^{(1)} = e(E_r^{(1)} - c\beta B_\theta^{(1)})$, the axisymmetric radial focusing force gradient, and $\Delta_{\mathcal{F}} = e(\Delta_{\mathcal{E}} - c\beta\Delta_{\mathcal{B}})$. The transverse gradients of these two forces satisfy

$$F_r^{(1)} = \frac{1}{2}\left(F_x^{(1,0)} + F_y^{(0,1)}\right).$$

From this it is tempting to write the transfer matrix elements in a similar form; however,

$$M_{r,p_r} \neq \frac{1}{2}\left(M_{x,p_x} + M_{y,p_y}\right) \tag{3.27}$$

in general. Only in the ultra-relativistic limit does this relationship hold. In this limit the focusing matrix elements reduce to integrals over the transverse gradients of the force components. The relative difference between κ_x and κ_y can be quantified using

$$\Delta_x = \frac{\kappa_x}{\kappa_y} - 1, \qquad \Delta_y = \frac{\kappa_y}{\kappa_x} - 1, \qquad \bar{\Delta} = \frac{\kappa_x - \kappa_y}{\frac{1}{2}(\kappa_x + \kappa_y)}. \tag{3.28}$$

The last term reduces to $(\kappa_x - \kappa_y)/\kappa_r$ as $v \to c$, giving a measure of the effect of the quadrupole focusing relative to the 'overall' focusing strength.

3.5 Checking the Algorithm

3.5.1 Computation of the Transfer Matrix

As the coupler kick is quantified in terms of the transfer matrix elements, it is important to check both the accuracy of the method to compute each element as well as the symplecticity

of the total transfer matrix. To check the symplecticity of the transfer matrices, we compute the determinant of the matrices as a function of z through the cavity. Using the phase space variables in Eq. (3.20), the determinant should be unity. We also compare the transfer matrix elements to those computed, using a simple 'drift-kick-drift' method which is inherently symplectic. The results of these comparisons are shown in Fig. 3.7. The initial

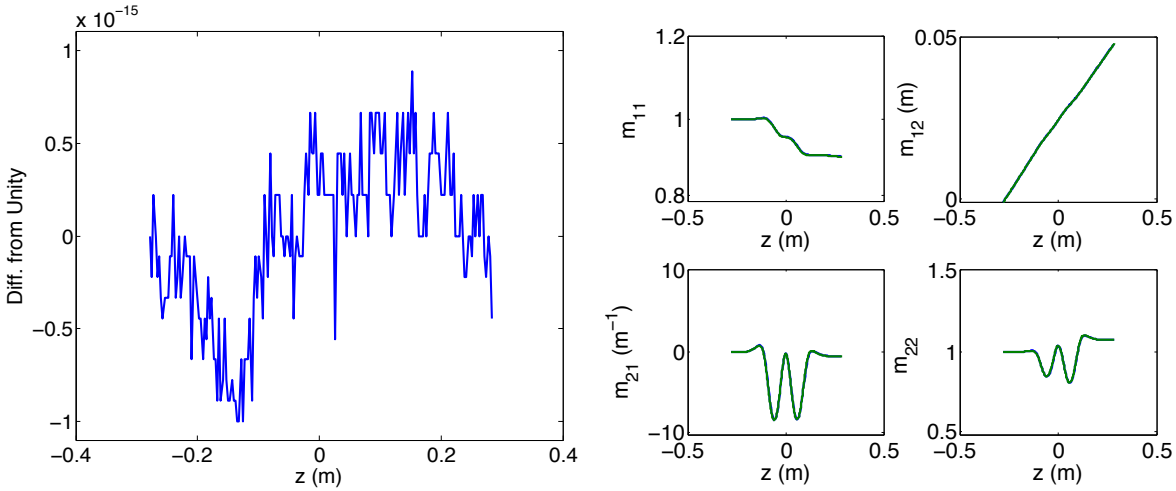

(a) Symplecticity of the transfer matrix. (b) Comparing matrix elements.

Figure 3.7: (a) Comparison of the transfer matrix determinant to unity. (b) Comparison of the symplectic ray differentiation algorithm (blue) to the 'drift-kick-drift' algorithm (green).

offset of the phase space variables used in position and normalized momentum is 10^{-15} m and $10^{-15}\,[\gamma\beta]$ respectively. With these offsets, the determinant of the transfer matrix is equal to unity to machine accuracy, as seen in Fig. 3.7(a). The comparison of the transfer matrix elements with the 'drift-kick-drift' method, Fig. 3.7(b), shows good agreement, indicating that either method could be used. Having two methods of computing the transfer matrix elements is convenient for cross-checking and debugging.

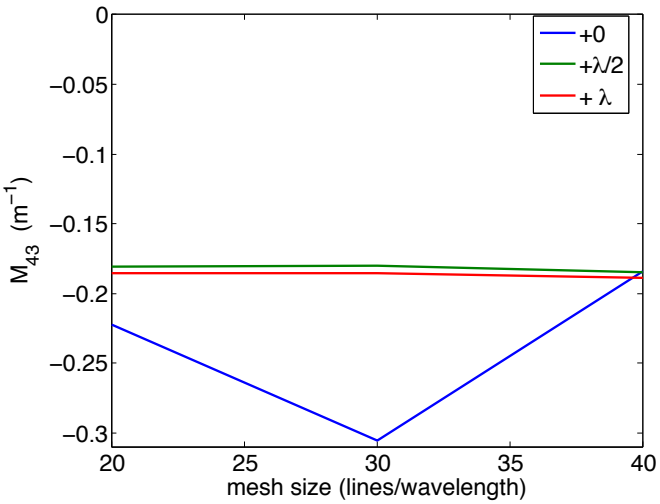

Figure 3.8: M_{y,p_y} focusing element for various coupler lengths and mesh sizes.

3.5.2 Numerical Issues

As mentioned before, it is important to accurately compute the amplitudes of the sinusoidal fields in the coupler region. The computation of these amplitudes depends mainly on two things: the mesh-size used to compute the fields in Microwave Studios, and the length of the coupler section of the cavity model. For meshing the cavity we use Microwave Sudio's automatic meshing algorithm. The parameters used by Microwave Studio to define the mesh are the lines per wavelength, lower mesh limit, and mesh line ratio. For these simulation we set all of these to the same value. To test that we have found the correct mesh size, the transfer matrix elements were computed for meshes of 20, 30, and 40 lines/wavelength. In addition to this, we added $\lambda/2$ and λ to the length of the coupler section. The starting coupler length is $y_{\mathrm{BC}} + \lambda/8$. From equation Eq. (3.18) it is clear that this should not have any effect on the fields in the cavities or the position of the reference plane. As we are interested in computing the transfer matrix elements from the fields, we use the focusing element to quantify the dependence on the mesh size and coupler length. Fig. 3.8 shows the focusing element in the (y, p_y) phase space. The transfer matrix elements

were computed for a 100 mA beam, on-crest beam with initial energy of 350 kV, and a 1 MV cavity voltage. It is clear that adding at least $\lambda/2$ is required to the reduce the dependence of the focusing element on the mesh size. Consequently, the MWS solutions for the original coupler length (labeled +0 in the figure) are not used for any of the studies in this work. For the $+\lambda/2$ and $+\lambda$ cases, the change with mesh size is roughly 2 % when going from 20 to 40 lines/wavelength. The difference between the elements computed for those two cases at each mesh size is roughly 2 to 3 %. This difference is likely being limited by other factors: the residual tolerance of the MWS field solutions, how accurately the cavity fields are phased and normalized, and the resulting numerical integration and differentiation of the particle trajectories through the fields.

3.5.3 Semi-Analytic Check

One check of the algorithm to compute the coupler kick is to take the ultra-relativistic limit of the transfer matrix through the cavity. In this limit $V_c \to V_0$ and $R/Q \to 220\ \Omega$. This allows the computation of Γ without any numerical integration. The fields can then be constructed and compared to the general algorithm given above. Fig. 3.9 shows the (x, p_x) transfer matrix elements computed with the general algorithm for constructing the fields (blue) and the semi-analytic algorithm in the $\beta = 1$ limit (green). The agreement in the matrix elements as well as the fields is very good.

3.6 Results

Having developed and tested a method for producing realistic cavity fields and computing the coupler kick for non-relativistic beams, we turn to investigating the effect for the Cornell

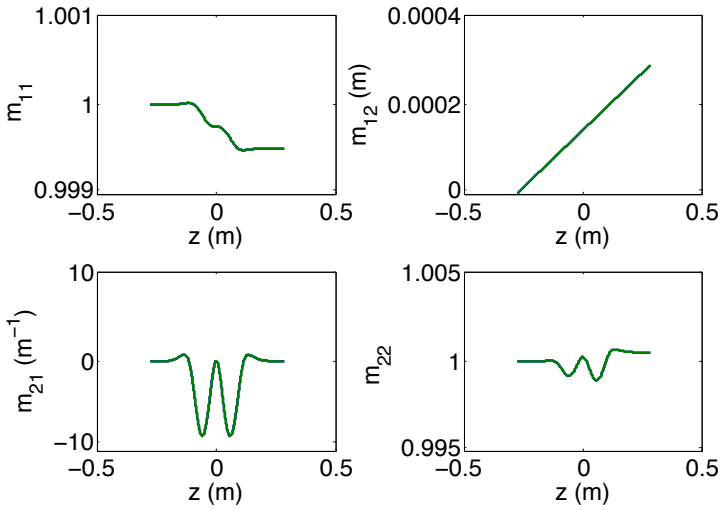

Figure 3.9: Comparison of the general algorithm to the '$\beta = 1$' algorithm.

ERL injector cavity model. As we will show, the results of these simulations demonstrate the need to be able to model the coupler effects for a variety of input conditions. The full set of input parameters required to generate the fields in the Cornell cavity model is given in Table 3.2. In addition to the parameters listed in the table, we also vary the orientation of the cavity (couplers at the entrance or exit of the cavity as seen from the incoming beam). In the Cornell injector the cavities are arranged so that the first cavity is oriented with the coupler at the exit of the cavity. The orientation of the subsequent cavities alternates. We limit the number of parameters varied in our simulations to a subset most often used in normal operation. The amount of coupling to the cavity is set for high current running, as this should increase the effect of the quadrupole focusing due to the couplers. To simulate this geometry, the coupler antennae are inserted into the cavity so that they are nearly flush with the beam pipe, setting Q_{ext} to 4.6×10^4. By making the antennae fully flush in the cavity model, the Q_{ext} calculated from the fields is 4.02×10^4. This corresponds to roughly 1 mm difference in the insertion depth of the coupler and is therefore considered acceptable for simulating the high current set-up of the injector cavities. In general the cavities may be run slightly off-crest in order to minimize growth of

W_i (MeV)	Initial Beam Energy
I_b (mA)	Average Beam Current
ϕ_0 (deg)	Beam Phase
V_c (MV)	Effective Cavity Voltage
V_0 (MV)	Cavity Voltage for $\beta = 1$
Q_0	Intrinsic Quality Factor
Q_{ext}	External Quality Factor
$\tan\psi'$	Loaded Detuning Factor

Table 3.2: List of Simulation Input Parameters.

the projected emittance through the cryomodule. We simplify this by simulating the cavity fields on-crest, as the offsets in the injector phases are usually less than 5 deg. Also, during normal operation, any reactive beam loading is compensated by detuning the cavity. These two restrictions imply $\sin\phi_0 = \tan\psi' = 0$. The remaining parameters left to vary then include the initial kinetic energy of the beam, the average current, and the cavity voltage.

3.6.0.1 Kinetic Energy Scans

It is instructive to scan the initial kinetic energy of the beam first. The current voltage of the ERL DC-gun used in beam operations is 350 keV. For proposed high current runs (100 mA average current), the beam is accelerated from the gun voltage to roughly 5 MeV in the cryomodule. It is also instructive to look at the quadrupole focusing in the ultra-relativistic limit. We perform two scans of the initial kinetic energies: one from the gun voltage to 5 MeV (the injector parameters), and the second from 5 MeV to 1 GeV (ultra-relativistic limit), for both cavity orientations. Fig. 3.10 shows the results of both scans for a 1 MV cavity gap voltage.

For the low energy scan, the first thing to note is that the mean focusing effect is

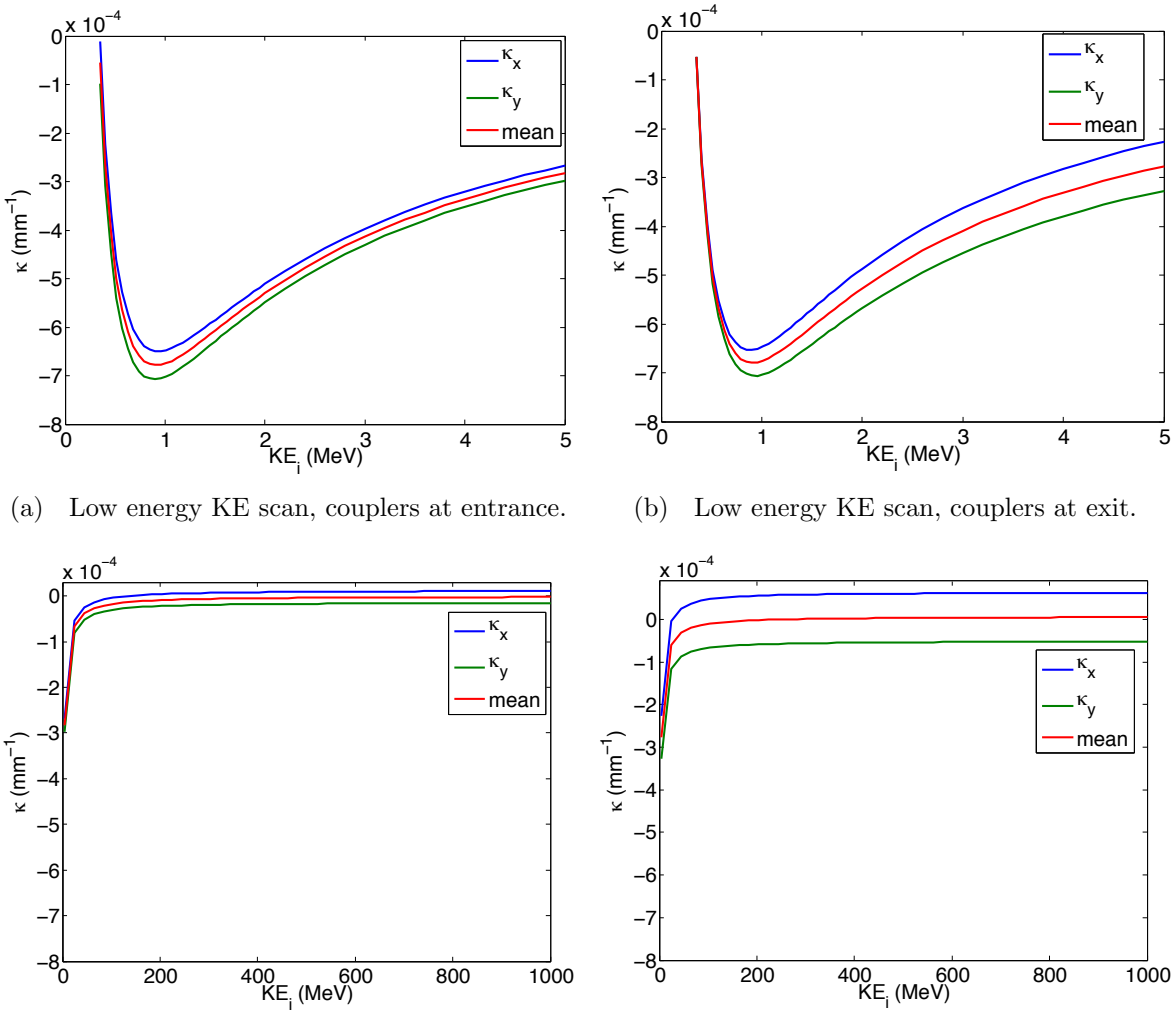

(a) Low energy KE scan, couplers at entrance.

(b) Low energy KE scan, couplers at exit.

(c) High energy KE scan, couplers at entrance.

(d) High energy KE scan, couplers at exit.

Figure 3.10: Scans of the initial beam kinetic energy for both orientations of the cavity model.

approximately the same for both cavity orientations in both energy scans. This implies the majority of the focusing occurs in the cavity cells. In general the quadrupole strength has different behavior for both orientations, as shown in Fig. 3.11. For the case where the coupler is at the entrance to the cavity $\bar{\Delta}$ starts at -161 %and sharply increases to around -11 % as the initial energy increases. When the coupler is at the exit, $\bar{\Delta}$ decreases from -1 to -36 % in a essentially a linear fashion. In both cases the overall focusing and the

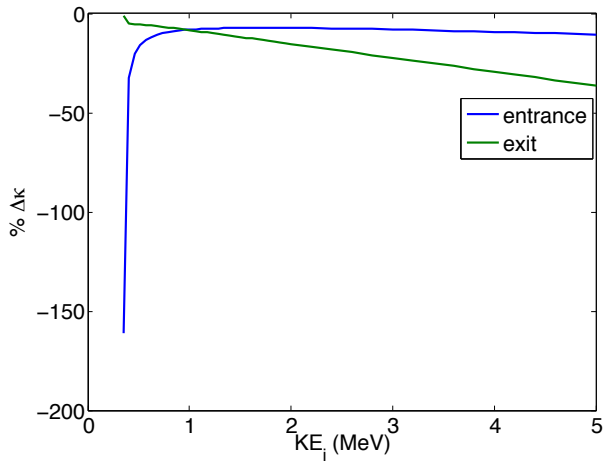

Figure 3.11: $\bar{\Delta}$ as a function of initial beam energy with the coupler at the cavity entrance (blue) and exit (green).

quadrupole effect should become asymptotic as the particles become ultra-relativistic. Fig. 3.10(c) and Fig. 3.10(d) show that the these asymptotic values are quite different from the values at 5 MeV. The asymptotic values are -1138 and 2168 % for the coupler at the entrance/exit respectively. The difference in sign is due to the fact that the mean of κ_x and κ_y is near zero and has a different sign for each cavity orientation. Table 3.3 gives the values of the quadrupole strength relative to the mean focusing for initial kinetic energies near those at the entrance to each of the five cavities in the injector, as well as the asymptotic values. The most significant result here is that the quadrupole effect becomes

Table 3.3: Relative Quadrupole Strength vs. Initial Beam Energy

KE_i [MeV]	0.35	1	2	3	4	5	$(\rightarrow \infty)$
$\bar{\Delta}_{ent}$ [%]	-161	-8	-7	-8	-9	-11	-1138
$\bar{\Delta}_{exi}$ [%]	-1	-8	-15	-22	-29	-36	2168

very pronounced at low initial energy if the input couplers are located at the cavity entrance. The opposite is true when the couplers are at the cavity exit, here the quadrupole effect is larger at higher energy (5 MeV in the injector). Also, in the ultra-relativistic limit, the quadrupole effect becomes increasingly more important as the mean focusing vanishes.

3.6.0.2 Current Scans

The dependence of the linear focusing as a function of beam current is also of interest, as the current will have to be ramped up to 100 mA in proposed experiments in the injector. Fig. 3.12 shows the results of scanning the current from 0 to 100 mA for a 350 keV initial beam energy, and a 1 MV cavity voltage. The Fig. 3.12(a) shows the current scan when the

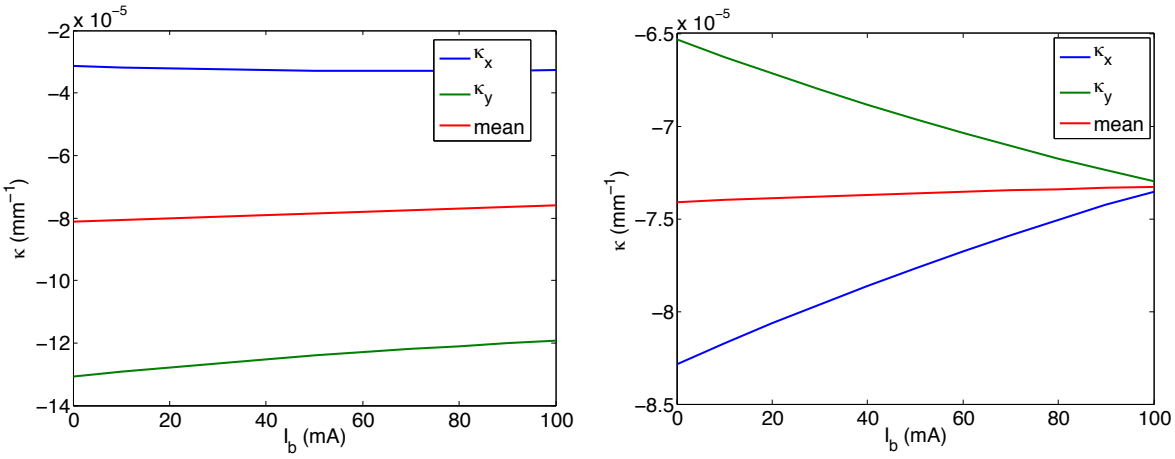

(a) Current scan, couplers at entrance.

(b) Current scan, couplers at exit.

Figure 3.12: Current Scan from 0 to 100 mA for an initial beam energy of 350 keV and the couplers located at the entrance (a), and the couplers located at the exit (b).

couplers are located at the entrance of the cavity. In this case, the quadrupole strength is strong; however, the dependence on the current is small. When the couplers are at the exit of the cavity (Fig. 3.12(b)), the dependence on current is more pronounced, with the quadrupole effect decreasing roughly linearly to near zero at 100 mA. Initially, both of these plots contained a noticeable amount of noise. This noise is caused by 'jitter' in the on-crest phase offset, ϕ_{off}, used to phase the cavity properly. To eliminate this noise, we fit a polynomial to the plot of ϕ_{off} as a function of the beam current and used the polynomial to evaluate $\phi_{\text{off}}(I_b)$ in a second current scan. The dependence of the quadrupole-like focusing on the beam current demonstrates an important point for beam operations, as having

current dependent focusing in the linear optics will effect the centroid motion. Thus, in addition to the effects of space charge, the dependence of the coupler focusing on current will have to be properly accounted for.

3.7 Conclusion

We have developed and tested an algorithm for producing realistic field maps for superconducting RF cavities from eigenmode solver solutions. The algorithm incorporates the effects of beam loading and detuning, and is generalized to include the acceleration of non-relativistic beams. In addition we have generalized the definition of the coupler kick to correctly describe the linear optics for low energy beams. Fields for the RF cavities in the Cornell ERL injector have been created for various initial beam energies and average currents. The RF quadrupole focusing produced by the input couplers has been computed for these fields and shown to be significant for certain beam parameters and cavity orientations. The algorithm given in this work assumes that the single bunch beam loading is small enough that the condition $\Delta U_b/U \ll 1$ holds. While the fields generated in this work generally satisfied this requirement with the single bunch loading on the order of 10^{-5} to 10^{-4}, further study may be warranted to place a stricter bound on $\Delta U_b/U$. In addition, since only the linear beam dynamics have been computed here, the effects of space charge and wakefields must be included for a full model of the cavity beam dynamics at high current. In closing, we note that once one finds the reference plane and correct length of the coupler(s) for a given cavity model, the field generation algorithm described in this work can be included in any tracking code that can handle complex electromagnetic field maps and can compute the on-axis energy gain of particles through each cavity. This allows for its possible inclusion in both offline and online simulation codes.

CHAPTER 4

Demonstration of Low Emittance in the Cornell Energy Recovery Linac Injector Prototype

Originally published as C. Gulliford, A. Bartnik, I. Bazarov, L. Cultrera, J. Dobbins, B. Dunham, F. Gonzalez, S. Karkare, H. Lee, H. Li, Y. Li, X. Liu, J. Maxson, C. Nguyen, K. Smolenski, and Z. Zhao, Phys. Rev. ST Accel. Beams **16**, 073401 (2013) [41].

4.1 Abstract

We present a detailed study of the six-dimensional phase space of the electron beam produced by the Cornell Energy Recovery Linac Photoinjector, a high-brightness, high repetition rate (1.3 GHz) DC photoemission source designed to drive a hard x-ray energy recovery linac (ERL). A complete simulation model of the injector has been constructed, verified by measurement, and optimized. Both the horizontal and vertical 2D transverse phase spaces, as well as the time-resolved (sliced) horizontal phase space, were simulated and directly measured at the end of the injector for 19 pC and 77 pC bunches at roughly 8 MeV. These bunch charges were chosen because they correspond to 25 mA and 100 mA average current if operating at the full 1.3 GHz repetition rate. The resulting 90% normalized transverse emittances for 19 (77) pC/bunch were 0.23 ± 0.02 (0.51 ± 0.04) μm

in the horizontal plane, and 0.14 ± 0.01 (0.29 ± 0.02) μm in the vertical plane, respectively. These emittances were measured with a corresponding bunch length of 2.1 ± 0.1 (3.0 ± 0.2) ps, respectively. In each case the rms momentum spread was determined to be on the order of 10^{-3}. Excellent overall agreement between measurement and simulation has been demonstrated. Using the emittances and bunch length measured at 19 pC/bunch, we estimate the electron beam quality in a 1.3 GHz, 5 GeV hard x-ray ERL to be at least a factor of 20 times better than that of existing storage rings when the rms energy spread of each device is considered. These results represent a milestone for the field of high-brightness, high-current photoinjectors.

4.2 Introduction

The desire for light sources with substantially more coherence and brightness has fueled significant interest in the research and design of ERLs and free electron lasers (FELs). The feasibility of ERL technology has already been demonstrated at several laboratories, most notably Thomas Jefferson National Accelerator Facility (TJNAF) [71], where energy recovery was achieved for 100 MeV beams with an average current of up to 9 mA. However, in order to design and construct a large scale, high energy (GeV) ERL x-ray source, significant advancement of both superconducting RF (SRF) cavity technology, as well as high-brightness, high current sources has been required. Over the last several years, Cornell University has played a lead role in the development of both areas, and has successfully reached several major milestones towards the realization of a practical ERL x-ray facility [19].

To drive this type of machine requires an exceptional electron source producing high-brightness bunches at high repetition rates. Traditionally it has been thought that the

best beam quality was obtained using low duty factor normal conducting RF (NCRF) gun based photoemission sources [37, 38, 72], as these devices are capable of providing high peak cathode fields. These fields are typically in the vicinity of 100 MV/m, though the field at the cathode during emission is often significantly lower since these devices are usually run off-crest [37, 72]. Due to the considerable heat load generated in the cavity walls, the cw operation of NCRF sources requires substantial lowering of the electric gradient, an approach being pursued at several facilities [38, 73]. Work started at TJNAF and later expanded at Cornell University, shows that the combination of a high-voltage DC gun followed immediately by acceleration with superconducting cavities yields beams with single bunch quality rivaling that produced by RF guns, but at much higher (GHz) repetition rates [34, 74]. In addition, DC guns provide an excellent vacuum, allowing for a much wider range of cathode materials to be used than in NCRF guns. While SRF guns show significant promise for producing high-brightness, high-current beams, this technology is currently in the development and testing stage, and the achieved beam parameters so far are relatively modest [42].

Consequently, a photoinjector using a DC gun has been designed, built, and commissioned at Cornell University. One of the main goals of this project was to demonstrate the ability to produce high average current from this source. The Cornell injector has made great strides toward this end, having recently set a new record for high average current from a photoinjector with cathode lifetime suitable for an operating facility [26]. Another major goal is the demonstration of low emittance at the end of the injector's merger section, where the (relatively) low energy beam would be injected into the main ERL linac. The results in this work demonstrate that it is possible to produce and transport beams from a DC source which have emittances at the point of injection approaching the diffraction limit

for hard x-rays, and which have a bunch length and an energy spread within the parameter space required by the specifications of a full hard x-ray ERL.

In general, to achieve the maximum brightness in a photoinjector, it is crucial to control both the transverse and longitudinal space charge forces, as well as the effects of time dependent RF focusing [27, 29–31, 34, 75]. Effective emittance compensation is possible when bunches are created with a charge distribution that has predominantly linear space charge fields [27, 29, 30, 75], and if done correctly, can lead to final emittances approaching the intrinsic emittance of the photocathode. One fundamental limit to this approach occurs when the amount of charge extracted from the cathode nears the virtual cathode instability limit. A rough calculation shows that the lowest achievable emittance then becomes proportional to the square root of the bunch charge q [27]:

$$\epsilon_n \propto \sqrt{q \cdot \frac{\mathrm{MTE}}{E_{\mathrm{cath}}}} \tag{4.1}$$

Here MTE and E_{cath} are the mean transverse energy of the photoelectrons and the accelerating field at the cathode, respectively. Detailed simulations of well optimized DC gun photoinjectors support this square root dependence on the bunch charge and the cathode's MTE [34, 74]. In this paper, we show that the final measured emittance also scales in accordance with Eq. (4.1). This represents a key step in experimentally realizing the maximum brightness limit for photoinjectors.

The outline of this work is structured as follows. First, a general description of the Cornell ERL photoinjector is given. This includes a description of the beamline layout, the relevant accelerating and optical elements, and the diagnostic systems used to take our emittance data. Next, we describe how to model the dynamics in the injector using the space charge simulation code *General Particle Tracer* (GPT) [76], and give a verification of the GPT injector model against linear optics measurements. After this, a description of the

optimization of this model and the process for determining our final optics settings used in the experiment is given. This is followed by the main results of this work. These include direct measurement and simulation of both the projected transverse phase spaces, as well as the time-resolved horizontal phase space at the end of the injector merger section. Additionally, the energy spread distribution was measured using a single dipole magnet in a separate diagnostic beamline section, providing an upper bound on the rms energy spread at the end of the merger.

4.3 The Cornell ERL Injector

Construction of the Cornell injector was completed in the summer of 2007. Initial beam commissioning experiments revealed an issue with charging up of the ferrites in the higher-order mode dampers in the injector cryomodule. After this problem was successfully addressed [77], beam experiments started in earnest in the spring of 2010 and have continued to this date [26, 32, 35, 78–82]. In that time, significant progress towards meeting the target goals of the injector project has been made. Table 4.1 shows these specifications. Of particular interest to this work are the specifications for the normalized transverse emittance and rms bunch length. We demonstrate later in this work that these specifications have been met.

4.3.1 Description and Layout

The layout of the Cornell ERL injector is shown in Fig. 4.1. The Cornell injector features two laser systems. The primary system is a 1.3 GHz laser producing 520 nm, 1 ps rms pulses with an average power of up to 60 W [83], and is used for high current experiments.

Table 4.1: List of injector design specifications and target parameters.

Parameter	Specification
Beam energy	5-15 MeV
Normalized emittance	$\epsilon_n \leq 0.3$ μm
RMS bunch length	$\sigma_t \leq 3$ ps
Bunch Charge	77 (19) pC
Average Current	100 (25) mA

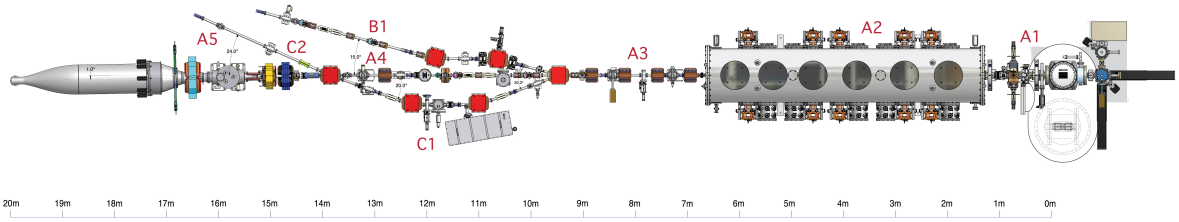

Figure 4.1: Top view of the Cornell ERL injector.

For emittance measurements with nonzero bunch charge, we exclusively use a 50 MHz system, whose individual pulses have comparable pulse energy and duration to the 1.3 GHz laser. This laser system allows us to limit the average electron beam power hitting our interceptive emittance diagnostics. After being generated in one of these two lasers, the final laser pulse train can be chopped using a Pockels cell, and shaped using our temporal shaping system [79]. This system consists of four rotatable birefringent crystals, which are used to divide the primary laser pulse into 16 copies, with tunable relative intensities set by their rotation angles. These crystals are typically tuned to produce a roughly flat intensity profile, with around 8 ps rms duration.

The cathode used for this study was a GaAs wafer grown using Molecular Beam Epitaxy on a p-doped GaAs substrate. The cathode was heat cleaned to 620 °C for 2 hours and then activated to negative electron affinity using Cs and NF_3 via the "yo-yo" process. The doping density was 5×10^{18} cm^{-3}. The top 100 nm was left undoped. The resulting

cathode had a quantum efficiency of 4%, a mean transverse energy of 90 meV, and a sub-picosecond response time at 520 nm.

The high-voltage DC gun used in these measurements is the same one used in previous space charge and emittance studies [26, 32, 35, 78–82]. The gun was operated at 350 kV for all measurements in this work. The beamline section just after the gun, labeled 'A1' in Fig. 4.1, houses two emittance compensation solenoids and a 1.3 GHz normal conducting buncher cavity. These elements were used to compensate the initial emittance blow up near the cathode, and to compress the bunch longitudinally before further acceleration. Immediately after emittance compensation, the bunches were accelerated using the five superconducting niobium cavities in the SRF cryomodule, labeled 'A2' in Fig. 4.1. In addition to increasing the beam energy, and thus partially freezing in the emittance, the SRF cavities were also used to perform further emittance compensation and longitudinal compression via time-dependent transverse and longitudinal focusing. Each cavity features a symmetric twin input coupler design in order to eliminate any time-dependent dipole kick [63, 64] and can be operated with a voltage in the range of 1 to 3 MV. For a more detailed description of the injector cavities see [61].

Just after the cryomodule, the beam was passed through a four-quad telescope, labeled 'A3' in Fig. 4.1. The beam was then directed into one of several diagnostic beamline sections. The section most relevant to this work is the 'B1' merger shown in detail in Fig. 4.2. The injector merger section is comprised of a conventional three-dipole achromat [84–86]. This design was chosen for its simplicity, and due to the limited space available for the injector experiment. The trade off for this approach is that while this merger set-up closes the single particle dispersion, it does not satisfy the second achromat condition $\eta'_{\mathrm{sc}} = 0$ for the space charge dispersion function [84, 85]. Despite this, both our simulations and measurements show that this merger design does in fact preserve low emittance for our

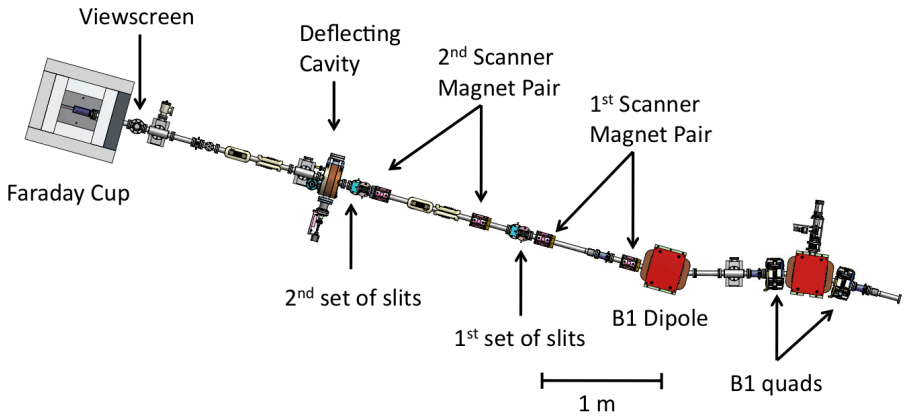

Figure 4.2: Top view of the B1 injector merger section showing the emittance measurement system.

operating parameters. As was anticipated in [85], this was accomplished by finding the correct settings for the four quadrupole magnets in the A3 straight section.

The emittance measurement system (EMS) used for projected and time-resolved phase space measurements is a two-slit system with no moving parts [32]. Fig. 4.2 shows the layout of this diagnostic system. In front of each 20 μm slit is a scanner magnet. Each scanner magnet consists of a pair of air core correcting coils with equal and opposite field polarity and negligible sextupole field component. The resulting effect of the scanner magnet is to translate the beam transversely without imparting any angle to it. In practice the coil pairs in each scanner magnet cancel each other to better than a few percent [32]. For projected phase space measurements, the beamlet coming through both slits was collected using the Faraday cup at the end of the merger section. For time-resolved horizontal phase space measurements, the beamlet was passed through a horizontal deflecting cavity [87] in order to resolve the time axis of the beam on the viewscreen at the end of the merger section [35]. For a more detailed description of the EMS, refer to [32, 35].

4.3.2 The GPT Injector Model

The 3D space charge code GPT was used extensively in this work. To model space charge effects, GPT utilizes a 3D non-equidistant mesh solver [88, 89]. Additionally, GPT allows users to define their own custom optical elements, as well as position and overlay electromagnetic field maps in 3D space. These features provided sufficient versatility to accurately model our machine, where the fields of several elements overlap. All of the beam line elements relevant for the space charge simulations in this work have been modeled using realistic field maps. POISSON-SUPERFISH [90] was used to generate 2D cylindrically symmetric fields specifying $E_r(r, z)$ and $E_z(r, z)$, as well as $B_r(r, z)$ and $B_z(r, z)$, for the high-voltage DC gun and emittance compensation solenoids respectively. The on-axis fields for these elements are shown in Fig. 4.3(a), and 4.3(b).

In order to efficiently and accurately describe the injector dipoles and quadrupoles, we created custom GPT elements which generate 3D fields using an off-axis field expansion of 1D field data. To create the 1D dipole and quadrupole field data, the full 3D fields for each type of element were computed in Opera-3D [91]. From these fields the quantities $B_y(r = 0, z)$ and $\partial B_y(r = 0, z)/\partial x$ were extracted from the dipole and quadrupole fields respectively. Fig. 4.3(c) and 4.3(d) show the 1D field data used for the dipoles and quadrupoles in the injector.

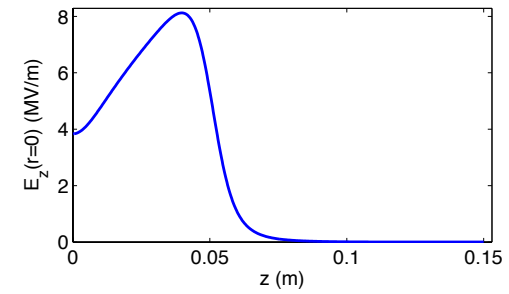

(a) On-axis electric field in the DC gun.

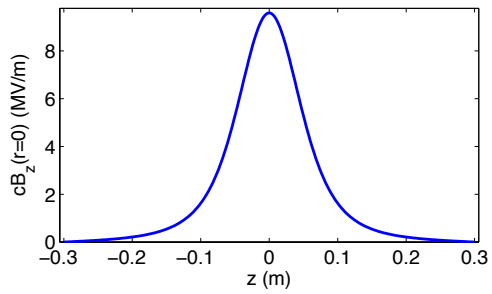

(b) On-axis magnetic field for the A1 solenoids.

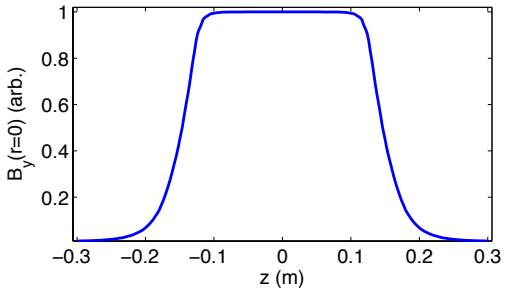

(c) 1D Dipole field map.

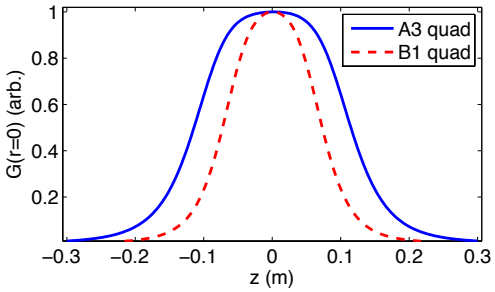

(d) 1D Quadrupole gradient data.

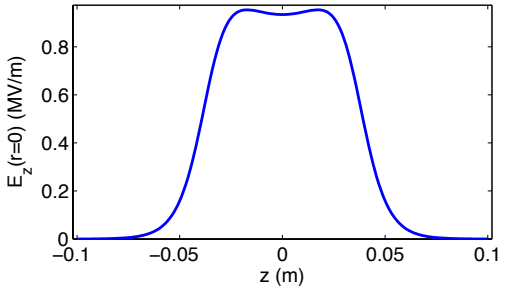

(e) On-axis electric field for the buncher.

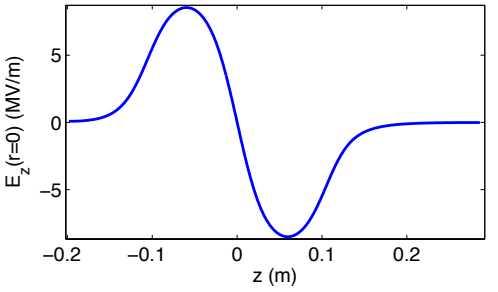

(f) On-axis electric field for the SRF cavity.

Figure 4.3: On-axis electric and magnetic fields for: (a) the high voltage DC gun at 350 kV, (b) emittance compensation solenoid at 3.75 A, (c) the A3 and B1 merger dipoles, (d) the A3 and B1 merger quads, (e) the buncher cavity at 60 kV, (f) the SRF cavity at 1 MV.

Our custom GPT rectangular dipole element uses an off-axis expansion of the fields

given by [92]:

$$\begin{aligned} B_x &\sim \mathcal{O}(4) \\ B_y &= B_0(z) - \frac{y^2}{2}\frac{d^2B_0}{dz^2} + \mathcal{O}(4), \\ B_z &= y\frac{dB_0}{dz} + \mathcal{O}(4), \end{aligned} \tag{4.2}$$

to model the the higher order components of the dipole field. In this expression $B_0 = B_y(r = 0, z)$. This expansion assumes that the particles do not see the fringe fields on the lateral sides of the magnet. This is true for the particle trajectories and magnets in the injector, where the maximum simulated rms beam size through the dipoles was ≤ 3 mm (see Fig. 4.13(b)), and the dipole width was 25 cm. Similarly, the fields for the quadrupoles were computed with an off-axis field expansion [92]:

$$\begin{aligned} B_x &= y\left[G(z) - \frac{1}{2}(3x^2 + y^2)\frac{dG}{dz}\right] + \mathcal{O}(5), \\ B_y &= x\left[G(z) - \frac{1}{2}(3y^2 + x^2)\frac{dG}{dz}\right] + \mathcal{O}(5), \\ B_z &= xyG(z) + \mathcal{O}(4). \end{aligned} \tag{4.3}$$

Here the term $G(z) = \partial B_y/\partial x(r = 0, z)$. To verify Eqs. (4.2) and (4.3), single particle tracking through the fields created by our custom elements was compared to tracking using the full 3D field maps. Excellent agreement was found in both cases. Additionally, the custom elements proved significantly faster because they do not require look-up of 3D field arrays.

All RF cavity fields were generated using the eigenmode 3D field solver in CST Microwave Studio (MWS) [65]. The buncher cavity was modeled using a 2D cylindrically symmetric map specifying: $E_r(r, z)$, $E_z(r, z)$, and $H_\theta(r, z)$. The on-axis field map for the buncher is shown in Fig. 4.3(e).

Previous work demonstrates that asymmetric focusing of the bunch near the input

power couplers of the accelerating cavities is significant and can lead to asymmetric horizontal and vertical emittances [35]. To address this issue, we generated full 3D field maps for the accelerating cavities which incorporate the beam running conditions following our method outlined in [54]. Fig. 4.4 shows the 3D cavity model used in MWS for the accelerating cavities.

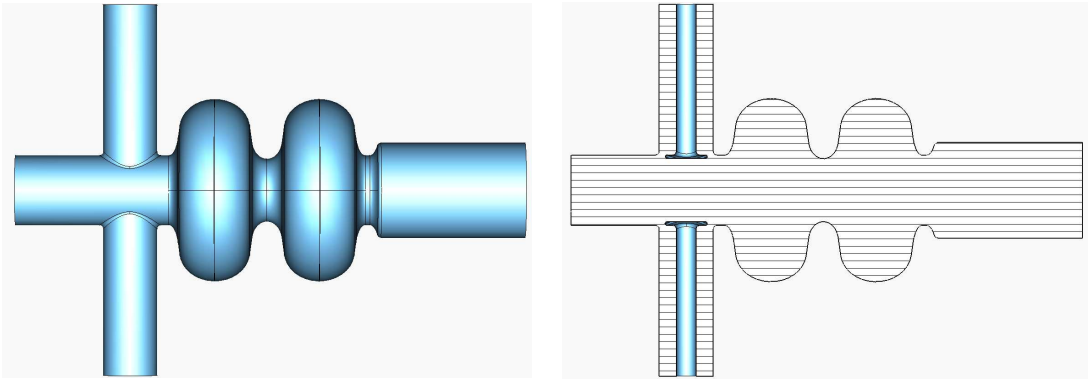

(a) Exterior view of the MWS injector cavity model.

(b) Cutaway view of the MWS injector cavity model.

Figure 4.4: (a) The Microwave Studio model of ERL injector cavity: (a) the cavity and coupler exterior, (b) cutaway view of the same model showing the inner coupler antennae.

The procedure for correctly constructing the fields in the coupler and cavity requires two sets of MWS solutions. Each set of fields was created by terminating the input coupler line in the MWS model with either an electric or magnetic wall boundary condition [54]. From these solutions, traveling waves carrying power into and out of the cavity through the couplers were constructed, scaled, and shifted in phase to match the actual running conditions in the injector. In order to further limit the beam power deposited in our interceptive EMS, the pulse train from the 50 MHz laser was chopped using a Pockels cell. The resulting beams typically had currents on the order of a micro-amp or less. In generating the field maps for the accelerating cavities, this amounts to effectively

having zero current. The parameter which determines how the cavity fields depend on the operating parameters is the reflection coefficient [54]:

$$\Gamma = -\frac{\frac{1-\beta}{1+\beta} + \frac{I_b}{V_c}(R/Q)Q_L e^{-i\phi_0} + i\tan\psi'}{1 + \frac{I_b}{V_c}(R/Q)Q_L e^{-i\phi_0} + i\tan\psi'} \tag{4.4}$$

Here I_b and ϕ_0 are the average beam current and phase of the beam with respect to the cavity fields. The rest of the parameters in this expression describe the properties of the cavities: β is the coupling parameter, Q is the intrinsic cavity quality factor, R is the shunt resistance, V_c is the cavity voltage, $Q_L = Q_0/(1+\beta)$ is the loaded quality factor, and $\tan\psi'$ is the cavity detuning parameter. In the zero current limit (with the cavity tuned to resonance), the reflection coefficient reduces to

$$\Gamma(I_b \to 0) = \frac{\beta - 1}{\beta + 1}. \tag{4.5}$$

This implies that the fields in the cavity and coupler coax depend only on the amount of coupling. The coupling factor β is determined by how far the inner coupler antennae are retracted from being flush with the beam pipe. For our emittances measurements, the couplers were fully retracted (zero current setting). By fully retracting the coupler antennae in the MWS model, and generating two set of solutions for both boundary conditions on the end of the coupler coax, we created one set of complex 3D electric and magnetic field maps for the SRF cavities. Fig. 4.3(f) shows the resulting on-axis electric field. We point out that simulations subsequently showed that the asymmetric emittances caused by the RF quad effect in the cavities could be successfully remedied by appropriate choice of magnetic quadrupole focusing downstream.

After completing the GPT physics model of the injector, we developed a user interface between the real machine and its GPT counterpart. Named the "Virtual Accelerator GUI", this program was designed to provide a single interface between the corresponding optics settings in the EPICS control system of the real machine, and the stand alone

GPT code. Additional features include the ability to save and load optics settings and simulation results to and from file, the ability to load injector settings from the machine and independently adjust them in simulation, as well as the ability to visualize all relevant simulation data. A screen shot of this application is shown in Fig. 4.5.

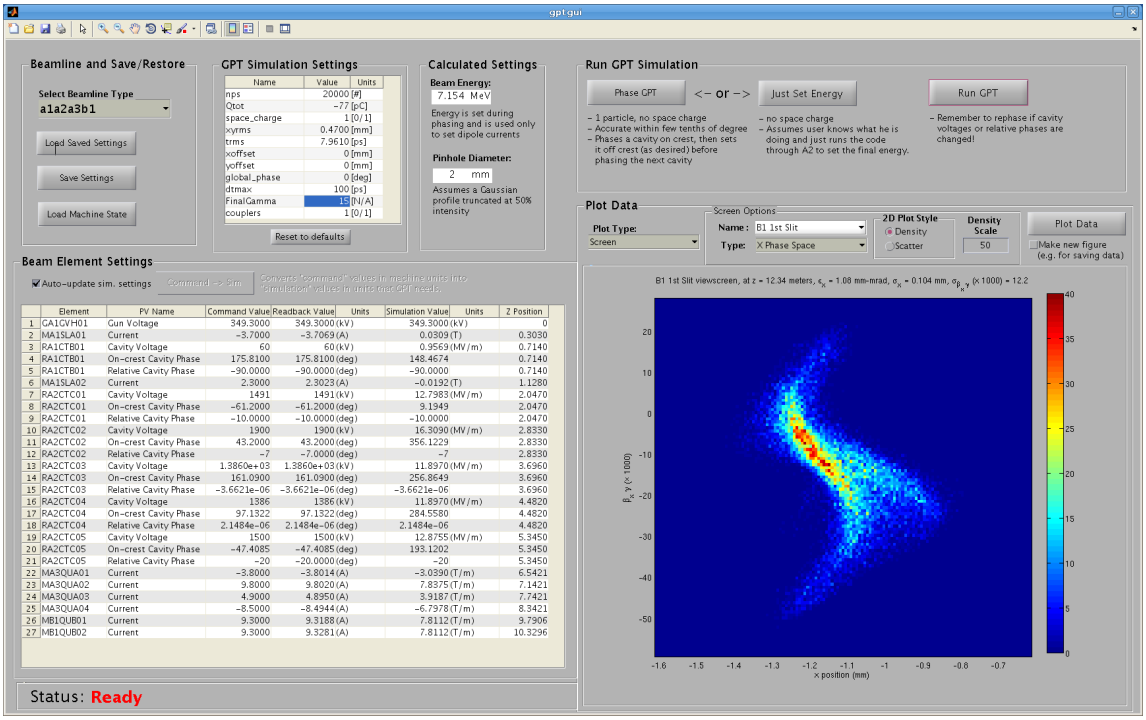

Figure 4.5: Screenshot of the Virtual Accelerator GUI.

In constructing this program, a master GPT input file was created which included not only the optical elements described in this section, but also simulation output screens at all of the corresponding locations of the beam position monitors (BPMs), viewscreens, and emittance measurement systems in the injector. The result was a nearly one-to-one simulation counterpart to the real machine. With this, we were able to use GPT in a more useful and realistic way, with simulations often guiding experiments in near real-time in the control room.

4.4 Measurements

All of the measurements in this work fall into one of two categories: measurements performed at near-zero bunch charge for verification and calibration purposes; or phase space measurements of space charge dominated bunches.

4.4.1 Measurements at Near-Zero Bunch Charge

The measurements presented in this section include: comparison of difference orbits (linear optics) in the injector with the GPT model including the effects of the RF input couplers, measurement of the beam size envelope along the injector and its verification with simulation, and calibration of the EMS and analysis procedures by comparing the emitance computed from the direct measurement of the projected transverse phase spaces in the merger and the emittance measured using a solenoid scan in the gun vicinity. In order to accurately perform difference orbit measurements, the BPM system needed to be corrected for its non-linear response, the procedure for which is presented below.

4.4.1.1 BPM Correction Procedure

The injector BPMs consist of four striplines, as seen in Fig 4.6(a). To model the system we make two assumptions: (i) both the beam pipe and striplines are assumed to be infinitely long perfect conductors connected to ground; and (ii) the beam is taken to be an infinite line charge at the position $\mathbf{r}_b = (x_b,\ y_b)$. The first assumption implies that the potential must vanish at the beam pipe. This is accomplished by placing an image line charge with opposite charge density at $\mathbf{r} = (R^2/r_b^2)\mathbf{r}_b$. The resulting electric field everywhere is:

$$\mathbf{E}(\mathbf{r}, \mathbf{r}_b) = \frac{\lambda}{2\pi\epsilon_0}\left[\frac{\mathbf{r}-\mathbf{r}_b}{|\mathbf{r}-\mathbf{r}_b|^2} - \frac{\mathbf{r}-(R^2/r_b^2)\mathbf{r}_b}{|\mathbf{r}-(R^2/r_b^2)\mathbf{r}_b|^2}\right].$$

From the electric field, the surface charge density on the beam pipe and striplines can be computed using $\sigma = -\epsilon_0 \mathbf{E}(\mathbf{R}, \mathbf{r}_b) \cdot \hat{\mathbf{n}}$, where $\hat{\mathbf{n}}$ is the normal vector to the beam pipe surface. Since this model assumes the beam pipe is a perfect conductor, the field is perpendicular to the surface so that $\mathbf{E}(\mathbf{R}, \mathbf{r}_b) \cdot \hat{\mathbf{n}} = |\mathbf{E}(\mathbf{R}, \mathbf{r}_b)|$. In cylindrical polar coordinates, the surface charge density takes the form

$$\sigma(R, \theta, r_b, \theta_b) = \frac{\lambda}{2\pi} \left(\frac{(r_b^2/R^2) - 1}{R^2 + r_b^2 - 2Rr_b \cos(\theta - \theta_b)} \right) R.$$

The angles θ and θ_b are defined in Fig 4.6(a). The signal from the i^{th} stripline is defined as the fraction of the surface charge density found on that stripline:

$$S_i(x_b, y_b) = \frac{1}{\lambda} \int_{\theta_i - \theta_s/2}^{\theta_i + \theta_s/2} \sigma(R, \theta, x_b, y_b) R \mathrm{d}\theta. \tag{4.6}$$

Here the angle θ_s is the angle subtended by each stripline. Performing the integration yields:

$$S_i(x_b, y_b) = \\ -\frac{1}{\pi} \tan^{-1} \left[\left(\frac{R + r_b}{R - r_b} \right) \tan \left(\frac{\theta - \theta_b}{2} \right) \right] \Bigg|_{\theta_i - \theta_s/2}^{\theta_i + \theta_s/2}, \tag{4.7}$$

where $\theta_i \in \{0,\ \pi/2,\ \pi,\ 3\pi/2\}$.

In order to invert the BPM signals and obtain the beam position, the signals from Eq. (4.7) are fit to the injector BPM signals using a χ^2-minimization with the beam position as the fit parameters. To verify this procedure, a pair of upstream horizontal and vertical corrector magnets was scanned in a grid pattern and the response on a test BPM was measured. Fig 4.6(b) shows the comparison of the standard linear BPM model (blue), and non-linear model given by Eq. (4.7) (red). The inclusion of this model effectively extended the workable range of the BPMs in the injector by roughly a factor of two. This increased range made the use of the BPMs in response measurements significantly more robust.

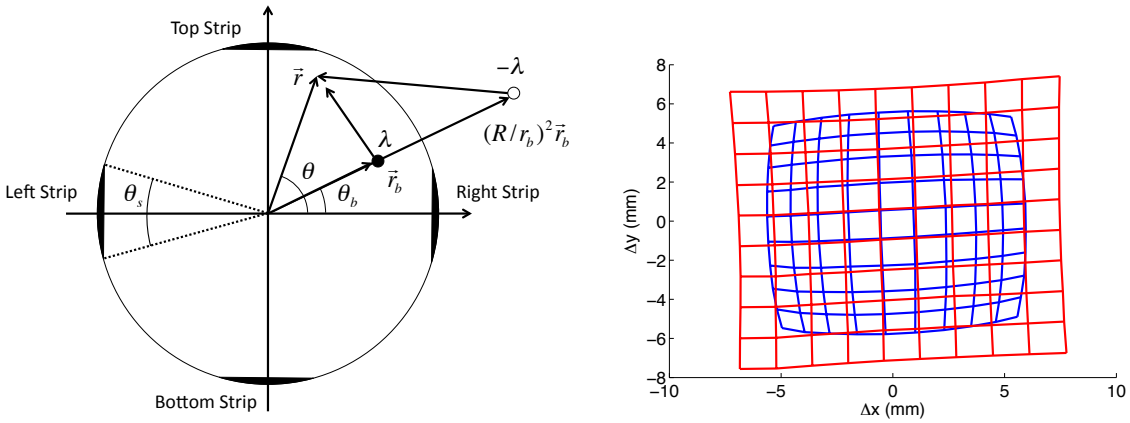

(a) Parameters for the non-linear BPM model. (b) Comparison of linear and non-linear BPM models.

Figure 4.6: Non-linear BPM model description and verification: (a) shows the relevant parameters for the model, while (b) shows the comparison of the standard linear BPM position calculation (blue) and positions computed with a non-linear correction (red) from a square grid scan of an upstream horizontal and vertical corrector pair.

4.4.1.2 Difference Orbits and Coupler Effects

To verify each injector beamline element and its corresponding GPT model, linear optics response measurements have been performed. The transverse dynamics were verified by changing the initial position of the beam on the cathode or kicking the beam with a corrector magnet and recording the change in position on all downstream BPMs. This was repeated for each type of element in the injector, starting with the gun and moving downstream turning on elements one by one and comparing the resulting response function to GPT simulations. Fig. 4.7(a) shows an example response measurement and corresponding GPT comparison. For this measurement, the first pair of horizontal and vertical correctors in the A1 section were scanned and the response through the straight portion of the injector recorded (with all quadrupoles off). Time of flight difference orbits were also measured by adjusting the laser phase ±60 degrees relative to the cavity phases, and measuring the bunch arrival phase from all BPMs via I/Q detection and bunch signal processing.

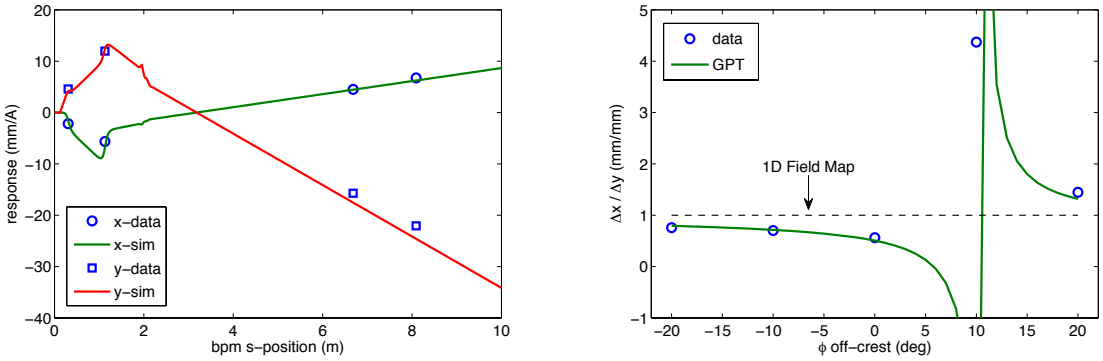

(a) Example response measurement.

(b) Asymmetric response through the second cavity due to coupler fields.

Figure 4.7: Response measurements: (a) the response from the set of correctors through first SRF cavity. The cavity was set to 1 MV on-crest. (b) The response asymmetry due the coupler fields in the second cavity as a function of cavity phase. The cavity voltage was 1.5 MV. The dashed line shows the expected response from a cylindrically symmetric, or 1D field map model of the cavity.

Excellent agreement with the GPT model was obtained using all BPMs, including those in the merger.

Difference orbits were also used to verify the 3D RF field maps used to model the cavities and fields near the input power couplers. Simulations show that asymmetric focusing from the couplers is worse when a low energy beam passes through the coupler fields before being accelerated [54]. Thus to more clearly measure the effects of the couplers, we turned off all of the SRF cavities except the second one, which has couplers at the entrance of the cavity, as seen by the beam. A square grid of angles was scanned using the last pair of horizontal and vertical correctors just before the entrance to the cryomodule, and the resulting response pattern was measured on a downstream BPM. This was repeated at multiple cavity phases shifted relative to the on-crest phase. By taking the ratio of the change in position in x to the change in y, the asymmetry in the response through the cavity was computed. Fig. 4.7(b) shows the comparison of the x to y response aspect ratio

measured in the injector and computed in GPT. The agreement is quite good except for the point where the response in both planes goes through zero. With these measurements, we are confident in our ability to include the 3D focusing effects of the cavity input couplers.

4.4.1.3 Alignment

Previous work has shown [32, 34, 35] that good alignment through each optical element is required to diminish emittance growth, and indeed alignment of the beam through the gun, emittance compensation section, and SRF cavities proved very important for obtaining the low emittance results presented here. In order to arrive at these results, a methodical element by element alignment procedure was developed. The benefit of such an approach was that after a thorough execution of the following procedure, additional alignment work was kept to a minimum on subsequent experiments.

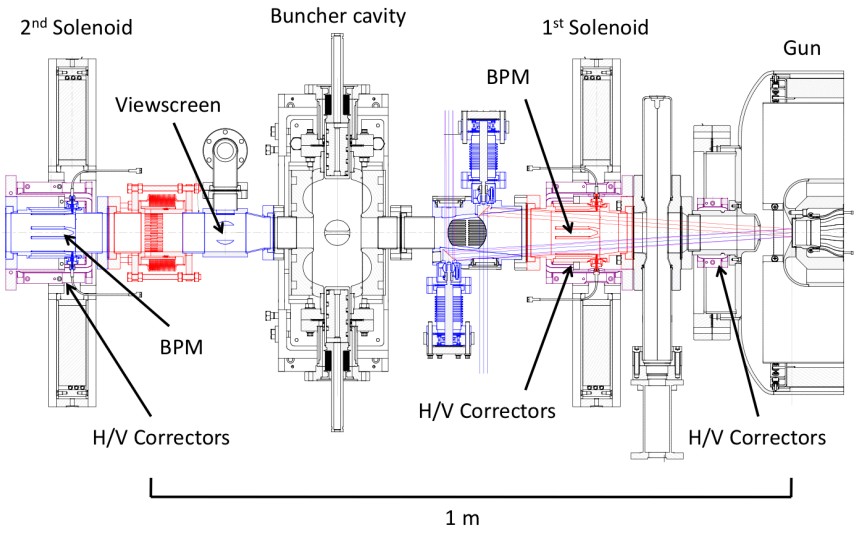

Figure 4.8: Layout of the A1 emittance compensation section.

The first step of this procedure was to center the laser spot on the cathode. To do so, the spot was scanned both horizontally and vertically to form a grid of positions. With the

first solenoid off, the corresponding beam position was recorded on the viewscreen after the gun, see Fig. 4.8. Fitting the response data to an off-axis expansion of the gun focusing allowed us to the determine electrostatic center of the gun/cathode to within 50 μm. It should be noted that in order to achieve a good cathode lifetime, off-center laser spot operation is required to minimize ion back-bombardment [26]. However, we found that offsetting the laser spot by 3 mm and using a corrector pair to bring the beam back through the center of the 1st solenoid did not degrade the beam emittance by more than 5%.

After aligning to the gun, the beam was then aligned in the buncher cavity. To do so, the gun was set to 350 kV, and the first and second solenoids were degaussed and turned off. The buncher cavity was turned on at 50 kV and the two energy zero-crossing phases determined. In order to keep the transverse beam size small, the cavity phase was set to the de-bunching zero-crossing value, in order to provide focusing from the buncher. The use of the zero-crossing phase also eliminated the effect of dispersion due to the combination of unwanted stray fields and low beam energy. The beam position on the second viewscreen was recorded with the cavity turned off and then turned on. The initial position offset going into the cavity field region was then found by fitting the beam transfer matrix from the corrector coil pair just before the buncher to the viewscreen after the cavity. The transfer matrix was computed from the on-axis electric field map shown in Fig. 4.3(e) using the method derived in [54]. The position offset in the buncher was then compensated by adjusting the corrector coils just before it. Using this technique, we were routinely able to align the beam through the center of the buncher to within 20 μm.

Next, the orbit was aligned through the first two SRF cavities. Each cavity was separately turned on to 50 kV and set to the de-bunching zero-crossing phase just as with the buncher. Once the correct phases were found, the beam position on the A3 viewscreen was recorded for three different settings: both cavities off, and then each cavity

on separately. After recording the beam position on the A3 viewscreen for each setting, the response functions from the last two pairs of horizontal and vertical correctors before the cryomodule were measured. From this set of response measurements, the corrector settings were determined that would place the beam at the same spot on the A3 viewscreen for all three cavity settings. This process produced an orbit which did not change position on the A3 viewscreen to within roughly 50 μm when the first two cavities were toggled on and off.

Finally, the solenoids were aligned. The alignment of the buncher and first two SRF cavities fixed the settings of all the available corrector coils in the A1 section. Consequently, the solenoids had to be physically moved to align their magnet centers with beam orbit. For the solenoids, both their offset and angle in the horizontal and vertical planes were found by performing a current scan of each magnet, recording the response on a downstream viewscreen, and fitting the data using the transfer matrix of the solenoid [43, 82]. The physical adjustment of the solenoid positions and angles was greatly aided by the incorporation of alignment motors in the design of the solenoid magnet support structure. At the completion of the final alignment measurements, the transverse offsets of the solenoids were aligned to within roughly 50 μm, and the transverse angles to within 0.2 mrad.

Alignment of the orbit through the optical elements in the A3 straight and B1 merger section was achieved by flattening the BPM readings in these sections. To check the overall alignment once the orbits for emittance measurements were set up, a special laser mask with a regular grid of 100 μm holes spaced 0.75 mm apart, was placed in the laser path. Fig. 4.9 shows the initial grid pattern and the measured grid pattern in the B1 section. To generate this image the buncher was purposefully set to give a longer bunch length in order to exaggerate the time dependent RF focusing from the SRF cavities. In this image, the center spot being circular and the other spots pointing towards the center indicates that the

beam is aligned reasonably throughout the injector. Also, the lack of curvature to each of the spots/lines indicates that aberration effects are minimal.

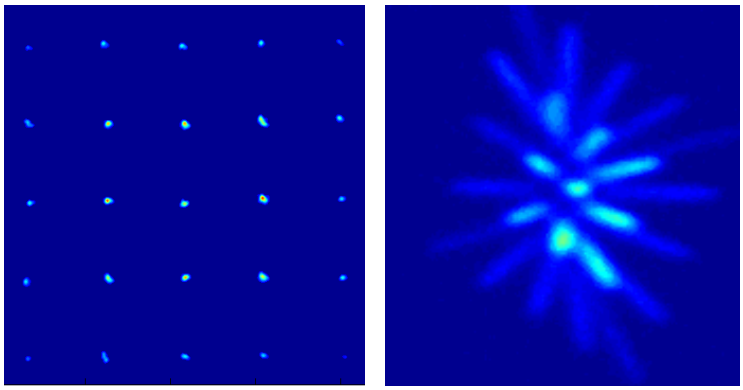

(a) Initial grid of laser spots as measured on the laser ccd.

(b) Resulting beam image on the viewscreen at the end of the B1 merger.

Figure 4.9: Alignment check using a grid of laser spots (a) and the resulting beam image on the viewscreen at the end of the B1 merger section (b).

4.4.1.4 Beam Sizes and Thermal Emittance

Before measuring emittance with nonzero bunch charge, we calibrated our emittance measurement system and emittance analysis scripts by measuring the emittance at near-zero bunch charge ($q \leq 0.03$ pC). A baseline thermal emittance was measured after the gun and before the cryomodule by scanning the current of the first solenoid and measuring the beam spot size on a viewsreen downstream. By computing the linear transfer matrix through the combined gun and solenoid fields, the emittance and initial rms beam spot size were found using the method in [82]. Fig. 4.10(a) and 4.10(b) show the solenoid scan data and fitted curve for the cathode used in this work. The resulting horizontal and vertical emittances measured with the solenoid current scan were 0.12 ± 0.01 μm and 0.11 ± 0.01 μm respectively. To check the calibration of the EMS in the merger section, the projected

horizontal and vertical phase space, as well as the horizontal time-resolved phase space were measured. For these measurements, the 19 pC/bunch injector optics settings were used (see Table 4.2), however the bunch charge was reduced so that space charge effects were negligible.

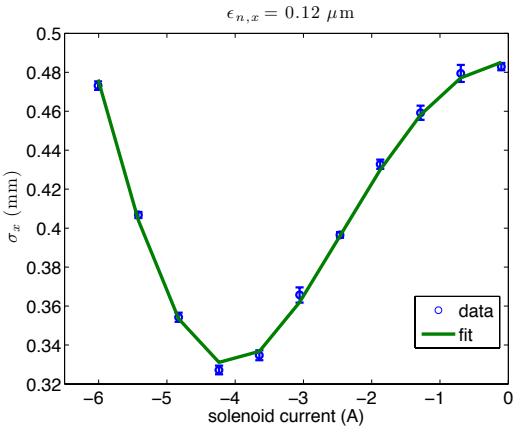

(a) Solenoid scan horizontal emittance data.

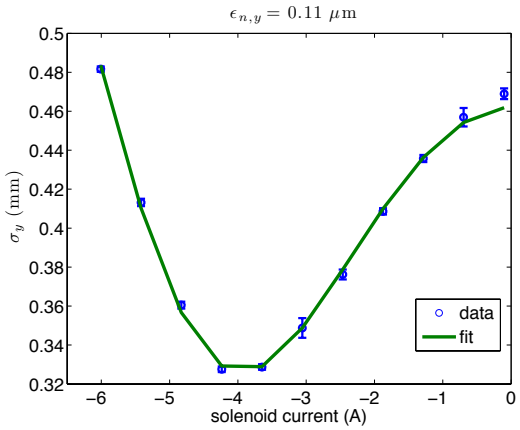

(b) Solenoid scan vertical emittance data.

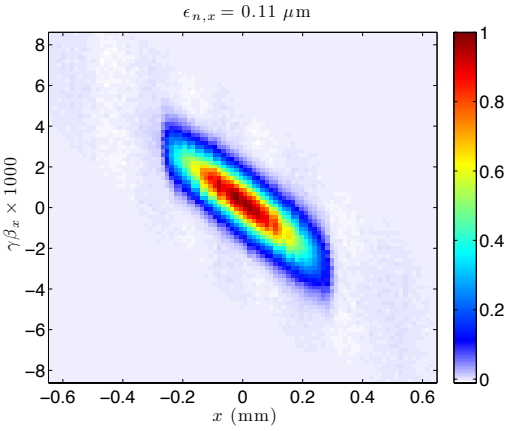

(c) Horizontal phase space in the merger.

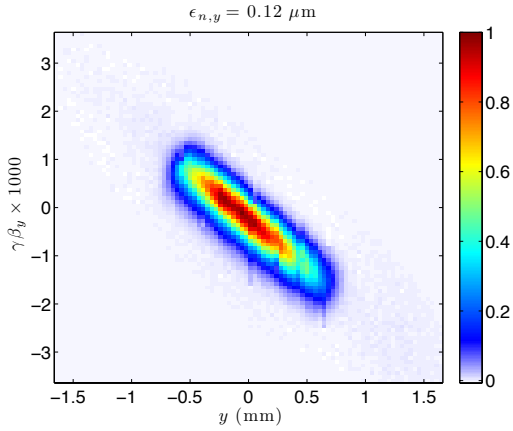

(d) Vertical phase space in the merger.

Figure 4.10: Projected emittance measurement at the cathode using a solenoid scan (a-b), and corresponding measurements in the merger section (c-d). Both the horizontal and vertical emittance measured in the merger section agreed to within 9% of values measured at the cathode. The colormap and normalization in (c-d) is used for all subsequent phase-space plots in this work. The estimated error in for these emittance values was ± 0.01 μm.

Fig. 4.10(c) and Fig. 4.10(d) show the projected emittance measured in the B1 merger section with a beam momentum of roughly 8 MeV/c. The estimated systematic error in the calibration of the merger EMS system was less than 7%. The horizontal and vertical emittances from these measurements were 0.11 ± 0.01 and 0.12 ± 0.01, which agree with the solenoid scan results to within the estimated error in both measurements. The same value for the horizontal projected emittance, 0.11 ± 0.01 μm, was measured in the merger section using the time-resolved EMS. These measurements not only verified the EMS diagnostics and analysis procedures, but also provided an additional check of the orbit alignment.

As a final check of the optics settings in the machine and simulations, we measured the transverse rms beam sizes at several locations along the injector with near-zero bunch charge.

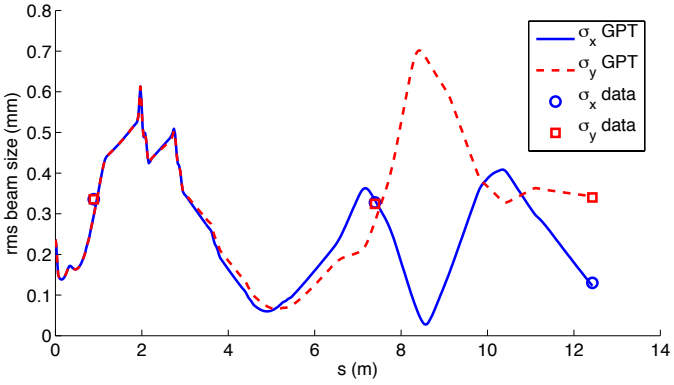

Figure 4.11: Comparison of simulated and measured rms spot sizes along the beam line.

Fig. 4.11 shows the comparison of the simulated and measured rms spot sizes. The optics settings were the same as those used in the EMS calibration measurements. The measured values were computed from images of the beam on the A1 and A3 viewscreens, and from the phase spaces measured in the merger section shown in Fig. 4.10(c) and Fig. 4.10(d). The systematic uncertainty in these measurements due to the viewscreen calibration and set-up resolution was estimated to be less than 5% for the direct viewscreen

measurements. As Fig. 4.11 shows, excellent agreement between GPT and the measured beam sizes was found.

4.4.2 Measurements with Space Charge

Two main data sets were produced for this work: one at 19 pC per bunch, and one at 77 pC. These correspond to 25 mA and 100 mA average current when operating at the full 1.3 GHz repetition rate. Each data set consists of a measurement of the projected horizontal and vertical phase spaces, the time-resolved horizontal phase space, and the energy spread distribution. All data was taken at the end of the merger section except the energy spread data, which was measured using the A4 straight section and C2 bend section. From the projected phase space the horizontal and vertical emittance as a function of beam fraction was computed. Similarly, from the time-resolved phase spasce data, the slice emittance was computed as a function of beam fraction, as well as the current profile along the bunch. Refer to Appendix A for the emittance definitions used to characterize non-Gaussian phase spaces.

4.4.2.1 Injector Settings and Simulation Parameters

To arrive at the final optics used for these experiments, optimizations of the GPT model were carried out using a multi-objective genetic algorithm [34, 74]. In general, each optimization was run with two competing objectives (e.g. minimizing the emittance at the location of the merger EMS and maximizing the bunch charge), while varying the optics settings (e.g. solenoid, rf, and quad settings). Upon convergence of the optimizer, this produced an optimal front for the two objective variables. A complete list of the parameters varied in the optimizer can be found in the first and second columns of Table 4.2. Note that

for all optimizations, the gun voltage was fixed at 350 kV, and the beam energy was constrained to be ≤ 8 MeV to reduce neutron production from the tungsten slits in the EMS. The simulated temporal laser distribution was fixed to be roughly a flat-top with 8 ps rms length, and was generated by adding 16 Gaussian pulses in accordance with the temporal laser shaping system used for the injector [83]. The transverse laser profile was a Gaussian truncated at 50% intensity with the resulting rms size varied in the optimizations.

Each simulation was run with a set of constraints which ensured the physicality of the results and pushed the optimizer to explore regions of the variable space relevant to achieving the injector design goals. The two most important constraints were the rms bunch length: $\sigma_t \sim 2$ ps, and the rms energy spread $\sigma_\delta \sim 0.1$ to 0.2 %. Note that these values are slightly more stringent than the quoted design goals in Table 4.1.

Optics solutions from the last set of optimizations were loaded into the GPT virtual accelerator GUI, and then tested in the injector. Doing so led to the recognition of a common feature to all of the optimized solutions: the optimizer always focused the beam through a waist at exactly the position of the EMS in the merger. As the experiment proceeded, another general trend was observed using the virtual accelerator GUI. Optimized solutions which kept the beam sizes small, particularly in the straight section and merger, gave better measured emittance results. The settings used in the final measurements presented here were both derived from one optimization solution for 50 pC bunch charge, as this optics setting kept the beam sizes reasonably small through the entire injector. Using this parameter set as a starting point in our virtual accelerator interface, the bunch charge was reduced from 50 to 19 pC while adjusting the magnet and buncher settings to compensate for the reduced space charge effects, as well as scaling the laser spot diameter in accordance with $\sigma_{x,y} \propto \sqrt{q}$. This allowed us to keep the simulated spot sizes small through the injector, while also maintaining the location of the beam focus at the position

of the merger EMS. The procedure was then started over, raising the charge from 19 to 77 pC. This time the phases of the first two SRF cavities, and the voltage and phase of the last SRF cavity were also adjusted in order to maintain small emittance values at the merger EMS.

These settings were then loaded into the injector and the measured projected emittance was minimized by scanning both solenoid currents and adjusting the intensity cut off value in the measured transverse laser profile. Fig. 4.12 shows the measured laser profiles for used in the final measurements and the corresponding profiles used in the final GPT simulations. The final solenoid currents used in the injector were within 3% of the simulation values. The quads in the B1 section were also adjusted slightly for both optics settings, but kept within 4% of the simulations. These slight adjustments to the simulated injector settings are believed to be a consequence of hysteresis effects in the magnets, as well as error in the calibration factors used to convert machine parameters to simulation parameters. Fig. 4.13 shows the rms beam sizes, projected horizontal and vertical emittances, kinetic energy, and bunch lengths computed using the final simulation optics values. Table 4.2 shows injector settings and parameters used in measurements. The beam kinetic energy measured after the cryomodule was 7.5 and 7.7 MeV for the two bunch charges respectively.

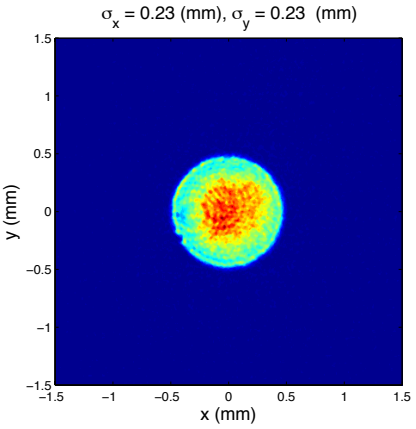

(a) Laser spot for the 19 pC/bunch data set.

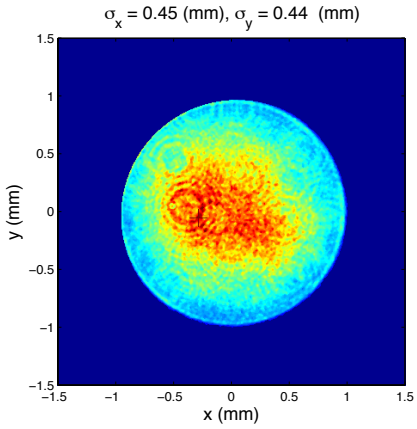

(b) Laser spot for the 77 pC/bunch data set.

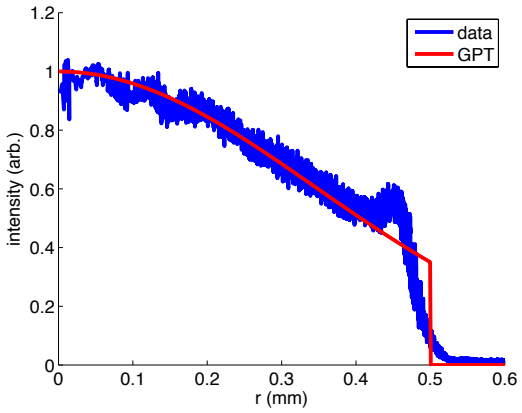

(c) Radial laser intensity for the 19 pC/bunch settings.

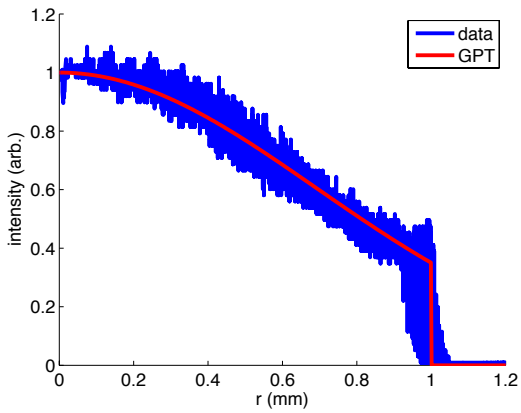

(d) Radial laser intensity for the 77 pC/bunch settings.

Figure 4.12: Verification of the initial transverse laser spot in the injector and GPT input file: (a) and (b) show the measured laser spot on a ccd camera as they would appear on the cathode. The uncertainty in the rms spot sizes is (a) ±0.01 mm, and (b) ±0.02 mm. The plots in (c) and (d) show the corresponding measured radial laser intensity (blue) and matching truncated Gaussian (red) used in simulation.

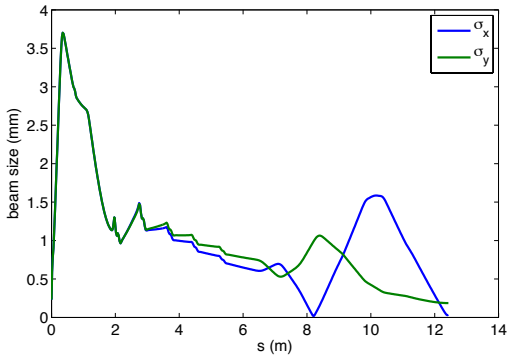

(a) RMS beam sizes for 19 pC/bunch.

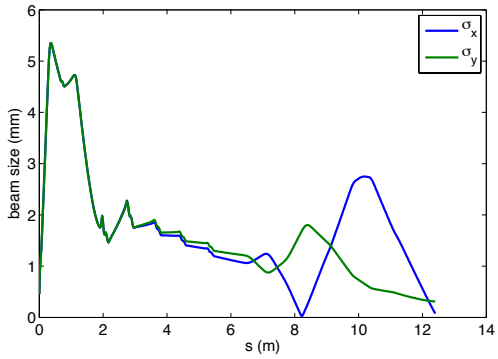

(b) RMS beam sizes for 77 pC/bunch.

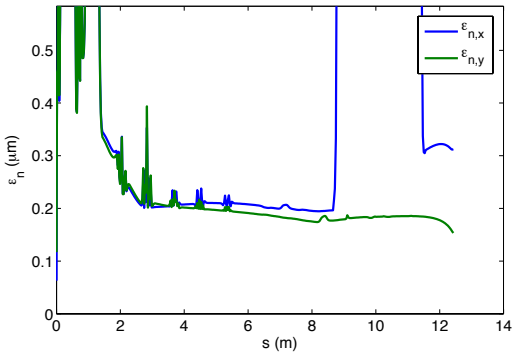

(c) Projected emittance for 19 pC/bunch.

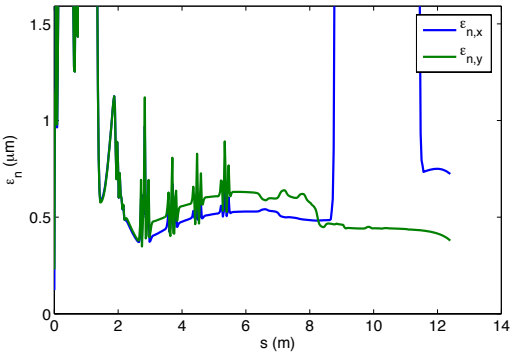

(d) Projected emittance for 77 pC/bunch..

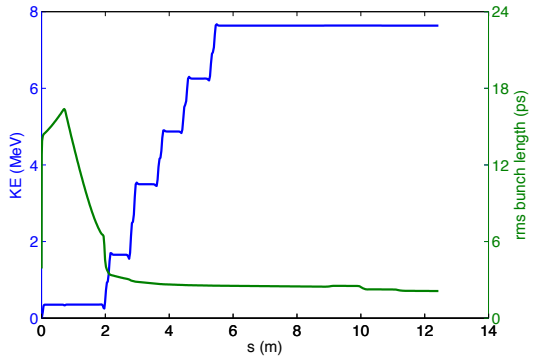

(e) Kinetic energy and bunch length for 19 pC/bunch

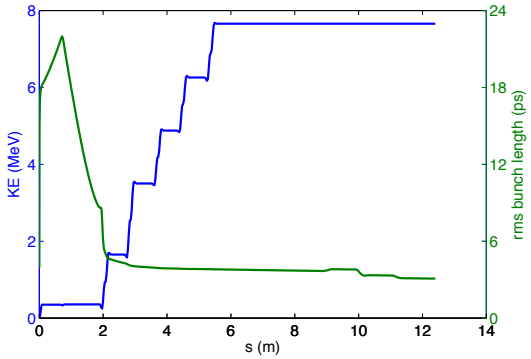

(f) Kinetic energy and bunch length for 77 pC/bunch.

Figure 4.13: Simulation data for the 19 pC/bunch (left) and 77 pC/bunch (right) injector settings: (a-b) show the rms beam size along the injector, (c-d) show the projected horizontal and vertical emittances, and (e-f) shows both the kinetic energy (left axis) and rms bunch length (right axis).

4.4.2.2 Projected Emittance Results

As previously discussed, measuring low projected emittance after the merger section that scales according Eq. (4.1), and meets the design specification of the injector was one the main goals of this work. Tables 4.3(a) and 4.3(b) show the best projected emittance data from measurement as well as the corresponding GPT simulation values. The measured emittance data was processed with removal of a near constant background via an automatic bias determination routine similar to the methods described in [32, 93]. The processed data was then used to determine the 100% beam emittance, as well as to generate the emittance vs. fraction curve, defined in Eqs. (A.2) and (A.3), and the corresponding core emittance and core fraction, defined in Eq. (A.4). These curves are shown for the horizontal and vertical projected phases at 19 (77) pC/bunch in Fig. 4.14. All of these procedures were automated and available to operators in the control room after each emittance measurement scan (lasting typically several seconds). Further details of the data processing and experimental procedures can be found in Appendix!!!! The measured 19 (77) pC/bunch horizontal and vertical projected 100% emittances agreed with the GPT model to within 6 (5) % and 25 (8) %, respectively. Similarly, the measured horizontal and vertical 90% emittances agreed with GPT to within 21 (16) % and 27 (16) %, respectively. We point out that the measured horizontal and vertical 100%, 90%, and core emittances obey the expected scaling law $\epsilon_n \propto \sqrt{q}$. Also of note is the fact the horizontal core emittance for 77 pC meets the injector design specification for an ERL. In the vertical plane, both the 90% and core emittance meet this specification. For comparison purposes, Fig. 4.15(a) and Fig. 4.15(b) show the measured and simulated phase spaces after the merger for both the horizontal and vertical planes with near-zero, 19, and 77 pC/bunch.

Table 4.2: Injector optics settings.

Element	Parameter	19 pC/bunch Values	77 pC/bunch Values
laser	pinhole (mm)	1	2
laser	intensity cut off (%)	40	35
laser	rms pulse length (ps)	8	8
DC gun	voltage (kV)	350	350
solenoid 1	peak field (T)	0.032	0.031
buncher	voltage (kV)	50	60
buncher	phase (deg)	-90	-90
solenoid 2	peak field (T)	-0.020	-0.020
SRF cavity 1	voltage (kV)	1491	1491
SRF cavity 1	phase (deg)	-10	-10
SRF cavity 2	voltage (kV)	1953	1953
SRF cavity 2	phase (deg)	-16	-7
SRF cavity 3	voltage (kV)	1386	1386
SRF cavity 3	phase (deg)	0	0
SRF cavity 4	voltage (kV)	1386	1386
SRF cavity 4	phase (deg)	0	0
SRF cavity 5	voltage (kV)	1386	1500
SRF cavity 5	phase (deg)	0	-20
A3 quad 1	$\int G(z)\mathrm{d}z$ ([T/m]·m)	0.013	0.013
A3 quad 2	$\int G(z)\mathrm{d}z$ ([T/m]·m)	-0.033	-0.033
A3 quad 3	$\int G(z)\mathrm{d}z$ ([T/m]·m)	-0.016	-0.016
A3 quad 4	$\int G(z)\mathrm{d}z$ ([T/m]·m)	0.029	0.029
B1 quads	$\int G(z)\mathrm{d}z$ ([T/m]·m)	-0.017	-0.016

Table 4.3: Measured and simulated projected horizontal (a), and vertical (b) emittances. Emittance values are quoted in [μm].

(a) Horizontal projected emittance data.

19 pC Data Type	$\epsilon_{n,x}(100\%)$	$\epsilon_{n,x}(90\%)$	$\epsilon_{n,x}(\text{core})$	f_{core}	$\epsilon_{n,x}(\text{core})/f_{\text{core}}$
Projected EMS	0.33 ± 0.02	0.23 ± 0.02	0.14 ± 0.01	67%	0.21 ± 0.01
Time-res. EMS	0.28 ± 0.02	0.21 ± 0.01	0.14 ± 0.01	72%	0.19 ± 0.01
Simulation	0.31	0.19	0.07	59%	0.12
77 pC Data Type	$\epsilon_{n,x}(100\%)$	$\epsilon_{n,x}(90\%)$	$\epsilon_{n,x}(\text{core})$	f_{core}	$\epsilon_{n,x}(\text{core})/f_{\text{core}}$
Projected EMS	0.69 ± 0.05	0.51 ± 0.04	0.28 ± 0.2	64%	0.44 ± 0.03
Time-res. EMS	0.66 ± 0.05	0.48 ± 0.04	0.29 ± 0.2	67%	0.43 ± 0.03
Simulation	0.72	0.44	0.17	51%	0.33

(b) Vertical projected emittance data.

19 pC Data Type	$\epsilon_{n,y}(100\%)$	$\epsilon_{n,y}(90\%)$	$\epsilon_{n,y}(\text{core})$	f_{core}	$\epsilon_{n,y}(\text{core})/f_{\text{core}}$
Projected EMS	0.20 ± 0.01	0.14 ± 0.01	0.09 ± 0.01	70%	0.13 ± 0.01
GPT Simulation	0.16	0.11	0.06	64%	0.09
77 pC Data Type	$\epsilon_{n,y}(100\%)$	$\epsilon_{n,y}(90\%)$	$\epsilon_{n,y}(\text{core})$	f_{core}	$\epsilon_{n,y}(\text{core})/f_{\text{core}}$
Projected EMS	0.40 ± 0.03	0.29 ± 0.02	0.19 ± 0.01	70%	0.27 ± 0.01
GPT Simulation	0.37	0.25	0.11	59%	0.19

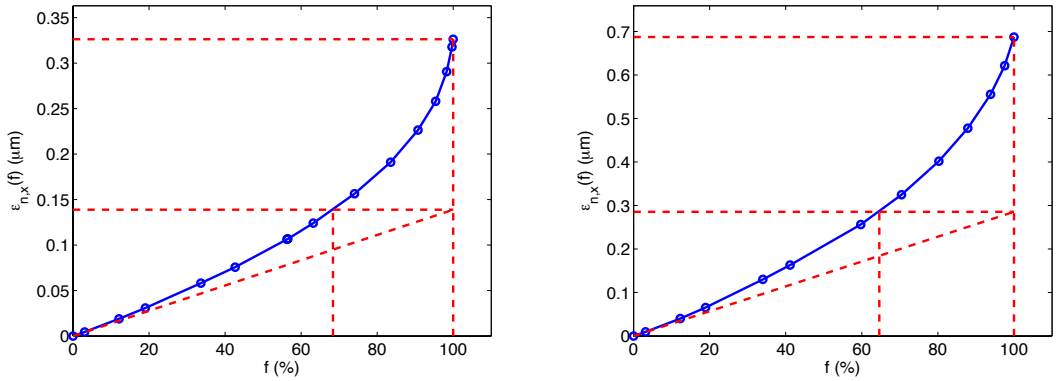

(a) Horizontal 19 pC/bunch data.

(b) Horizontal 77 pC/bunch data.

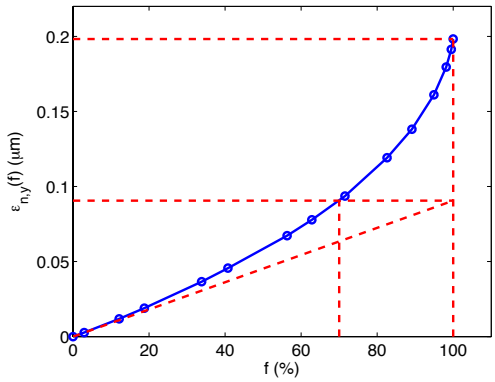

(c) Vertical 19 pC/bunch data.

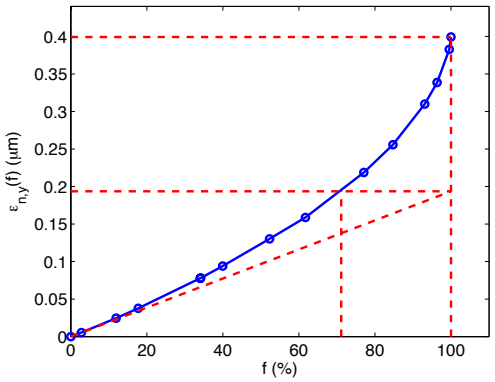

(d) Vertical 77 pC/bunch data.

Figure 4.14: Emittance versus fraction curves: (a-b) the curves computed from the measured horizontal phase space data at 19 and 77 pC/bunch, (c-d) the curves computed from the measured vertical phase space data at 19 and 77 pC/bunch.

4.4.2.3 Time-resolved Phase Space and Energy Spread Results

In order to satisfy the injector design requirements, it was important to verify that the emittance values were measured with an acceptable bunch length ($\sigma_t \leq 3$ ps). The rms bunch length was computed from the instantaneous current of each bunch measured with the time-resolved merger EMS. Fig. 4.16(a) and 4.16(b) shows both the measured and simulated bunch current for the 19 pC/bunch and 77 pC/bunch data, respectively. The

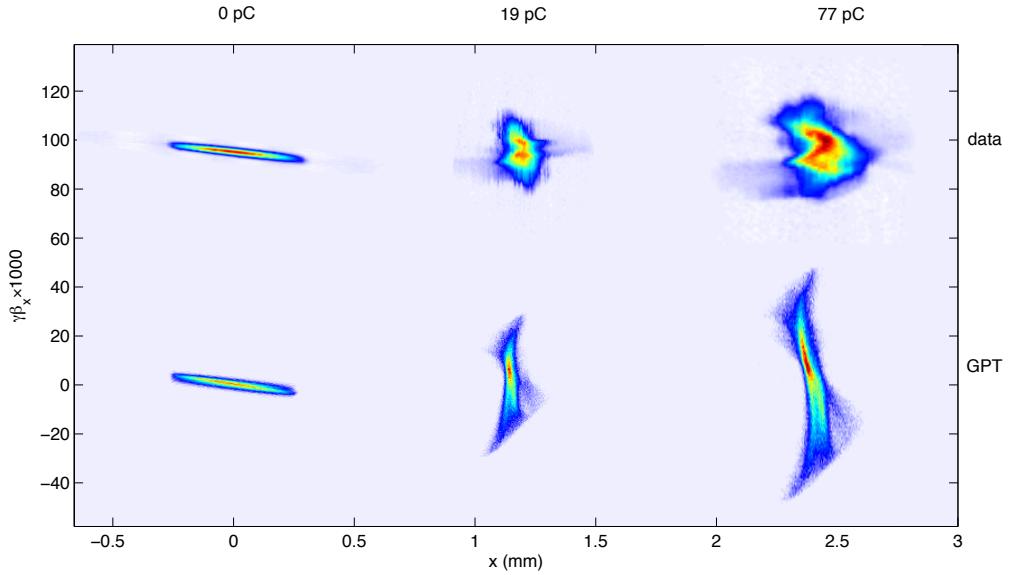

(a) Horizontal phase-space as a function of bunch charge.

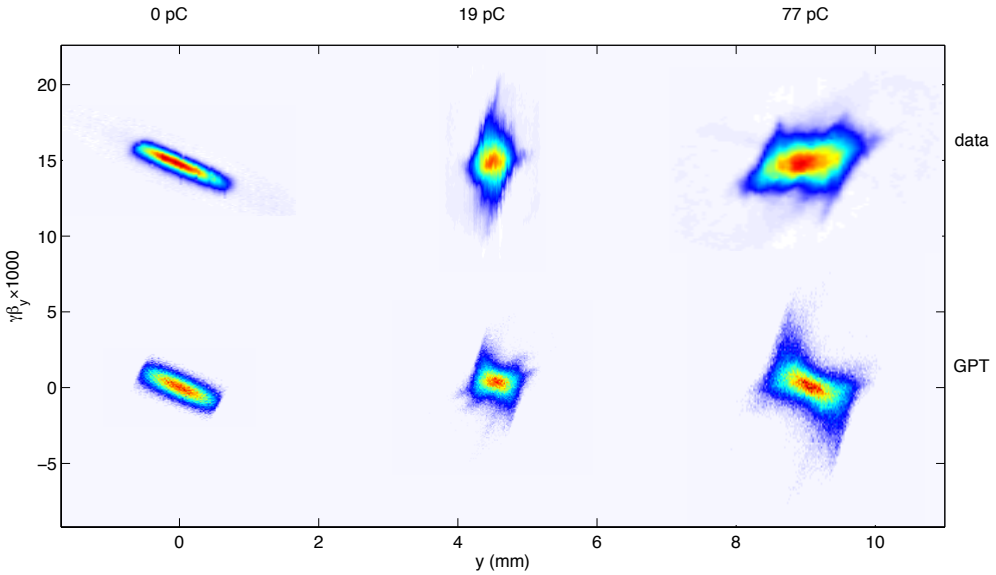

(b) Vertical phase-space as a function of bunch charge.

Figure 4.15: Comparison of the measured and simulated projected transverse phase-space as a function of bunch charge. Plot (a) shows the the horizontal phase-space, while (b) shows the vertical phase-space. Corresponding emittance values can be found in Table 4.3.

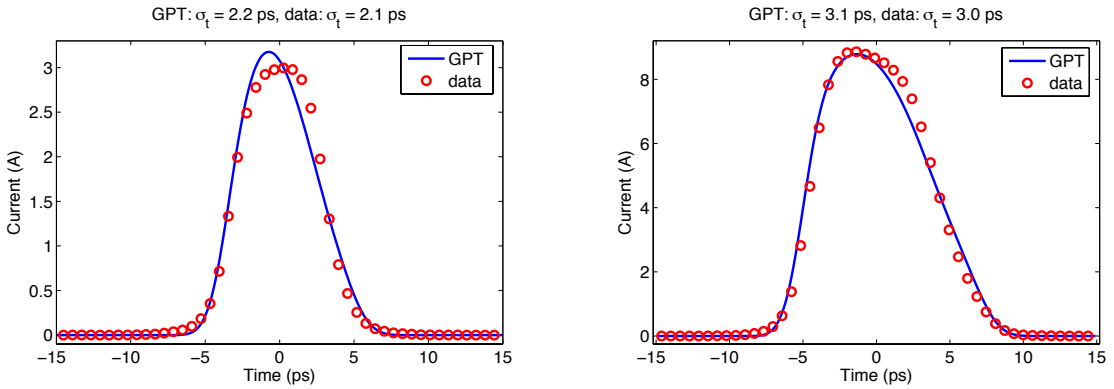

(a) Instantaneous current at 19 pC/bunch. (b) Instantaneous current at 77 pC/bunch.

Figure 4.16: Comparison of the measured beam current to GPT simulation. The estimated uncertainty in the rms bunch lengths was (a) ±0.1 ps and (b) ±0.2 ps.

rms bunch lengths for the 19 (77) pC per bunch settings were measured to be 2.1 ± 0.1 (3.0 ± 0.2) ps, respectively, while GPT gave bunch lengths of 2.2 (3.1) ps, respectively. The agreement between measurement and GPT was within 5% in both cases. As Fig. 4.16(a) shows, the qualitative agreement between data and simulation was good for the 19 pC/bunch measurement. The difference in the overall scaling between the measured and simulated data for this setting is due to the normalization of the data to the bunch charge. In the 77 pC/bunch case, the qualitative agreement between measurement and simulation, shown in Fig. 4.16(b), was excellent.

In addition to measuring the bunch length, the time-resolved emittance was measured both because it is of interest to FEL applications and to elucidate the character of the emittance growth in the merger. Fig. 4.17 shows the core and 90% emittance for both the 19 and 77 pC measurements. For the 19 pC data, both emittances are relatively constant over the bunch length. Similarly, for the 77 pC data, the core emittance is constant over the majority of the bunch length. Also important is the fact that the core emittance for this data is below the design specification for the injector. The time-resolved emittance

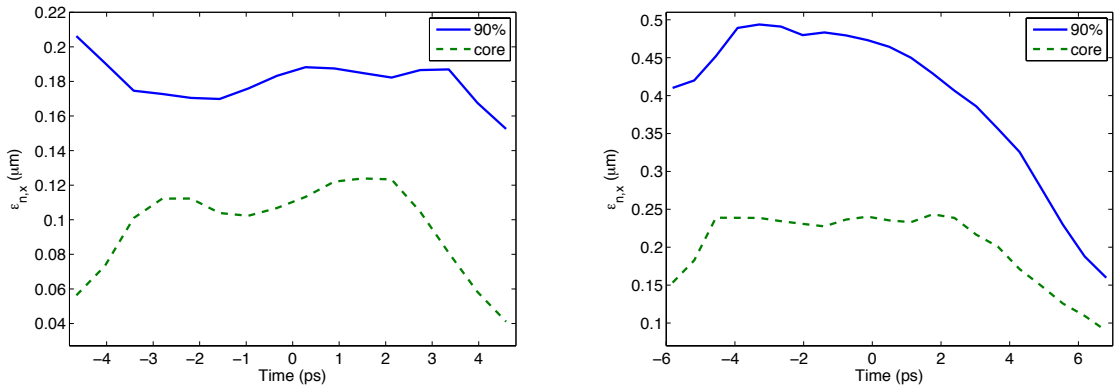

(a) 19 pC/bunch slice emittance data. (b) 77 pC/bunch slice emittance data.

Figure 4.17: The 90% and core slice emittance for: (a) 19 pC/bunch, (b) 77 pC/bunch.

measurements provide a very elegant way of viewing the resulting phase space distributions. Fig. 4.18 shows the three-dimensional representation of the time-resolved phase space for both data sets. The 3D representation demonstrates that the z-shaped features seen in the projected emittance in Fig. 4.15(a) are actually a real effect formed along the time axis.

The last quantity measured was the rms energy spread. To do so, the beam was sent through the A4 straight section, followed by a single dipole and viewscreen in the C2 section (see Fig. 4.1). Before entering the dipole, the beam was clipped by passing it through a crossed pair of emittance measurement slits. The emittance measurement scanner magnets in this section were set so that crossed slits selected out a beamlet from the centroid of the horizontal and vertical phase spaces. Table 4.4 shows the simulated and measured rms energy spread in the straight section, as well as simulated values in the B1 merger. The measured values were computed from the 1D dimensional energy spread distribution obtained on the viewscreen in the C2 section using a 10% threshold to remove background noise. The values are slightly smaller than simulation, which is likely due to the fact that we were only measuring the energy spread of a single transverse beamlet, while

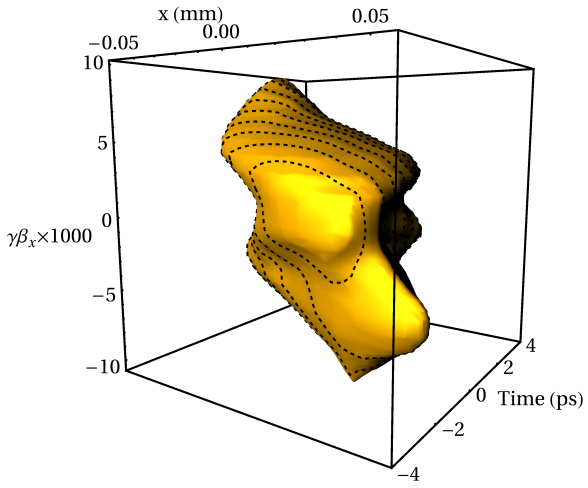

(a) 60% isosurface plot of the 19 pC data.

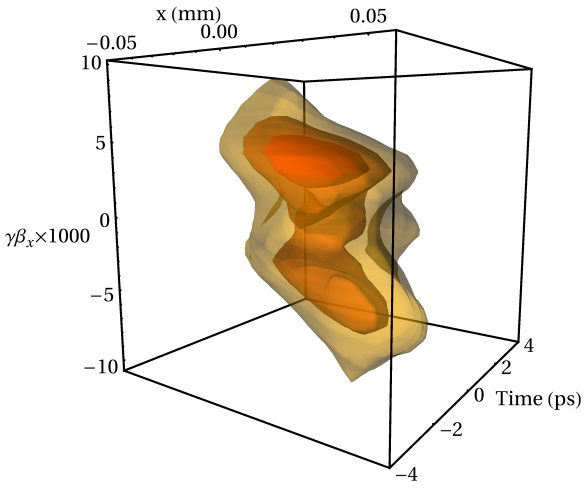

(b) 60% isosurface plot of 19 pC data showing inner isosurfaces.

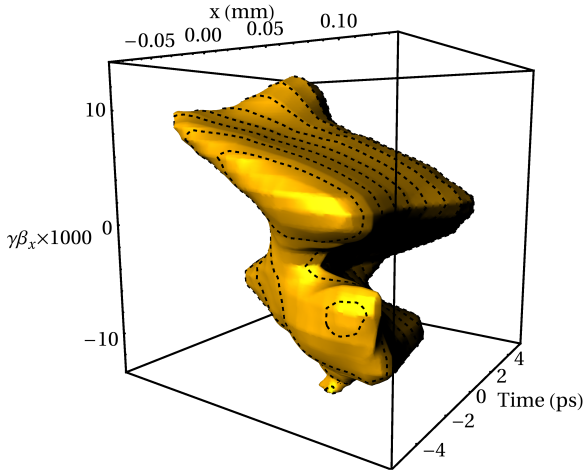

(c) 60% isosurface plot of the 77 pC data.

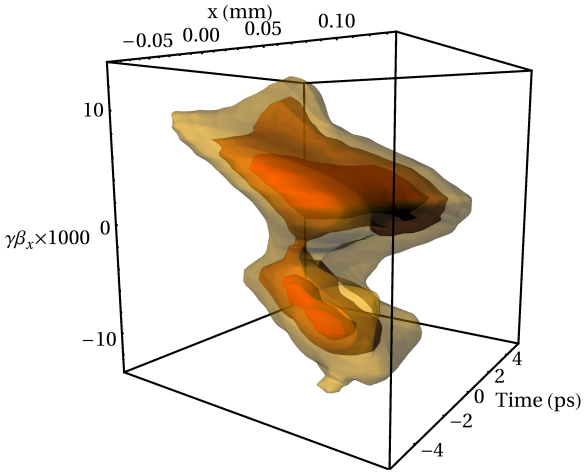

(d) 60% isosurface plot of 77 pC slice emittance data showing inner isosurfaces.

Figure 4.18: Time-resolved phase space data: (a) 60% isosurface plot of the 19 pC data, (b) 60% isosurface plot of 19 pC slice emittance data showing inner isosurfaces, (c) 60% Isosurface plot of the 77 pC time-resolved phase-space, and (d) 60% isosurface plot of 77 pC slice emittance data showing inner isosurfaces.

the simulated values are computed from the entire beam distribution. While we did not measure the energy spread directly in the merger section, the agreement found between measurement and simulation for emittance and bunch length lead us to conclude that the

Table 4.4: Simulated and measured rms energy spread as a function of bunch charge.

Data Type	GPT Simulation	Measurement
19 pC/bunch, A4 Section	0.16%	$0.14 \pm 0.01\%$
19 pC/bunch, B1 Section	0.12%	N/A
77 pC/bunch, A4 Section	0.27%	$0.26 \pm 0.01\%$
77 pC/bunch, B1 Section	0.21%	N/A

values measured in the straight section at least provide an upper bound on the energy spread in the merger, following the same trend found in the simulation data.

4.5 Conclusion and Discussions

A comprehensive model of the Cornell ERL injector has been constructed using the space charge code GPT. After verifying the accuracy of the GPT model against linear optics measurements in the injector, multi-objective optimizations of the model were carried out in order to find optics settings with which to measure low emittance after the merger section in the injector. In addition, a user interface between the GPT code, the optimizer solutions, and the injector was developed. This interface provided visualization of relevant simulation data in one-to-one correspondence with measured data, and allowed users to explore adjustments of the injector optics in simulation while in the control room, often in near real time with measurements. Using this interface, and starting from a single optimized setting of the injector model, optics sets for both 19 pC and 77 pC bunch charges were found which kept both the simulated rms beam sizes small throughout the injector, in addition to preserving the minimized emittance at the end of the merger section. These settings were then loaded into the injector, and the phase space data for each bunch charge was taken.

The resulting data sets include the vertical and horizontal projected phase spaces, as

well as the time-resolved horizontal phase space at the merger EMS, and the energy spread distribution in the A4 straight section. Overall, we found excellent agreement between measurement and simulation. For both bunch charges, the agreement between the measured projected 100 and 90% emittance values was within 30% of the simulated values in both transverse planes. We point out that for 77 pC/bunch, the measured 90% emittance in vertical plane, as well as the core emittance in both planes, meets the ERL design specification of $\epsilon_n \leq 0.3$ μm. The projected emittance in both transverse planes demonstrates the correct scaling with bunch charge shown in Eq. (4.1). Using the time-resolved horizontal phase data, the longitudinal bunch profile and time-resolved emittance were computed. The measured rms bunch length for both bunch charges was at or below the 3 ps specification, and agreed with simulation to within 5%. For both bunch charges, the time-resolved core emittance met the ERL specification. Finally, an estimation of the energy spread of the beam in merger was found by measuring the energy spread in the straight section. Agreement between the measured and simulated rms energy spread was within 13% for both bunch charges.

These results represent a significant advancement in high-brightness photoinjectors. The measured emittances in this work set a new record low for DC photoinjectors producing beams with comparable bunch charge. To put these results in a broader picture, it is instructive to compare the performance of the Cornell injector for its designed application of a 5 GeV x-ray ERL to the beam quality of existing storage rings. For this comparison, we assume a 100 mA, 1 nm-rad horizontal emittance storage ring with 10^{-3} energy spread and 1% coupling factor, representing the best of existing third generation light sources [15]. As a figure of merit for non-Gaussian beams, it is convenient to use the effective transverse average beam brightness over the rms energy spread of the beam at the location of an

undulator:

$$\left(I \cdot \frac{f_x \cdot f_y}{\epsilon_x(f_x) \cdot \epsilon_y(f_y)} \bigg|_{\text{core}} \right) \times \frac{1}{\sigma_\delta}. \tag{4.8}$$

Here ϵ_x and ϵ_y are the transverse geometric emittance values as a function of the horizontal and vertical beam fractions, respectively. The energy spread is included in this expression to reflect the fact that undulators with larger number of periods can be more efficiently utilized for beams with smaller energy spread. In an ERL, the energy spread after the main linac will be defined by the RF curvature and the bunch length according to $(2\pi f_{\text{rf}} \cdot \sigma_t)^2/\sqrt{2}$ [94]. Using our 19 pC/bunch data, and assuming the full repetition rate, the estimated energy spread and effective average brightness of a 1.3 GHz, 5 GeV ERL yields a higher transverse brightness over the best storage ring by a factor of 20.

Looking forward, we point out that the measurements shown here demonstrate two crucial points: (i) that low emittances reported previously in simulations [34, 74] are well within the reach of the next planned iteration of the photoinjector; and (ii) the relevant physics and control parameters required to produce these low emittances are now understood. In developing a plan for reducing the emittance further, we note that optimization results indicate that lower emittances and shorter bunch lengths at the end of the merger are possible at higher beam energies [85]. As a result, the optimal photoinjector for a future ERL light source will operate at higher beam energies (roughly 12 MeV) than those used in this work [19]. Eq. (4.1) shows two more directions for further improvement. For a given bunch charge, the emittance in this equation can be reduced by lowering photocathode MTE, or by increasing the accelerating field at the cathode. In fact, the results for the vertical emittance demonstrate that the emittance in this plane is dominated by the thermal emittance, and thus colder cathodes are required. Currently, there is an active cathode research program at Cornell University dedicated to improving cathode performance [95]. Already, cathodes with MTE values as low as 30 meV have been

experimentally realized both for negative affinity and multi-alkali photocathodes [96]. In parallel, Cornell is developing an improved DC gun, in order to overcome the current voltage limitation. The new gun design features a segmented insulator with guard rings [97] in order to minimize damaging the insulator from field emission. Lastly, improved laser shaping will aid in creating bunches with more linear space charge fields. According to the rough scaling law in Eq. (4.1), as well as more detailed calculations reported in [19, 34], these improvements are expected to reduce the emittance in the photoinjector by roughly a factor of 3, resulting in a beam brightness roughly 10 times higher than reported here. This ability to independently improve critical elements in the injector, resulting in better performance, is one of the major strengths of a linac based accelerator.

APPENDIX A

Emittance Definitions

Here we provide the relevant emittance definitions used in this work to describe non-Gaussian phase space distributions. We use the standard definition of the normalized transverse rms emittance:

$$\epsilon_n = \frac{1}{mc}\sqrt{\langle x^2\rangle\langle p_x^2\rangle - \langle xp_x\rangle^2} = \sqrt{\langle x^2\rangle\langle \gamma^2\beta_x^2\rangle - \langle x\cdot\gamma\beta_x\rangle^2}, \tag{A.1}$$

where γ and β_x are the normalized energy and transverse velocity of each electron. In this and all following expression the subscript "n" is used to distinguished between the normalized emittance ϵ_n and geometric emittance ϵ, which are related by $\epsilon_n = (\gamma\beta)\cdot\epsilon$. In this and all subsequent expressions, $\langle u\rangle$ denotes the average over the particle distribution in phase space: $\langle u\rangle = \iint u(x,p_x)\rho(x,p_x)\mathrm{d}x\mathrm{d}p_x$, where $\rho(x,p_x)$ is the normalized 2D phase space distribution function. The rms emittance as a function of beam fraction is defined as follows [98]. For an area in phase space πa, an ellipse with Twiss parameters given by

$$T = \begin{pmatrix} \beta_n & -\alpha_n \\ -\alpha_n & \gamma_n \end{pmatrix},$$

is defined so that the phase space region enclosed by the ellipse is given by $d(a,T) = \left\{\mathbf{x} : \mathbf{x}^T T^{-1}\mathbf{x} \le a\right\}$, where $\mathbf{x} = (x,p_x)^{\mathrm{T}}$. The twiss parameters in T are varied until the fraction of particles enclosed in the ellipse is maximized. Labeling this phase space region $D(a)$, the beam fraction is defined as:

$$f(a) = \max\left\{\iint_{d(a,T)} \rho(x,p_x)\mathrm{d}x\mathrm{d}p_x\right\} = \iint_{D(a)} \rho(x,p_x)\mathrm{d}x\mathrm{d}p_x. \tag{A.2}$$

The corresponding fractional emittance takes the form

$$\epsilon_n(a) = \frac{1}{mc}\sqrt{\langle x^2\rangle_D \langle p_x^2\rangle_D - \langle x p_x\rangle_D^2}, \tag{A.3}$$

where $\langle u\rangle_D = \frac{1}{f(a)}\iint_{D(a)} u\rho(x,p_x)\mathrm{d}x\mathrm{d}p_x$. The parametric curve defined by $\{f(a),\ \epsilon_n(a)\}$ is the emittance vs. fraction curve $\epsilon_n(f)$. Also important for understanding emittances of non-Gaussian beams are the definitions of the core emittance and corresponding core fraction [27, 98]:

$$\epsilon_n(\text{core}) = \left.\frac{d\epsilon_n}{df}\right|_{f\to 0}, \quad f_{\text{core}} : \epsilon_n(f_{\text{core}}) = \epsilon_n(\text{core}). \tag{A.4}$$

For comparison purposes, the emittance vs. fraction curve for 2D uniform, elliptical, and Gaussian distributions have been computed. To do so the correlation between x and p_x has been removed and the coordinates rescaled so that the distributions can be written as radial functions of the normalized coordinate $\hat{r} = \sqrt{\hat{x}^2 + \hat{p}_x^2}$. Additionally, the distributions are parameterized so that the resulting emittance vs. fraction curve $\hat{\epsilon}_n(f)$ is normalized: $\hat{\epsilon}_n(f=1) = 1$. Fig A.1(a) shows each of the three distributions as a function of the normalized radial coordinate. The corresponding emittance vs. fraction curves are shown in Fig. A.1(b). From these curves the 90% and core emittance (relative to the 100% emittance) can be computed. Table A.1 gives these ratios, as well as the core fraction, for each distribution. For additional discussion on the connection between core emittance and brightness, see [98].

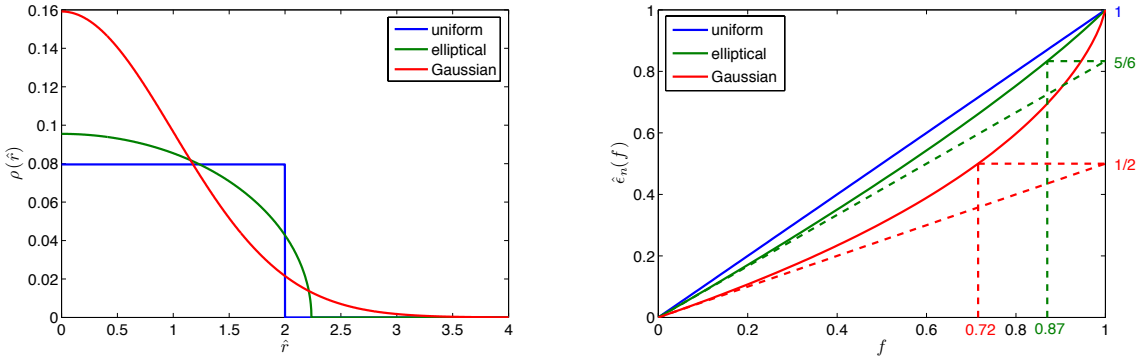

(a) Transverse phase-space distributions.

(b) Emittance verses fraction curves.

Figure A.1: Example transverse phase space distributions as a function of the normalized coordinates $\hat{r}^2 = \hat{x}^2 + \hat{p}_x^2$ (a), and the corresponding emittance vs. fraction curves (b). Dashed lines indicate core emittance and core fraction values.

Table A.1: The scaled emittance and fraction data for various phase-space distributions.

Distribution Type	$\hat{\epsilon}_n(90\%)$	$\hat{\epsilon}_n(\text{core})$	f_{core}	$\hat{\epsilon}_n(\text{core})/f_{\text{core}}$
uniform	0.90	1	100%	1
elliptical	0.87	5/6	87%	0.96
Gaussian	0.74	1/2	72%	0.69

APPENDIX B

Phase Space Noise Subtraction

It is well known that a density distribution with a nonzero noise offset leads to significantly higher second moments. All of the raw measured phase spaces in Chapter §4 had such a background, and subsequently, several procedures had to be developed before the second moments and emittance could be reliably extracted from the data. The analysis procedures used are split into two cases: projected phase space measurements and time-resolved (horizontal) phase space measurements.

B.1 Projected Phase Space Distributions

Performing a projected phase measurement yields the 2D transverse distribution function $\rho = \rho(x, P)$, where $P = p_x/mc = \gamma\beta_x$. An example phase space is shown in Fig. B.1(a). It is clear from this image that both a constant noise offset and sinusoidal feature along the x-axis are present. This sinusoidal variation is attributed to 60 Hz noise in the measurement system. Before removing these backgrounds, a 2D interpolation of the distribution function was done in order to use the scanner magnet current read-backs (as opposed to the command values) used to perform the phase space measurements. This was done with the *gridfit* Matlab package [99].

After this, the 60 Hz effect was removed in a four step process described below:

1. Select the 1D distribution function $\rho_i(P) = \rho(x = x_i, P)$ for the i^{th} value along the x-axis.

2. Define the noise region along this column of data using a user specified threshold T (typically 3%): $R_{\text{noise}}(P) = \{P : \rho_i(P) < T \cdot \max[\rho_i(P)]\}$.

3. Compute the average noise value for this region: $\bar{N}_i = \frac{1}{\Delta P} \int_{R_{\text{noise}}(P)} \rho_i(P) \mathrm{d}P$.

4. Subtract the noise from the initial distribution: $\rho(x_i, P) = \rho_0(x_i, P) - \bar{N}_i$.

Having removed any possible 60 Hz distortions along the x-axis, the remaining background offset is subtracted out using a method based on the SCUBEEx algorithm [93]. This outline of this algorithm used in this work is given below:

1. An initial estimate of the background noise is made using the outer 5% of the phase space data area: $R_{\text{noise}}(x, P) = \{(x, P) : (x, P) \leq 1.05 \cdot (x_{\min}, P_{\min}) \bigcup (x, P) \geq 0.95 \cdot (x_{\max}, P_{\max})\}$.

2. Compute the average noise: $\bar{N} = \iint_{R(x,p)} \rho(x, P) \mathrm{d}P / \iint_{R(x,p)} \mathrm{d}P$.

3. Subtract the noise from the distribution: $\rho(x, P) = \rho_0(x, P) - \bar{N}$, and use this to compute the Σ matrix and emittance:

$$\Sigma = \begin{pmatrix} \langle x^2 \rangle & \langle xP \rangle \\ \langle xP \rangle & \langle P^2 \rangle \end{pmatrix}, \quad \epsilon_{n,x} = \sqrt{\det[\Sigma]}.$$

4. Compute the corresponding Twiss matrix $T = \Sigma / \epsilon_{n,x}$, and define the noise region as $R_{\text{noise}} = \{(x, P) : (x, P) T^{-1} (x, P)^T \geq N \epsilon_{n,x}^2$. This correspondes to defining the noise as lying outside $N\sigma$ of a Gaussian distribution. Typically $N = 5$.

5. Repeat 2-4 for a desired number of times (typically 5).

The subtraction of background offset was calibrated against thermal emittance measurements taken using a solenoid scan in the A1 emittance compensation section. Fig. B.1 shows how the removal of the 60 Hz noise lead more consistent results. The top row of the figure shows how the 60 Hz noise subtraction reduced the emittance substantially when the signal to noise ratio was relatively lower. In this case the 60 Hz noise subtraction reduced the emittance from 0.92 μm to 0.73 μm. The bottom row of the figure shows the same phase space measured with better signal to noise. In this case the emittance was hardly changed. The results both give emittances around 0.7 μm.

B.2 Time-resolved Phase Space Distributions

A detailed description of the time-resolved measurement process is given in [35]. For every current setting of the two EMS scanners, a snapshot of the beamlet passed through the EMS system with the deflector on is taken on a downstream viewscreen. The distribution describes a time resolved phase space. Noise subtraction in this case must be performed on each snapshot. Note that the vertical axis in each snapshot, labeled y, is a dummy variable, and is eventually integrated out. The noise subtraction process for each snapshot is detailed below:

1. Load the intensisty profile (snapshot) and only save data within a rectangular region of interest supplied by the user.

2. Apply an upper threshold T_H to define the initial noise region: $R_{\text{noise},H}(t,y) = \{(t,y) : \rho(t,y) < T_H \cdot \max[\rho(t,y)]\}$.

3. Grow the boundary of this region using a simple convolution function which smears

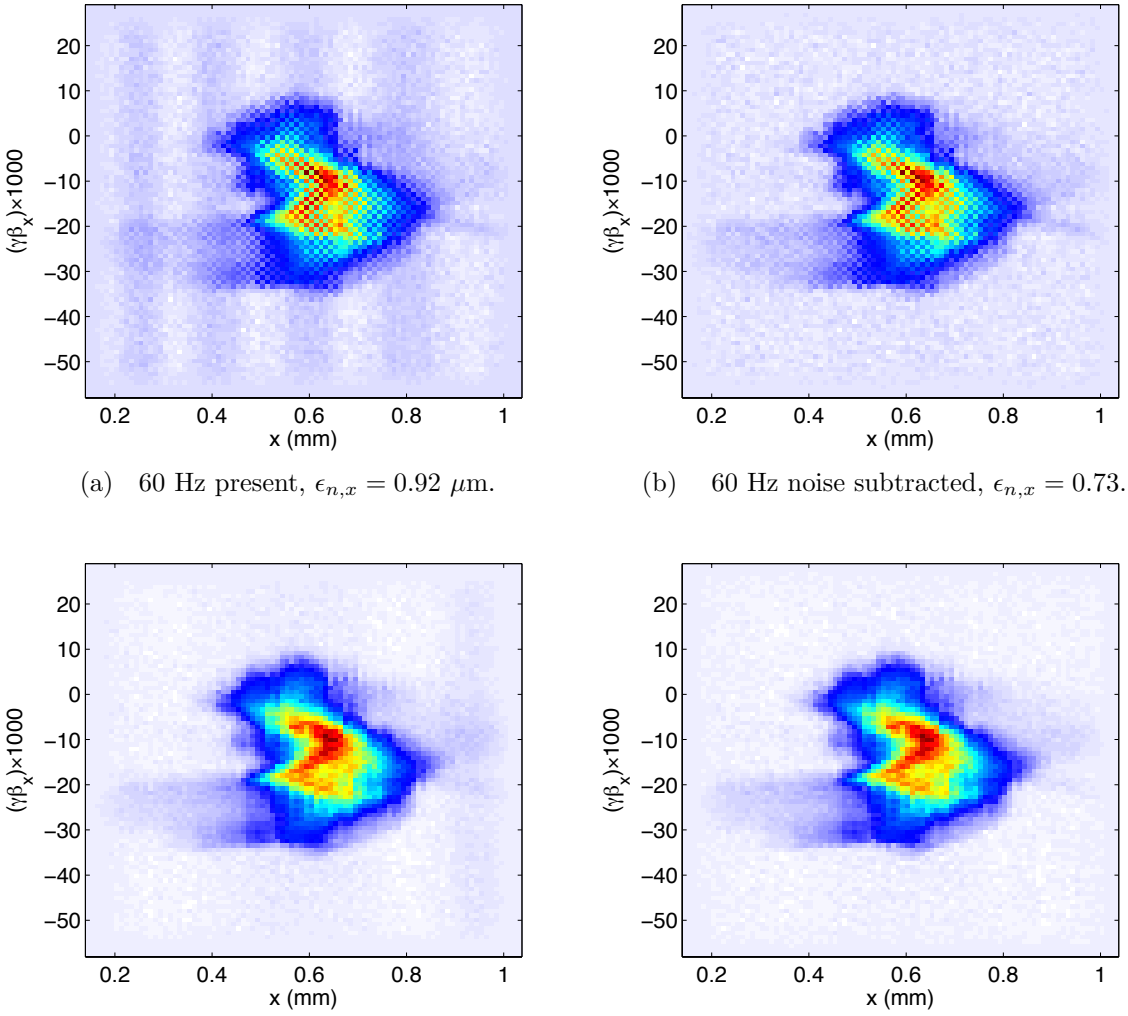

(a) 60 Hz present, $\epsilon_{n,x} = 0.92$ μm.

(b) 60 Hz noise subtracted, $\epsilon_{n,x} = 0.73$.

(c) Same as (a), but better signal to noise, $\epsilon_{n,x} = 0.7$ μm.

(d) 60 Hz noise subtracted, $\epsilon_{n,x} = 0.69$ μm.

Figure B.1: Comparison of two phase space measurements before and after 60 Hz noise removal.

out the boundary by several phase space pixels. The boundary is grown until a lower threshold T_L is reached: $R_{\text{noise},L} = \{(t, y) : \rho(t, y) < T_L \cdot \max[\rho(t, y)]\}$.

4. Compute the average noise outside of the data region: $\bar{N} = \iint_{R(x,p)} \rho(x, P)\mathrm{d}P / \iint_{R(x,p)} \mathrm{d}P$.

5. Subtract the average noise from the distribution data: $\rho = \rho_0 - \bar{N}$.

The snapshot is then used in computing the time-resolved phase space as described in [35]. This method was calibrated against both the projected noise subtraction algorithm and a measurement of the thermal emittance in the machine using a solenoid scan.

References

1. D. Iwanenko and I. Pomeranchuk, "On the maximal energy attainable in a betatron," *Phys. Rev.* **65** (Jun, 1944) 343–343. http://link.aps.org/doi/10.1103/PhysRev.65.343. 1
2. F. R. Elder, R. V. Languir, and H. C. Pollock, "Radiation from electrons accelerated in a synchrotron," *Phys. Rev.* **74** no. 1, (July, 1948) 52–56. 1
3. J. P. Blewett, "Synchrotron radiation - early history," *J. Synchrotron Rad.* **5** (1998) 135–139. 1
4. G. A. Schott, *Electromagnetic Radiation*. Cambridge University Press., 1912. 1
5. D. H. Tomboulian and P. L. Hartman, "Spectral and angular distribution of ultraviolet radiation from the 300-mev cornell synchrotron," *Phys. Rev.* **102** (Jun, 1956) 1423–1447. http://link.aps.org/doi/10.1103/PhysRev.102.1423. 1
6. J. P. Blewett, "Radiation losses in induction electron accelerators," *Phys. Rev.* **69** no. 3 and 4, (February, 1946) 87–95. 2
7. J. Schwinger, "On the classical radiation of accelerated electrons," *Phys. Rev.* **75** (Jun, 1949) 1912–1925. http://link.aps.org/doi/10.1103/PhysRev.75.1912. 2
8. J. D. Jackson, *Classical Electrodynamics*. John Wiley and Sons, Inc., 2nd ed., 1975.
9. A. Hofmann, *The Physics of Synchrotron Radiation*. Cambridge University Press., July, 2004. 2, 5
10. H. Winick, "Fourth generation light sources," SLAC-PUB 7525, Stanford Linear Accelerator Center, Stanford Universtiy, May, 1997. 3, 4, 6
11. G. N. Kulipanov, "Ginzburg's invention of undulators and their role in modern synchrotron radiation sources and free electron lasers," *Physics-Uspekhi* **50** no. 4, (2007) 368. http://stacks.iop.org/1063-7869/50/i=4/a=R06. 3
12. http://www.esrf.eu/Accelerators/news/art-undulator, 2013. http://www.esrf.eu/Accelerators/news/art-undulator. 4
13. http://xdb.lbl.gov/, 2009. http://xdb.lbl.gov/. 5
14. A. Chao and W. Chou, eds., *Reviews of Accelerator Science and Technology*, vol. 1. World Scientific Publishing Co. Pte. Ltd., Singapore, 2008. 5, 6
15. https://photon-science.desy.de/facilities/petra_iii/machine/parameters/index_eng.html, 2013. https://photon-science.desy.de/facilities/petra_iii/machine/parameters/index_eng.html. 6, 115
16. AmannJ., BergW., BlankV., D. J., DingY., EmmaP., FengY., FrischJ., FritzD., HastingsJ., HuangZ., KrzywinskiJ., LindbergR., LoosH., LutmanA., N. D., RatnerD., RzepielaJ., ShuD., Shvyd'koYu., SpampinatiS., StoupinS., TerentyevS., TrakhtenbergE., WalzD., WelchJ., WuJ., ZholentsA., and ZhuD., "Demonstration of self-seeding in a

hard-x-ray free-electron laser," *Nat Photon* **6** no. 10, (10, 2012) 693–698. http://dx.doi.org/10.1038/nphoton.2012.180. 7

17. D. Pile, "X-rays: First light from sacla," *Nat Photon* **5** no. 8, (08, 2011) 456–457. http://dx.doi.org/10.1038/nphoton.2011.178.

18. H. H. Braun, "The future of x-ray fels," in *Proceedings of IPAC2012*, no. FRYAP01. 2012. 7

19. I. V. Bazarov, S. A. Belomestnykh, D. H. Bilderback, M. G. Billing, J. D. Brock, B. W. Buckley, S. S. Chapman, E. P. Chojnacki, Z. A. Conway, J. A. Crittenden, D. Dale, J. A. Dobbins, B. M. Dunham, R. D. Ehrlich, M. P. Ehrlichman, K. D. Finkelstein, E. Fontes, M. J. Forster, S. W. Gray, S. Greenwald, S. M. Gruner, C. Gulliford, D. L. Hartill, R. G. Helmke, G. H. Hoffstaetter, A. Kazimirov, R. P. Kaplan, S. S. Karkare, V. O. Kostroun, F. A. Laham, Y. H. Lau, Y. Li, X. Liu, M. U. Liepe, F. Loehl, L. Cultrera, T. Miyajima, C. E. Mayes, J. M. Maxson, A. Meseck, A. A. Mikhailichenko, D. Ouzounov, H. S. Padamsee, S. B. Peck, M. A. Pfeifer, S. E. Posen, P. G. Quigley, P. Revesz, D. H. Rice, U. Sae-Ueng, D. C. Sagan, J. O. Sears, V. D. Shemelin, C. K. Sinclair, D. M. Smilgies, E. N. Smith, K. W. Smolenski, C. Spethmann, C. Song, T. Tanabe, A. B. Temnykh, M. Tigner, N. R. A. Valles, V. G. Veshcherevich, Z. Wang, A. R. Woll, Y. Xie, and Z. Zhao, "Cornell energy recovery linac project definition design report," tech. rep., Cornell University, September, 2012. 8, 10, 78, 116, 117

20. M. Tigner, "A possible apparatus for electron clashing-beam experiements," *Nuovo Cimento* **37** (1965) 1228–1231. 8

21. IPAC2012, ed., *Review of ERL Projects at KEK and Around the World*, no. TUXB02. Proceedings of IPAC2012, New Orleans, Louisiana, USA, 2012. 10

22. W. Coene, G. Janssen, M. Op de Beeck, and D. Van Dyck, "Phase retrieval through focus variation for ultra-resolution in field-emission transmission electron microscopy," *Phys. Rev. Lett.* **69** (Dec, 1992) 3743–3746. http://link.aps.org/doi/10.1103/PhysRevLett.69.3743. 12

23. M. E. Read, G. Miram, R. Ives, V. Ivanov, and A. Krasnykh, "A gridded electron gun for a sheet beam klystron," SLAC-PUB 13205, Stanford Linear Accelerator Center.

24. P. Kung, H.-c. Lihn, H. Wiedemann, and D. Bocek, "Generation and measurement of 50-fs (rms) electron pulses," *Phys. Rev. Lett.* **73** (Aug, 1994) 967–970. http://link.aps.org/doi/10.1103/PhysRevLett.73.967.

25. P. of the 1992 Linear Accelerator Conference, ed., *Generation of Multi-bunch Beam with Thermionic Gun for the Japan Linear Collider*. Ottawa, Ontario, Canada, 1992. 12

26. B. Dunham, J. Barley, A. Bartnik, I. Bazarov, L. Cultrera, J. Dobbins, G. Hoffstaetter, B. Johnson, R. Kaplan, S. Karkare, V. Kostroun, Y. Li, M. Liepe, X. Liu, F. Loehl, J. Maxson, P. Quigley, J. Reilly, D. Rice, D. Sabol, E. Smith, K. Smolenski, M. Tigner, V. Vesherevich, D. Widger, and Z. Zhao, "Record high-average current from a high-brightness photoinjector," *Applied Physics Letters* **102** no. 3, (2013) 034105.

http://link.aip.org/link/?APL/102/034105/1. 12, 17, 20, 21, 79, 81, 83, 96

27. I. V. Bazarov, B. M. Dunham, and C. K. Sinclair, "Maximum achievable beam brightness from photoinjectors," *Phys. Rev. Lett.* **102** (Mar, 2009) 104801. http://link.aps.org/doi/10.1103/PhysRevLett.102.104801. 12, 80, 119

28. M. Reiser, *Theory and Design of Charge Particle Beams*. WILEY-VCH Verlag GmbH and Co. KGaA, 2008. 12, 13, 14, 28

29. B. E. Carlsten, "Nuclear instruments and methods in physics research uclear instruments and methods in physics research uclear instruments and methods in physics research uclear instruments and methods in physics research new photoelectric injector design for the los alamos national laboratory xuv fel accelerator," *Nuclear Instruments and Methods in Physics Research* **A** (1989) 313–319. 16, 80

30. L. Serafini and J. B. Rosenzweig, "Envelope analysis of intense relativistic quasilaminar beams in rf photoinjectors:ma theory of emittance compensation," *Phys. Rev. E* **55** (Jun, 1997) 7565–7590. http://link.aps.org/doi/10.1103/PhysRevE.55.7565. 16, 80

31. K.-J. Kim, "Rf and space-charge effects in laser-driven rf electron guns," *Nuclear Instruments and Methods in Physics Research Section A: Accelerators, Spectrometers, Detectors and Associated Equipment* **275** no. 2, (1989) 201 – 218. http://www.sciencedirect.com/science/article/pii/0168900289906888. 31, 65, 80

32. I. V. Bazarov, B. M. Dunham, C. Gulliford, Y. Li, X. Liu, C. K. Sinclair, K. Soong, and F. Hannon, "Benchmarking of 3d space charge codes using direct phase space measurements from photoemission high voltage dc gun," *Phys. Rev. ST Accel. Beams* **11** (Oct, 2008) 100703. http://link.aps.org/doi/10.1103/PhysRevSTAB.11.100703. 12, 81, 83, 84, 95, 106

33. J. Rees, "Symplecticity in beam dynamics: An introduction," SLAC-PUB 9939, Stanford Linear Accelerator Center. 13

34. I. V. Bazarov, A. Kim, M. N. Lakshmanan, and J. M. Maxson, "Comparison of dc and superconducting rf photoemission guns for high brightness high average current beam production," *Phys. Rev. ST Accel. Beams* **14** (Jul, 2011) 072001. http://link.aps.org/doi/10.1103/PhysRevSTAB.14.072001. 15, 17, 19, 79, 80, 95, 101, 116, 117

35. H. Li, *Mutli-dimensional Characterization of the Laser and Electron Beams of the Cornell Energy Recovery Linac Photoinjector Prototype*. PhD thesis, Cornell University, August, 2012. 15, 81, 83, 84, 88, 95, 123, 125

36. J. Fraser, R. Sheffield, and E. Gray, "A new high-brightness electron injector for free electron lasers driven by {RF} linacs," *Nuclear Instruments and Methods in Physics Research Section A: Accelerators, Spectrometers, Detectors and Associated Equipment* **250** no. 12, (1986) 71 – 76.

http://www.sciencedirect.com/science/article/pii/0168900286908624. 17

37. R. Akre, D. Dowell, P. Emma, J. Frisch, S. Gilevich, G. Hays, P. Hering, R. Iverson, C. Limborg-Deprey, H. Loos, A. Miahnahri, J. Schmerge, J. Turner, J. Welch, W. White, and J. Wu, "Commissioning the linac coherent light source injector," *Phys. Rev. ST Accel. Beams* **11** (Mar, 2008) 030703. http://link.aps.org/doi/10.1103/PhysRevSTAB.11.030703. 17, 79

38. D. H. Dowell, J. W. Lewellen, D. Nguyen, and R. Rimmer, "The status of normal conducting rf (ncrf) guns, a summary of the erl2005 workshop," *Nuclear Instruments and Methods in Physics Research Section A: Accelerators, Spectrometers, Detectors and Associated Equipment* **557** no. 1, (2006) 61 – 68. http://www.sciencedirect.com/science/article/pii/S0168900205019741. 17, 18, 19, 79

39. D. H. Dowell, K. J. Davis, K. D. Friddell, E. L. Tyson, C. A. Lancaster, L. Milliman, R. E. Rodenburg, T. Aas, M. Bemes, S. Z. Bethel, P. E. Johnson, K. Murphy, C. Whelen, G. E. Busch, and D. K. Remelius, "First operation of a photocathode radio frequency gun injector at high duty factor," *Applied Physics Letters* **63** no. 15, (1993) 2035–2037. http://link.aip.org/link/?APL/63/2035/1. 17, 18

40. F. Sannibale, D. Filippetto, C. F. Papadopoulos, J. Staples, R. Wells, B. Bailey, K. Baptiste, J. Corlett, C. Cork, S. De Santis, S. Dimaggio, L. Doolittle, J. Doyle, J. Feng, D. Garcia Quintas, G. Huang, H. Huang, T. Kramasz, S. Kwiatkowski, R. Lellinger, V. Moroz, W. E. Norum, H. Padmore, C. Pappas, G. Portmann, T. Vecchione, M. Vinco, M. Zolotorev, and F. Zucca, "Advanced photoinjector experiment photogun commissioning results," *Phys. Rev. ST Accel. Beams* **15** (Oct, 2012) 103501. http://link.aps.org/doi/10.1103/PhysRevSTAB.15.103501. 19

41. C. Gulliford, A. Bartnik, I. Bazarov, L. Cultrera, J. Dobbins, B. Dunham, F. Gonzalez, S. Karkare, H. Lee, H. Li, Y. Li, X. Liu, J. Maxson, C. Nguyen, K. Smolenski, and Z. Zhao, "Demonstration of low emittance in the cornell energy recovery linac injector prototype," *Phys. Rev. ST Accel. Beams* **16** (Jul, 2013) 073401. http://link.aps.org/doi/10.1103/PhysRevSTAB.16.073401. 21, 77

42. A. Arnold and J. Teichert, "Overview on superconducting photoinjectors," *Phys. Rev. ST Accel. Beams* **14** (Feb, 2011) 024801. http://link.aps.org/doi/10.1103/PhysRevSTAB.14.024801. 21, 22, 79

43. C. Gulliford and I. Bazarov, "New method for generating linear transfer matrices through combined rf and solenoid fields," *Phys. Rev. ST Accel. Beams* **15** (Feb, 2012) 024002. http://link.aps.org/doi/10.1103/PhysRevSTAB.15.024002. 24, 97

44. R. Brinkmann, Y. Derbenev, and K. Flöttmann, "A low emittance, flat-beam electron source for linear colliders," *Phys. Rev. ST Accel. Beams* **4** (May, 2001) 053501. http://link.aps.org/doi/10.1103/PhysRevSTAB.4.053501. 25

45. K.-J. Kim, "Round-to-flat transformation of angular-momentum-dominated beams," *Phys. Rev. ST Accel. Beams* **6** (Oct, 2003) 104002.

http://link.aps.org/doi/10.1103/PhysRevSTAB.6.104002. 25

46. I. Bazarov, L. Cultrera, A. Bartnik, B. Dunham, S. Karkare, Y. Li, X. Liu, J. Maxson, and W. Roussel, "Thermal emittance measurements of a cesium potassium antimonide photocathode," *Applied Physics Letters* **98** no. 22, (2011) 224101. http://link.aip.org/link/?APL/98/224101/1. 25, 31, 39

47. J. Rosenzweig and L. Serafini, "Transverse particle motion in radio-frequency linear accelerators," *Phys. Rev. E* **49** (Feb, 1994) 1599–1602. http://link.aps.org/doi/10.1103/PhysRevE.49.1599. 25, 32, 64

48. C. Wang and A. Chao, "Transfer matrices of superimposed magnest and rf cavities," Tech. Rep. 106, SLAP/AP, 1996. 25

49. D. T. Abell, "Numerical computation of high-order transfer maps for rf cavities," *Phys. Rev. ST Accel. Beams* **9** (May, 2006) 052001. http://link.aps.org/doi/10.1103/PhysRevSTAB.9.052001. 25

50. Y. Eidelman, N. Mokhov, S. Nagaitsev, and N. Solyak, "A new approach to calculate the transport matrix in rf cavities," in *Proceedings of 2011 Particle Accelerator Conference*, no. WEP131, PAC'11. New York, NY, USA, 2011. 26

51. P. Lapostolle and M. Weiss, "Formulae and procedures useful for the design of linear accelerators." CERN-PS-2000-001 (DR), January, 2000. 26

52. E. Tanke, S. Valero, and P. Lapostolle, "Dynac: A multi-particle beam dynamics code for leptons and hadrons in complex accelerating elements," in *Proc. of LINAC 2002*, LINAC2002. LINAC2002, Gyeongju, Korea, 2002. 26

53. L. Schachinger and R. Talman, "Teapot: A thin-element accelerator program for optics and tracking," *Particle Accelerators* **22** (1987) 35–56. 26, 47, 64

54. C. Gulliford, I. Bazarov, S. Belomestnykh, and V. Shemelin, "Asymmetric focusing study from twin input power couplers using realistic rf cavity field maps," *Phys. Rev. ST Accel. Beams* **14** (Mar, 2011) 032002. http://link.aps.org/doi/10.1103/PhysRevSTAB.14.032002. 26, 44, 45, 88, 89, 94, 96

55. J. D. Lawson, *The Physics of Charged Particle Beams*. No. 24-27. Oxford University Press, 1977. 28, 29, 35

56. C.-x. Wang, "Hamiltonian analysis of transverse beam dynamics in high-brightness photoinjectors," *Phys. Rev. E* **74** (Oct, 2006) 046502. http://link.aps.org/doi/10.1103/PhysRevE.74.046502. 31, 32, 35

57. M. Dohlus and S. Wipf, "Numerical investigations of waveguide input couplers for the tesla superstructure," in *7th European Particle Accelerator Conference*. Vienna, Austia, June, 2000. 46, 54

58. M. Dohlus, I. Zagorodnov, E. Gjonaj, and T. Weiland, "Coupler kick for very short bunches and its compensation," in *11th European Particle Accelerator Conference*,

EPAC08. Genoa, Italy, June, 2008. 62

59. N. Juntong, C. Beard, G. Burt, R. Jones, and I. Shinton, "Rf coupler kicks and wake-fields in sc accerelating cavities," in *Proc. 11th European Particle Accelerator Conference*, EPAC08. Genoa, Italy, 2008. 46, 54

60. G. Wu, H. Wang, C. E. Reece, and R. A. Rimmer, "JLAB internal report," tech. rep., Jefferson National Laboratory, 2007. 46

61. S. Belomestnykh, M. Liepe, H. Padamsee, V. Shemelin, and V. Veshcherevich, "High average power fundamental input couplers for the cornell university ERL: Requirements, design challenges and first ideas," ERL Internal Report 02-08, Cornell University, 2008. 46, 48, 54, 83

62. Z. Greenwald and D. Rubin, "Emittance Growth Study Using 3DE Code for the ERL Injector Cavities with Various Coupler Configurations," LNS Internal Report ERL 03-09, Cornell University, 2009.

63. B. Buckley and G. H. Hoffstaetter, "Transverse emittance dilution due to coupler kicks in linear accelerators," *Phys. Rev. ST Accel. Beams* **10** (Nov, 2007) 111002. http://link.aps.org/doi/10.1103/PhysRevSTAB.10.111002. 59, 61, 83

64. V. Shemelin, S. Belomestnykh, , and H. Padamsee, "Low-kick twin-coxial and waveguide-coaxial couplers for erl," LNS Internal Report SRF 021028-08, Cornell University, 2008. 46, 54, 83

65. http://www.cst.com/Content/Products/MWS/Overview.aspx. 48, 87

66. P. B. Wilson, "High Energy Electron Linacs: Applications to Storage Ring RF Systems and Linear Colliders," tech. rep., SLAC, November, 1991. 51, 52, 53

67. P. Balleyguier, "A straightforward method for cavity external q computation," *Particle Accelerators* **57** (1997) 113–127. 51, 56, 61

68. T. Wangler, *RF Linear Accelerators*. WILELY-VCH, 2008. 51

69. P. Balleyguier, "External q studies for apt sc-cavity couplers," 19th International Linear Accelerator Conference. Chicago, IL, USA, August, 1998. 61

70. Hairer, Lubich, and Wanner, *Geometric Numerical Integration: Structure-Preserving Algorithms for Ordinary Differential Equations, Second Edition"*. Springer, 2006. 64

71. G. R. Neil, C. L. Bohn, S. V. Benson, G. Biallas, D. Douglas, H. F. Dylla, R. Evans, J. Fugitt, A. Grippo, J. Gubeli, R. Hill, K. Jordan, R. Li, L. Merminga, P. Piot, J. Preble, M. Shinn, T. Siggins, R. Walker, and B. Yunn, "Sustained kilowatt lasing in a free-electron laser with same-cell energy recovery," *Phys. Rev. Lett.* **84** (Jan, 2000) 662–665. http://link.aps.org/doi/10.1103/PhysRevLett.84.662. 78

72. F. Stephan, C. H. Boulware, M. Krasilnikov, J. Bähr, G. Asova, A. Donat, U. Gensch, H. J. Grabosch, M. Hänel, L. Hakobyan, H. Henschel, Y. Ivanisenko, L. Jachmann, S. Khodyachykh, M. Khojoyan, W. Köhler, S. Korepanov, G. Koss, A. Kretzschmann, H. Leich, H. Lüdecke, A. Meissner, A. Oppelt, B. Petrosyan, M. Pohl, S. Riemann,

S. Rimjaem, M. Sachwitz, B. Schöneich, T. Scholz, H. Schulze, J. Schultze, U. Schwendicke, A. Shapovalov, R. Spesyvtsev, L. Staykov, F. Tonisch, T. Walter, S. Weisse, R. Wenndorff, M. Winde, L. v. Vu, H. Dürr, T. Kamps, D. Richter, M. Sperling, R. Ovsyannikov, A. Vollmer, J. Knobloch, E. Jaeschke, J. Boster, R. Brinkmann, S. Choroba, K. Flechsenhar, K. Flöttmann, W. Gerdau, V. Katalev, W. Koprek, S. Lederer, C. Martens, P. Pucyk, S. Schreiber, S. Simrock, E. Vogel, V. Vogel, K. Rosbach, I. Bonev, I. Tsakov, P. Michelato, L. Monaco, C. Pagani, D. Sertore, T. Garvey, I. Will, I. Templin, W. Sandner, W. Ackermann, E. Arévalo, E. Gjonaj, W. F. O. Müller, S. Schnepp, T. Weiland, F. Wolfheimer, J. Rönsch, and J. Rossbach, "Detailed characterization of electron sources yielding first demonstration of european x-ray free-electron laser beam quality," *Phys. Rev. ST Accel. Beams* **13** (Feb, 2010) 020704. http://link.aps.org/doi/10.1103/PhysRevSTAB.13.020704. 79

73. F. Sannibale, D. Filippetto, C. F. Papadopoulos, J. Staples, R. Wells, B. Bailey, K. Baptiste, J. Corlett, C. Cork, S. De Santis, S. Dimaggio, L. Doolittle, J. Doyle, J. Feng, D. Garcia Quintas, G. Huang, H. Huang, T. Kramasz, S. Kwiatkowski, R. Lellinger, V. Moroz, W. E. Norum, H. Padmore, C. Pappas, G. Portmann, T. Vecchione, M. Vinco, M. Zolotorev, and F. Zucca, "Advanced photoinjector experiment photogun commissioning results," *Phys. Rev. ST Accel. Beams* **15** (Oct, 2012) 103501. http://link.aps.org/doi/10.1103/PhysRevSTAB.15.103501. 79

74. I. V. Bazarov and C. K. Sinclair, "Multivariate optimization of a high brightness dc gun photoinjector," *Phys. Rev. ST Accel. Beams* **8** (Mar, 2005) 034202. http://link.aps.org/doi/10.1103/PhysRevSTAB.8.034202. 79, 80, 101, 116

75. D. H. Dowell, S. Joly, A. Loulergue, J. P. de Brion, and G. Haouat, "Observation of space-charge driven beam instabilities in a radio frequency photoinjector," *Physics of Plasmas* **4** no. 9, (1997) 3369–3379. http://link.aip.org/link/?PHP/4/3369/1. 80

76. http://www.pulsar.nl/gpt/, 2011. http://www.pulsar.nl/gpt/. 80

77. M. Liepe, S. Belomestnykh, E. Chojnacki, Z. Conway, G. Hoffstaetter, R. Kaplan, S. Posen, P. Quigley, J. Sears, V. Shemelin, and V. Veshcherevich, "Status of the cornell ERL injector SCRF cryomodule," in *Proceedings of LINAC 2010*, no. TU303, pp. 382–386. 2010. 81

78. I. V. Bazarov, B. M. Dunham, Y. Li, X. Liu, D. G. Ouzounov, C. K. Sinclair, F. Hannon, and T. Miyajima, "Thermal emittance and response time measurements of negative electron affinity photocathodes," *Journal of Applied Physics* **103** no. 5, (2008) 054901. http://link.aip.org/link/?JAP/103/054901/1. 81, 83

79. I. V. Bazarov, D. G. Ouzounov, B. M. Dunham, S. A. Belomestnykh, Y. Li, X. Liu, R. E. Meller, J. Sikora, C. K. Sinclair, F. W. Wise, and T. Miyajima, "Efficient temporal shaping of electron distributions for high-brightness photoemission electron guns," *Phys. Rev. ST Accel. Beams* **11** (Apr, 2008) 040702. http://link.aps.org/doi/10.1103/PhysRevSTAB.11.040702. 82

80. I. V. Bazarov, B. M. Dunham, X. Liu, M. Virgo, A. M. Dabiran, F. Hannon, and

H. Sayed, "Thermal emittance and response time measurements of a gan photocathode," *Journal of Applied Physics* **105** no. 8, (2009) 083715. http://link.aip.org/link/?JAP/105/083715/1.

81. L. Cultrera, J. Maxson, I. Bazarov, S. Belomestnykh, J. Dobbins, B. Dunham, S. Karkare, R. Kaplan, V. Kostroun, Y. Li, X. Liu, F. Löhl, K. Smolenski, Z. Zhao, D. Rice, P. Quigley, M. Tigner, V. Veshcherevich, K. Finkelstein, D. Dale, and B. Pichler, "Photocathode behavior during high current running in the cornell energy recovery linac photoinjector," *Phys. Rev. ST Accel. Beams* **14** (Dec, 2011) 120101. http://link.aps.org/doi/10.1103/PhysRevSTAB.14.120101.

82. I. Bazarov, L. Cultrera, A. Bartnik, B. Dunham, S. Karkare, Y. Li, X. Liu, J. Maxson, and W. Roussel, "Thermal emittance measurements of a cesium potassium antimonide photocathode," *Applied Physics Letters* **98** no. 22, (2011) 224101. http://link.aip.org/link/?APL/98/224101/1. 81, 83, 97, 98

83. Z. Zhao, B. M. Dunham, I. Bazarov, and F. W. Wise, "Generation of 110 w infrared and 65 w green power from a 1.3-ghz sub-picosecond fiber amplifier," *Opt. Express* **20** no. 5, (Feb, 2012) 4850–4855. http://www.opticsexpress.org/abstract.cfm?URI=oe-20-5-4850. 81, 102

84. V. N. Litvinenko, R. Hajima, and D. Kayran, "Merger designs for erls," *Nuclear Instruments and Methods in Physics Research Section A: Accelerators, Spectrometers, Detectors and Associated Equipment* **557** no. 1, (2006) 165 – 175. http://www.sciencedirect.com/science/article/pii/S0168900205019881. 83

85. T. Miyajima and I. Bazarov, "Simulation study of cornell l0 beamline," ERL Internal Report 11-02, Cornell University, 2011. 83, 84, 116

86. J.-G. Hwang, E.-S. Kim, and T. Miyajima, "Effects of space charge in a compact superconducting energy recovery linac with a low energy," *Nuclear Instruments and Methods in Physics Research Section A: Accelerators, Spectrometers, Detectors and Associated Equipment* **684** no. 0, (2012) 18 – 26. http://www.sciencedirect.com/science/article/pii/S0168900212003439. 83

87. S. Belomestnykh, I. Bazarov, V. Shemelin, J. Sikora, K. Smolenski, and V. Veshcherevich, "Deflecting cavity for beam diagnostics at cornell erl injector," *Nuclear Instruments and Methods in Physics Research Section A: Accelerators, Spectrometers, Detectors and Associated Equipment* **614** no. 2, (2010) 179 – 183. http://www.sciencedirect.com/science/article/pii/S0168900209024000. 84

88. S. van der Geer, M. d. L. O.J. Luiten, G. Pöplau, and U. van Rienen, "Institute of physics conference series," No. 175, p. 101. 2005. 85

89. G. Poplau, U. Van Rienen, B. van der Geer, and M. de Loos, "Multigrid algorithms for the fast calculation of space-charge effects in accelerator design," *Magnetics, IEEE Transactions on* **40** no. 2, (2004) 714–717. 85

90. http://laacg1.lanl.gov/laacg/services/download_sf.phtml, 2012.

http://laacg1.lanl.gov/laacg/services/download_sf.phtml. 85

91. http://www.cobham.com/about-cobham/aerospace-and-security/about-us/antenna-systems/kidlington/products/opera-3d.aspx, 2008. http://www.cobham.com/about-cobham/aerospace-and-security/about-us/antenna-systems/kidlington/products/opera-3d.aspx. 85

92. J. Wei, Y. Papaphilippou, and R. Talman, "Scaling law for the impact of magnet fringe fields," in *Proceedings of the 2000 European Particle Accelerator Conference*, no. TUP3B15, EPAC 2000. Vienna, Austria, 2000. 87

93. M. P. Stockli, R. F. Welton, and R. Keller, "Self-consistent, unbiased root-mean-square rmittance analysis," *Review of Scientific Instruments* **75** no. 5, (2004) 1646–1649. http://link.aip.org/link/?RSI/75/1646/1. 106, 122

94. I. V. Bazarov and G. H. Hoffstaetter, "Lattice options for a 5 gev light source at cornell," in *Particle Accelerator Conference, 2003. PAC 2003. Proceedings of the*, P. of the 2003 Particle Accelerator Conference, ed., vol. 2, pp. 842–844 Vol.2. 2003. 116

95. L. Cultrera, I. Bazarov, J. Conway, B. Dunham, Y. Hwang, Y. Li, X. Liu, T. Moore, R. Merluzzi, K. Smolenski, S. Karkare, J.Maxson, and W. Schaff, "Photocathode R&D at cornell university," in *Proceedings of IPAC2012*, no. WEOAB02, IPAC. New Orleans, Louisiana, USA, 2012. 116

96. "Photocathode physics for photoinjectors 2012," Cornell University. Ithaca, NY, October, 2012. 117

97. R. Nagai, R. Hajima, N. Nishimori, T. Muto, M. Yamamoto, Y. Honda, T. Miyajima, H. Iijima, M. Kuriki, M. Kuwahara, S. Okumi, and T. Nakanishi, "High-voltage testing of a 500-kv dc photocathode electron gun," *Review of Scientific Instruments* **81** no. 3, (2010) 033304. http://link.aip.org/link/?RSI/81/033304/1. 117

98. I. V. Bazarov, "Synchrotron radiation representation in phase space," *Phys. Rev. ST Accel. Beams* **15** (May, 2012) 050703. http://link.aps.org/doi/10.1103/PhysRevSTAB.15.050703. 118, 119

99. https://www.mathworks.com/matlabcentral/fileexchange/8998-surface-fitting-using-gridfit, 2010. https://www.mathworks.com/matlabcentral/fileexchange/8998-surface-fitting-using-gridfit. 121